NAVAL POSTGRADUATE SCHOOL

MONTEREY, CALIFORNIA

THESIS

IMPLEMENTATION OF ACTIVE AND REACTIVE POWER FLOW CONTROL IN A SINGLE PHASE MICROGRID

by

Dimitrios Kanavaros

June 2019

Thesis Advisor:	Giovanna Oriti
Co-Advisors:	Roberto Cristi
	James Calusdian
	Alexander Julian, Non-NPS

THIS PAGE INTENTIONALLY LEFT BLANK

REPORT DOCUMENTATION PAGE	*Form Approved OMB No. 0704-0188*

1. AGENCY USE ONLY ***(Leave blank)***	**2. REPORT DATE** June 2019	**3. REPORT TYPE AND DATES COVERED** Master's thesis

4. TITLE AND SUBTITLE IMPLEMENTATION OF ACTIVE AND REACTIVE POWER FLOW CONTROL IN A SINGLE PHASE MICROGRID	**5. FUNDING NUMBERS**
6. AUTHOR(S) Dimitrios Kanavaros	
7. PERFORMING ORGANIZATION NAME(S) AND ADDRESS(ES) Naval Postgraduate School Monterey, CA 93943-5000	**8. PERFORMING ORGANIZATION REPORT NUMBER**
9. SPONSORING / MONITORING AGENCY NAME(S) AND ADDRESS(ES) N/A	**10. SPONSORING / MONITORING AGENCY REPORT NUMBER**

11. SUPPLEMENTARY NOTES The views expressed in this thesis are those of the author and do not reflect the official policy or position of the Department of Defense or the U.S. Government.

12a. DISTRIBUTION / AVAILABILITY STATEMENT Approved for public release. Distribution is unlimited.	**12b. DISTRIBUTION CODE** A

13. ABSTRACT (maximum 200 words)

A microgrid is a miniature version of a large power grid, and its purpose is to operate autonomously and to increase the reliability of the power system in a naval installation. It is a local area power system, which is able to operate either as a subset of a main grid or in an autonomous mode (islanded). The power flowing from a utility to a microgrid and vice-versa has two components: 1) active power, which is the real power that can be transformed from electric to non-electric by the loads; and 2) reactive power, which is generated by inductive loads, such as electric motors. The presence of the latter category lessens the energy efficiency of an installation, reduces the real energy, and increases the cost of the electricity for the consumer.

The compensation for the reactive power and simultaneously the control of the active power is obtained by a highly developed electronic system, called the Energy Management System (EMS). It manages the distributed energy resources in a microgrid, such as batteries, and renewable energy sources to ensure that electricity is available to an installation when the main grid is off.

In our research, four different methods of EMS control have been examined in order to regulate the electricity delivered to the consumer for maximum available power and to reduce the cost of the electricity. Simulated plots are presented and validated by experimental waveforms measured on a laboratory prototype.

14. SUBJECT TERMS active power, reactive power, power factor, microgrid, single phase microgrid	**15. NUMBER OF PAGES** 115
	16. PRICE CODE

17. SECURITY CLASSIFICATION OF REPORT Unclassified	**18. SECURITY CLASSIFICATION OF THIS PAGE** Unclassified	**19. SECURITY CLASSIFICATION OF ABSTRACT** Unclassified	**20. LIMITATION OF ABSTRACT** UU

NSN 7540-01-280-5500 Standard Form 298 (Rev. 2-89)
Prescribed by ANSI Std. 239-18

THIS PAGE INTENTIONALLY LEFT BLANK

IMPLEMENTATION OF ACTIVE AND REACTIVE POWER FLOW CONTROL IN A SINGLE PHASE MICROGRID

Dimitrios Kanavaros
Lieutenant, Hellenic Navy
B.S., Hellenic Naval Academy, 2007

Submitted in partial fulfillment of the
requirements for the degrees of

ELECTRICAL ENGINEER

and

MASTER OF SCIENCE IN ELECTRICAL ENGINEERING

from the

NAVAL POSTGRADUATE SCHOOL
June 2019

Approved by: Giovanna Oriti
Advisor

Roberto Cristi
Co-Advisor

James Calusdian
Co-Advisor

Alexander Julian
Co-Advisor

Douglas J. Fouts
Chair, Department of Electrical and Computer Engineering

THIS PAGE INTENTIONALLY LEFT BLANK

ABSTRACT

A microgrid is a miniature version of a large power grid, and its purpose is to operate autonomously and to increase the reliability of the power system in a naval installation. It is a local area power system, which is able to operate either as a subset of a main grid or in an autonomous mode (islanded). The power flowing from a utility to a microgrid and vice-versa has two components: 1) active power, which is the real power that can be transformed from electric to non-electric by the loads; and 2) reactive power, which is generated by inductive loads, such as electric motors. The presence of the latter category lessens the energy efficiency of an installation, reduces the real energy, and increases the cost of the electricity for the consumer.

The compensation for the reactive power and simultaneously the control of the active power is obtained by a highly developed electronic system, called the Energy Management System (EMS). It manages the distributed energy resources in a microgrid, such as batteries and renewable energy sources, to ensure that electricity is available to an installation when the main grid is off.

In our research, four different methods of EMS control have been examined in order to regulate the electricity delivered to the consumer for maximum available power and to reduce the cost of the electricity. Simulated plots are presented and validated by experimental waveforms measured on a laboratory prototype.

THIS PAGE INTENTIONALLY LEFT BLANK

TABLE OF CONTENTS

THIS PAGE INTENTIONALLY LEFT BLANK

LIST OF FIGURES

LIST OF TABLES

THIS PAGE INTENTIONALLY LEFT BLANK

LIST OF ACRONYMS AND ABBREVIATIONS

AC	Alternating Current
APF	All-Pass Filter
DC	Direct Current
DER	Distributed Energy Resources
DG	Distributed Generation
DoD	Department of Defense
DQ	Direct-Quadrature
DS	Distributed Storage
EMI	ElectroMagnetic Interference
EMS	Energy Management System
FPGA	Field Programmable Gate Array
FY	Fiscal Year
IEEE	Institute of Electrical and Electronics Engineers
JTAG	Join Test Action Group
LPF	Low-Pass Filter
OGM	Orthogonal Generation Methods
PC	Personal Computer
PCB	Printed Circuit Boards
PG&E	Pacific Gas & Electric
PI	Proportional and Integral
PLL	Phase-Locked Loop
PWM	Pulse Width Modulation
SOGI	Second-Order Generalized Integrator
U.S.	United States
VHDL	Very High Speed Integrated Circuit Hardware Description Language

THIS PAGE INTENTIONALLY LEFT BLANK

ACKNOWLEDGMENTS

First of all, I would like to express the deepest appreciation to my thesis advisor, Dr. Giovanna Oriti, and my co-advisor, Dr. Alexander Julian, for their guidance and continuous support. They were always there for me whenever I ran into a trouble spot or had a question about my research or writing.

In addition, I feel very grateful for the collaboration that I had with Dr. Roberto Cristi and Dr. James Calusdian, who provided me with valuable comments for this thesis.

Last but not least, I would like to express my very profound gratitude to my beloved wife, Andromahi, and my little son, Stavros, for providing me with unfailing support and continuous encouragement throughout my years of study and through the process of researching and writing this thesis. I love you so much. Thank you.

I. INTRODUCTION

Military installations rely heavily on the availability of electric power 24 hours per day to carry out their missions. Therefore, a power outage that lasts more than a few hours may jeopardize military operations. It would have dire outcomes for the soldiers—not only for their training, but even worse, for their living conditions. Department of Defense (DoD) installations cannot afford to wait for the local power companies to fix power outages, but must have back-up power to sustain critical loads in order to continue the military mission. Therefore, other types of resources such as wind turbines, solar panels, and batteries are needed nowadays to ensure that an installation will be supplied with power during a power outage. To that end, a continuous energy supply offers a solution. But, is this the only use that these alternative sources can offer? The answer to this question is negative, and this thesis tests and suggests an additional benefit of such sources.

Generally, two different types of power flow in a power grid: 1) active power, which is the real power that can be transformed from electric to non-electric by the loads; and 2) reactive power, which is generated by inductive loads, such as electric motors. The presence of the latter category lessens the energy efficiency of the grid, reduces the amount of real energy supplied to the load, and consequently increases the cost of the electricity for the consumer. The purpose of this thesis is to examine how these two types of power can be controlled in such a way that the maximum amount of active power is delivered to the load while minimizing the reactive power in the grid. The reduction of the power efficiency, the decrease of the active power, and the rise of the cost of the electricity caused by reactive power in the grid, can be minimized or some of them can even be eliminated by the use of appropriate control of distributed energy resources.

The United States (U.S) DoD is the largest energy consumer in the United States, and for that reason, the improvement of energy efficiency and the increase of the production of renewable energy are two DoD main goals in this area. And, these goals are challenging. The DoD has over 500 installations around the world, containing approximately 300,000 buildings [1]. Therefore, it is necessary to use distributed energy resources to ensure that the U.S. DoD military installations worldwide are supplied with electrical power 24 hours per day.

The annual goals of the DoD concerning energy performance from Fiscal Years (FY) 2011 to 2025 are provided in Table 1.

Table 1. Annual goals of the DoD concerning energy performance. Source: [1].

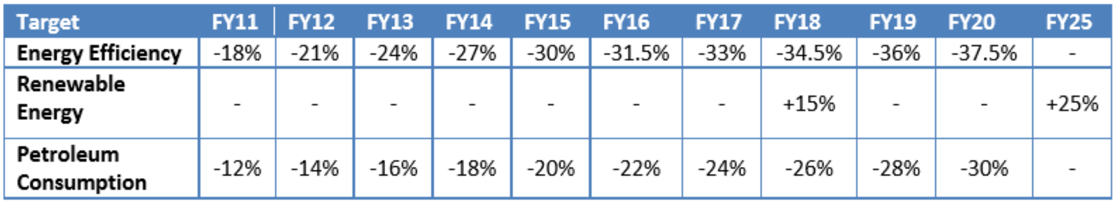

Target	FY11	FY12	FY13	FY14	FY15	FY16	FY17	FY18	FY19	FY20	FY25
Energy Efficiency	-18%	-21%	-24%	-27%	-30%	-31.5%	-33%	-34.5%	-36%	-37.5%	-
Renewable Energy	-	-	-	-	-	-	-	+15%	-	-	+25%
Petroleum Consumption	-12%	-14%	-16%	-18%	-20%	-22%	-24%	-26%	-28%	-30%	-

It is clear from the table that the DoD, as the main energy consumer, wants to:

- Improve its energy efficiency by decreasing energy consumption of its installations.
- Develop and establish renewable sources of energy.
- Decrease consumption of petroleum fuel.

Therefore, many different renewable energy projects have been implemented by the DoD in order to succeed in those aims. Figure 1 shows a sample of those projects that are already implemented or are scheduled to be activated at military facilities across the United States. It has to be mentioned that there are also a lot of other DoD energy projects across the United States and abroad. The repetition of some numbers in different places shows that the same project has been executed in different locations.

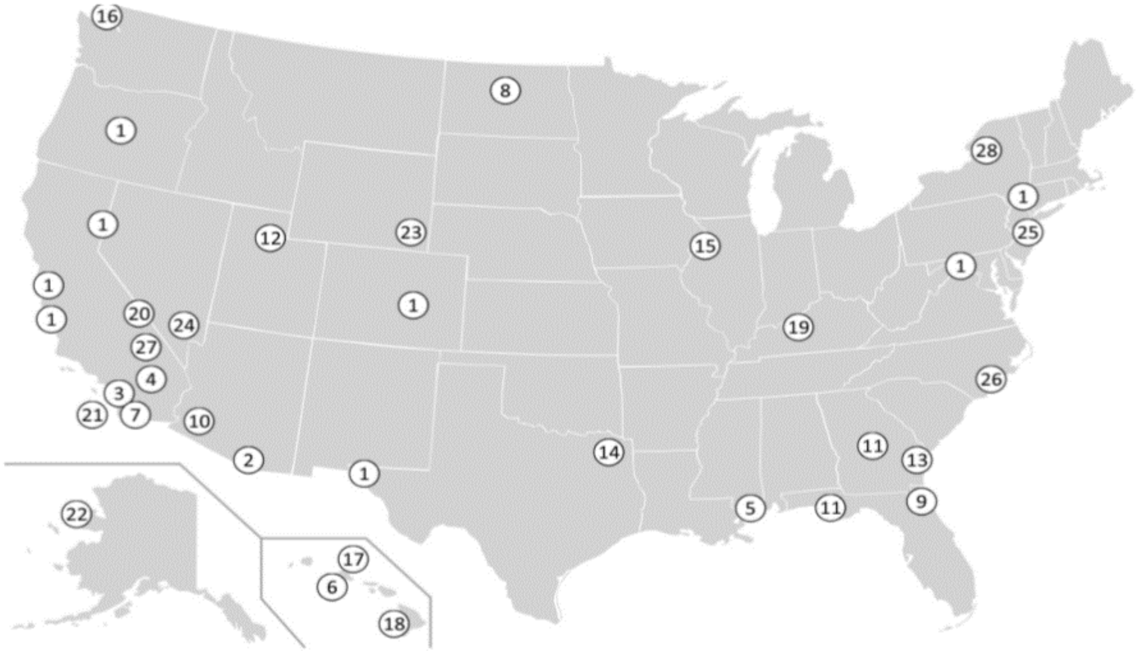

Figure 1. A sample of energy projects that have been implemented in the United States. Source: [2].

This thesis illustrates how a combination of the main grid and renewable resources can be implemented not only to maximize power efficiency but also to decrease the cost of the electricity for the consumer.

In our research, we examine four different methods of controlling renewable resources in order to regulate the active and reactive power flow from the source in a single-phase microgrid when it operates in grid-connected mode. Experimental measurements validate the simulated results and, therefore, three of those different kinds of controls have accomplished the maximum desired efficiency. This means that the microgrid can compensate for reactive power and, simultaneously, manage the active power. This contributes to a reduction in the cost of the electricity and an increase in the maximum available power delivered to the consumer.

In Chapter II, we present background information, including some fundamental definitions related to power systems engineering. Chapter III illustrates a detailed analysis of the Energy Management System (EMS), a highly developed electronic system that can manage the distributed energy resources of the microgrid and loads. In Chapter IV, the designed active and reactive power flow controllers are presented together with the four different methods of controlling the renewable resources. The simulation and the experimental validation are presented in Chapter V and Chapter VI, respectively. Finally, conclusions and recommendations for future work are provided in Chapter VII.

II. BACKGROUND

In this chapter, some essential terms and concepts related to power systems engineering are presented. The definition of active and reactive power, as well as the power factor, is provided. This chapter also offers a basic understanding of the microgrid and the Energy Management System (EMS).

A. ALTERNATING CURRENT MAIN GRID

1. Active and Reactive Power

From a very broad perspective, one of the main purposes of power electronics is to handle and manage the flow of power in such a way that we will have high efficiency with our system. In Figure 2, we see how a main (alternating current, or AC) grid distributes power to the loads. Usually, the power input is the main grid at a line frequency of 50 Hz (for Europe) or 60 Hz (for the United States), in a single phase or in three phases. The quantity v_{ac} is the line voltage, which is usually 120 Volts AC and i_{ac} is the line current provided to the load. In this thesis, linear loads are examined along with single phase AC microgrids.

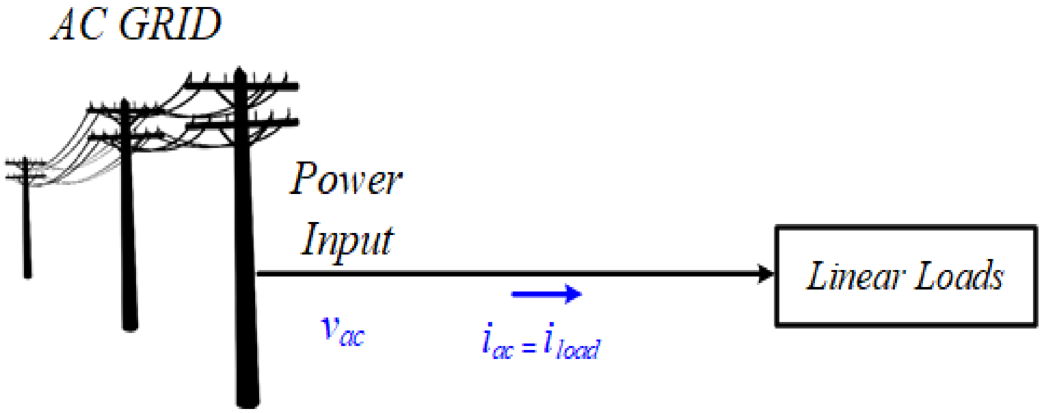

Figure 2. Main grid

Linear loads are those loads that, when a sinusoidal source is applied, produce a current that is a pure sinusoidal current i_{load} with the same frequency as the input source. This can occur when the loads are resistors (such as incandescent lights), inductors (such as AC motors), or capacitors. While there are loads that have capacitive components, the resistive and inductive elements are usually dominant. As a result, capacitive loads are not often found in buildings [3]. For this reason, in this thesis, the type of linear loads examined are a combination of resistors and inductors.

For a single-phase system, where the voltage v_{ac} of the AC grid source is a sinusoidal function, the voltage, and the current of our resistive—inductive linear load is [4]

$$v_{ac} = v_{load} = \sqrt{2} V_{rms} \sin(\omega t) \tag{1}$$

$$i_{ac} = i_{load} = \sqrt{2} I_{rms} \sin(\omega t - \varphi)\,, \tag{2}$$

where V_{rms} and I_{rms} are the root mean square values of voltage and current, respectively; ω is the angular frequency of the line; and φ is the phase angle between the voltage v_{ac} and the current i_{ac}.

Therefore, the instantaneous power p provided to the load under sinusoidal conditions is $p = v_{ac}\, i_{ac}$. Incorporating equations (1) and (2) gives

$$p = V_{rms} I_{rms} \cos\varphi \left[1 - \cos(2\omega t)\right] - V_{rms} I_{rms} \sin(\varphi) \sin(2\omega t)\,. \tag{3}$$

The average value of the first term of Equation (3) is

$$P = V_{rms} I_{rms} \cos\varphi\,, \tag{4}$$

which is the active (real) power, while the peak value of the second term is

$$Q = V_{rms} I_{rms} \sin\varphi\,, \tag{5}$$

which is the reactive power.

Recall that active power is the real power delivered to the load and contributes to the actual work done by the power system. On the other hand, the reactive power, which is generated in our AC system by the reactive elements such as capacitors and inductors, is caused by periodic exchange of capacitive and magnetic energy between capacitors and inductors. Since the average energy exchanged by the reactive component is zero, its power delivered to the load is zero as well. On the other hand, since the energy is exchanged through conductors with resistance, the presence of a strong reactive power component causes energy dissipation in the transmission lines.

In equations (4) and (5), the phase angle φ influences the active and reactive power significantly. As a result, by controlling the phase angle, we can in turn control the amount of active and reactive power delivered to the load.

Moreover, we should introduce one other term that is more commonly used, and this is the *power factor*. The power factor is a measurement of how efficient a system is. Mathematically, the power factor is defined as

$$pf = \cos\varphi . \tag{6}$$

2. Phasor Diagram

A graphical analysis can be done comparing the voltage and the current of the main grid and the current of the loads. This analysis is the phasor diagram, which can be observed in Figure 3. As it has been mentioned, the types of linear loads used in this thesis consist of inductors and resistors. This is the reason why I_{load}, which is equal to the current I_{ac}, is lagging in the phasor diagram with a phase angle of φ as compared with the input voltage V_{ac} of the AC grid. Analyzing the phasor representation of our power system, we will show how we can manage the current in a utility in order to obtain a unity power factor at the main grid.

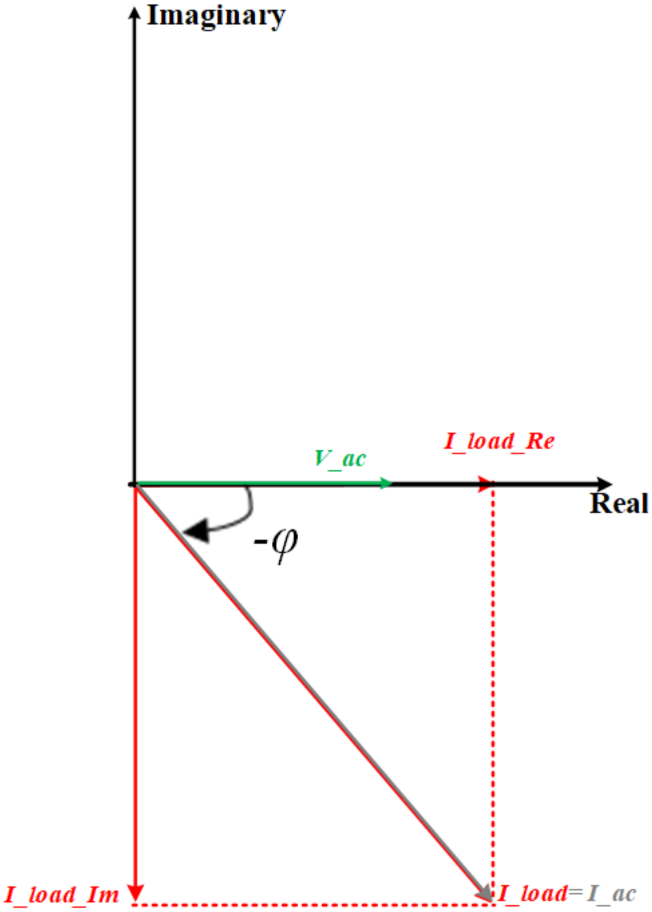

Figure 3. Phasor diagram when the loads are powered by the main grid

From Figure 3, it can be seen that the *I_load_Im*, which is equal to *I_ac_Im*, is the reason the reactive power exists. In order to eliminate power losses in the transmission lines due to the flow of the reactive power Q, the power factor should be unity so that the angle difference between the voltage and the current at the grid is zero, as shown by

$$Q = 0 \Leftrightarrow V_{rms} I_{rms} \sqrt{1-(pf)^2} = 0 \Leftrightarrow pf = 1 \Leftrightarrow \varphi = 0\,. \tag{7}$$

Having analyzed the basic concepts and definitions about active and reactive power flow in the main grid, we perform an analogous analysis for a single-phase microgrid in grid-connected mode.

B. SINGLE-PHASE MICROGRID

A general view of the installation examined in this thesis is shown in Figure 4, where we have added the microgrid to the main grid.

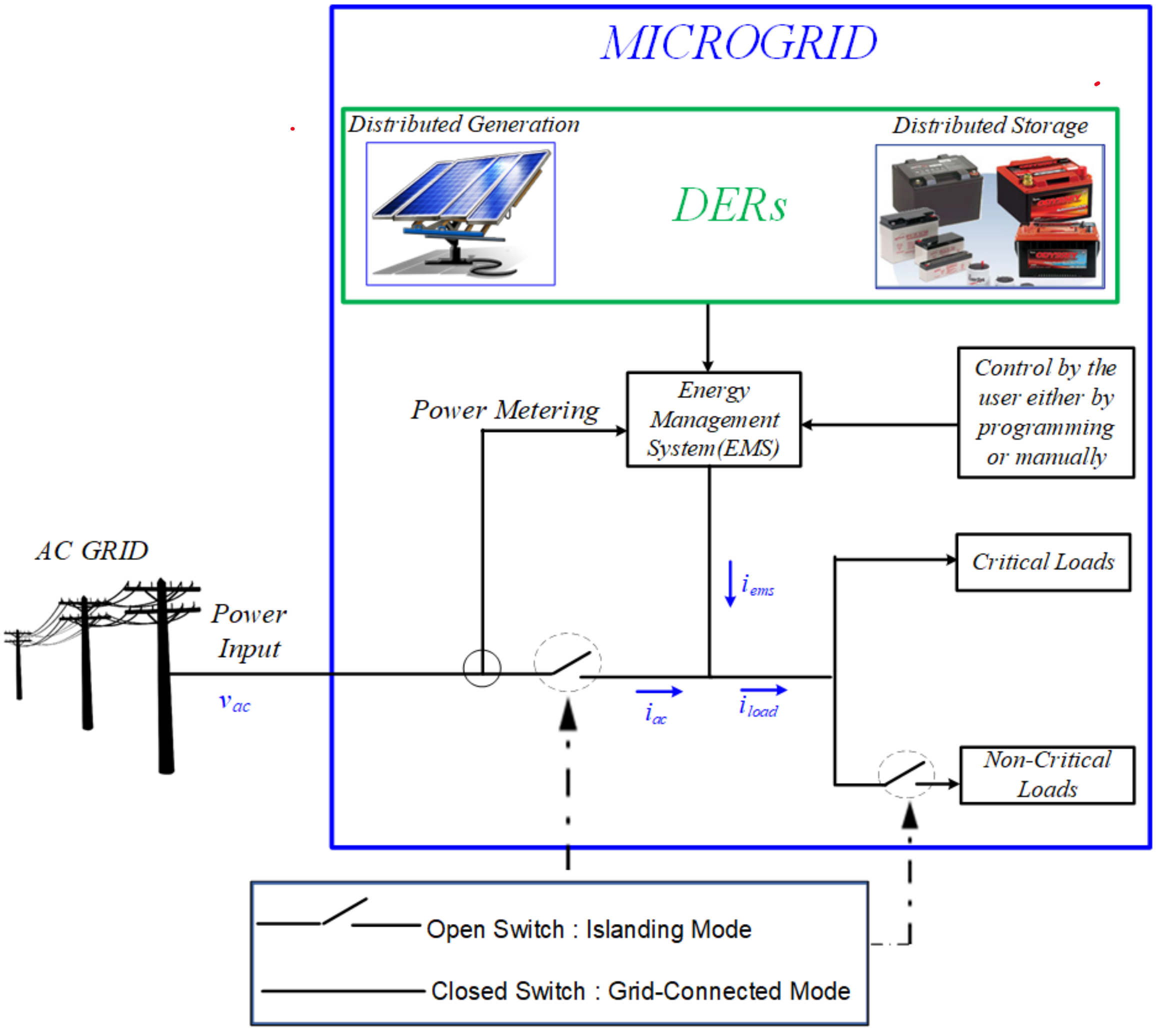

Figure 4. General view of a microgrid

The word microgrid is composed of micro (originating from the Greek word *mikros*, which means small) and grid, indicating that a microgrid is a miniaturization of the main grid with the main purpose to operate autonomously and to increase the reliability of the power system. In other words, a microgrid is local area power system, composed of a network of electricity sources with the capability to store and provide energy for a facility, such as a home, building, or even a small town, primarily during emergencies like the blackout of the main power source. Therefore, the microgrid can be disconnected from the main grid and can be operated autonomously, improving the reliability of the system. This operation is also known as islanding mode.

The other mode of operation of the microgrid is when the main grid is connected and is called the grid-connected mode. In this thesis, we examine our electronic power system when the microgrid functions in the latter mode of operation.

Today the need for electric power 24 hours per day all over the world has led to the pervasive use of Distributed Energy Resources (DER), including generators, solar panels, and energy storage systems, such as batteries. DERs are often integrated to form a microgrid to ensure that electricity is available to an installation when the main grid is off. Control of the DERs and loads when a microgrid exists can be established by an EMS, a highly developed electronic system that not only manages the microgrid DERs and loads, but can also detect when the main grid is off (power metering), and controls whether the microgrid operates in grid-connected mode or in islanding mode (disconnected from the main AC grid) [5]–[7].

As we can observe from Figure 4, the loads are separated into critical and noncritical loads. By critical loads, we mean those loads that are crucial for the function of the installation and by noncritical loads, those that are not essential.

Finally, yet importantly, it would be wise to mention that when the microgrid works in islanding mode, the operator can specify whether the noncritical loads need to be supplied by power. This is illustrated in our circuit by the existence of the switch at the noncritical loads.

C. OBJECTIVE

1. Current Injection in Resistive–Inductive Loads

One of the goals of the control of the microgrid is to compensate for reactive power. In other words, the voltage and the current at the grid could have the same phase, and as a result, the power factor in the input will be unity, as in Equation (7).

In order for this to occur, the current of the EMS has to be controlled. Specifically, it can be noticed from Figure 4 that the current in the load will be equal to not only the current of the main grid, but to the sum of the AC current and the current of the EMS:

$$I_{load} = I_{ac} + I_{ems} \,. \tag{8}$$

A phasor diagram similar to that of the main grid in Figure 3 is shown in Figure 5 for the single-phase microgrid.

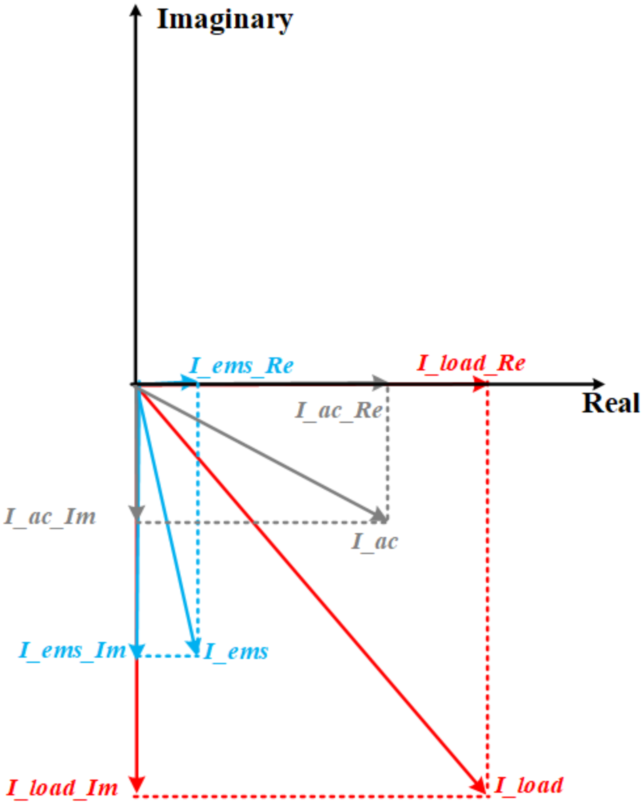

Figure 5. Phasor diagram for the currents without control of EMS current

As shown in Figure 5, the reactive-inductive current load, the EMS current, and the current of the main grid will be

$$I_{load} = I_{load\_\mathrm{Re}} + jI_{load\_\mathrm{Im}} \tag{9}$$

$$I_{ac} = I_{ac\_\mathrm{Re}} + jI_{ac\_\mathrm{Im}} \tag{10}$$

$$I_{ems} = I_{ems\_\mathrm{Re}} + jI_{ems\_\mathrm{Im}} . \tag{11}$$

Therefore, from equations (8), (9), (10), and (11), the current of the EMS will be

$$I_{ems} = I_{load} - I_{ac} \Leftrightarrow I_{ems} = (I_{load\_\mathrm{Re}} - I_{ac\_\mathrm{Re}}) + j(I_{load\_\mathrm{Im}} - I_{ac\_\mathrm{Im}}) \Leftrightarrow$$

$$\Leftrightarrow \begin{cases} I_{ems\_\mathrm{Re}} = I_{load\_\mathrm{Re}} - I_{ac\_\mathrm{Re}} & (12) \\ I_{ems\_\mathrm{Im}} = I_{load\_\mathrm{Im}} - I_{ac\_\mathrm{Im}} . & (13) \end{cases}$$

This is the case where the I_{ems} is injected in resistive–inductive loads. It is obvious that in this case, the reactive current is not eliminated. In order for this to happen, the EMS current has to behave as a resistive-capacitance current; this condition is investigated next.

2. Current Injection to Create Unity Power Factor

As previously mentioned, our purpose is to ensure the current and the voltage at the main grid be in phase, because in that way the whole reactive power will be compensated for. Therefore, the I_{ac_Im} has to be diminished or, in other words, I_{ac_Im} has to equal zero.

$$I_{ac\_\mathrm{Im}} = 0 . \tag{14}$$

Taking into consideration equations (12), (13), and (14), the current of the EMS is

$$I_{ems\_\mathrm{Re}} = I_{load\_\mathrm{Re}} - I_{ac\_\mathrm{Re}} \tag{15}$$

$$I_{ems\_\mathrm{Im}} = I_{load\_\mathrm{Im}} . \tag{16}$$

The last two equations (15) and (16) are the core of what the purpose of this thesis is. They show that by controlling the EMS current, we can also control the active and reactive power. ***Consequently, for the elimination of Q, the EMS current must be in the opposite direction of the current load and must have the same amplitude.***

In Figure 6, we can observe how the phasor diagram in the single-phase microgrid in grid-connected mode changes when the EMS current is controlled in such way that a completely reactive compensation is accomplished. **Therefore, if the I_{ems} is managed**

properly, both active and reactive power can be controlled such that unity power factor is realized in the main grid.

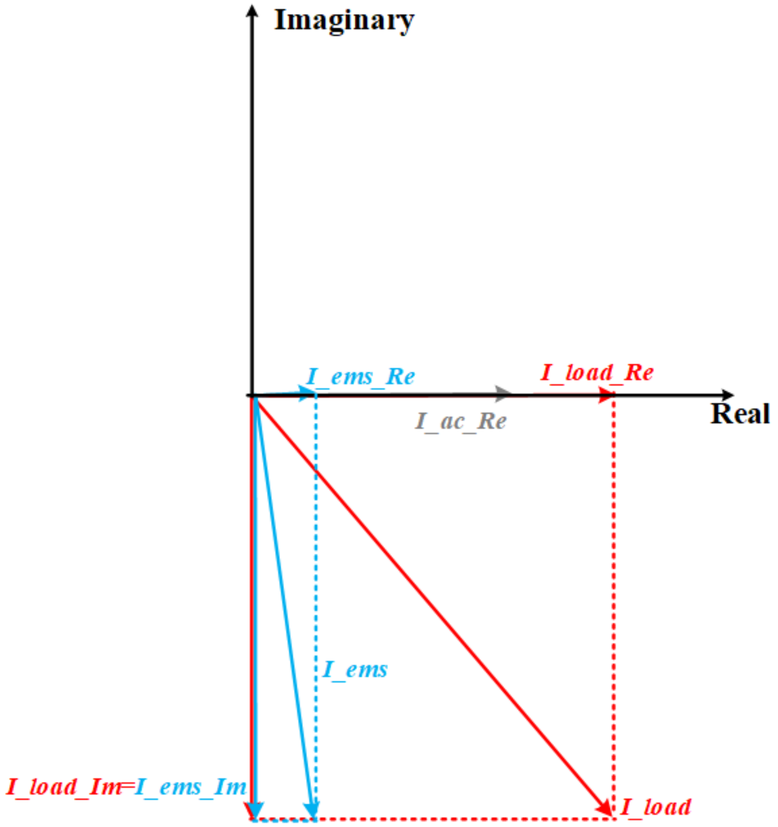

Figure 6. Phasor diagram for the currents when control of EMS current occurs

In the next chapter, we present a detailed illustration and analysis of the EMS in order to explain how the EMS current can be controlled to accomplish unity power factor at the main grid.

THIS PAGE INTENTIONALLY LEFT BLANK

III. ENERGY MANAGEMENT SYSTEM

In the previous chapter, we presented a very broad view of the EMS. In this chapter, a more detailed description of how the EMS operates is offered in order to better convey how the EMS current can be controlled.

A. FUNCTIONALITY

By observing equations (12) and (13), we can conclude that when the EMS is operating in grid-connected mode, an extra current, and as a result, extra power can be given to the critical and noncritical loads. This can play a significant role in the functionality of the EMS. Specifically, the EMS can act as a vital tool in [7]:

- Creating unity power factor at the main grid, which is the topic of this thesis.
- Improving power efficiency.
- Reducing fuel consumption.
- Accomplishing peak power shaving. This is a technique for lessening the peak power drawn from the utility.
- Recognizing when an islanding or grid-connected mode is needed.
- Improving the reliability of our power system, especially when it operates in islanding mode. Thus, when an emergency occurs in the utility, such as a power outage, the EMS manages the microgrid’s resources.
- Harvesting and sharing renewable energy. Therefore, it is not necessary to immediately consume this energy, but it can be stored for future use.
- Operating as a current controlled source in grid-connected mode or voltage controlled source in islanding mode.

In the majority of the previously mentioned capabilities of the EMS, the main impact is that a reduction of the cost of the electricity will be achieved by providing the consumer with the maximum available power.

B. DESCRIPTION

In Figure 7, a schematic view of the EMS architecture is presented. Each part of the following figure is subsequently analyzed for better comprehension of our system [7].

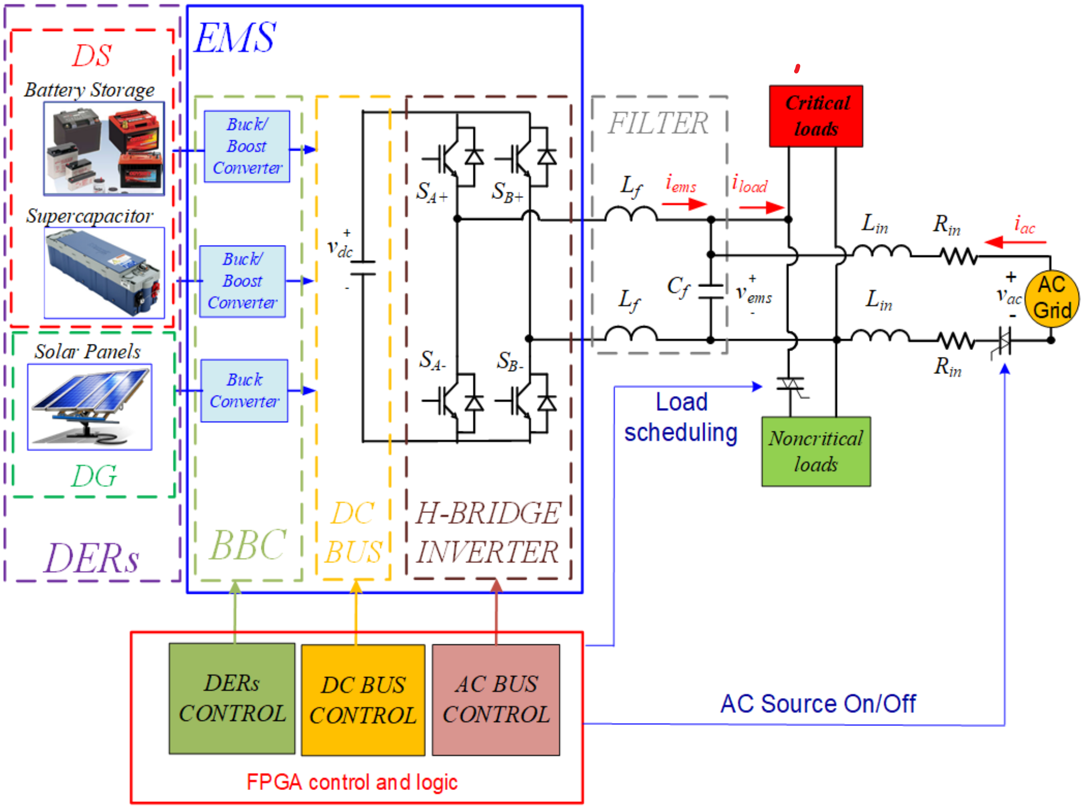

Figure 7. EMS architecture. Adapted from [7].

1. Distributed Generation and Distributed Storage

In the local power system, the existence of DERs, either the Distributed Generation (DG) resources such as solar panels or the Distributed Storage (DS) resources such as batteries and supercapacitors, offers

- additional energy to the microgrid
- electricity to our power system when the main grid is off (islanding mode)
- Direct Current (DC) power supply to the microgrid
- harvest of renewable energy to the DS resources.

2. Buck and Boost Converters

The buck and the boost converters provide regulation of the DC bus interfacing the DERs to the rest of the microgrid. More specifically, the boost converter increases the DC voltage at the output of the DERs to the DC voltage value required at the input of the H-bridge inverter. On the other hand, the buck converter steps down the voltage when power flows from the DC bus to the battery in the DS. In this thesis the DC bus voltage is regulated at 215V while the battery voltage is 72V; therefore, a boost converter is required when the batteries supply power to the microgrid while a buck converter is necessary to charge the batteries from the DC bus. The DC Bus Controller determines when the buck or the boost converter should operate.

3. DC Bus Voltage

The purpose of the bus voltage in the EMS architecture is to interface the DERs, which are DC components, to the rest of the system. According to the type of voltage, the EMS includes an AC and a DC bus, as shown in Figure 7. The AC bus voltage, where the loads are connected, is controlled by the H-bridge inverter, which is analyzed in the next section. The DC bus is controlled to the desired DC voltage value required by the H-bridge inverter to control AC bus voltage, as required by the loads.

4. H-Bridge Inverter

The H-Bridge Inverter consists of two one-leg inverters. Its purpose is to convert the DC voltage from the DC bus to AC voltage by appropriately controlling each leg in the bridge. Therefore, at the output of the H-bridge inverter, we achieve a sinusoidal signal with the desired amplitude v_{ems} and frequency.

In the case of the grid-connected microgrid mode, however, the EMS acts as a current-controlled source and the main grid is the voltage-controlled source. Consequently, only the output current of this inverter, called i_{ems}, can be a sinusoidal signal with ***controllable*** amplitude and frequency.

In order to form this signal and regulate the output current, the switches of this inverter have to be Pulse-Width Modulated (PWM). This means that the voltage output waveform and the desired sinusoidal output current waveform will be generated after a comparison between a triangular waveform with a constant switching frequency f_s and a sinusoidal control signal [8].

In Figure 8, the duty cycle control input signal $v_{control}$ and the triangle waveform are illustrated. The result of their comparison is shown in Figure 9, which represents a rectangular pulse signal before filtering. After filtering, the output voltage becomes the dashed sinusoidal signal v_{o1} of Figure 9.

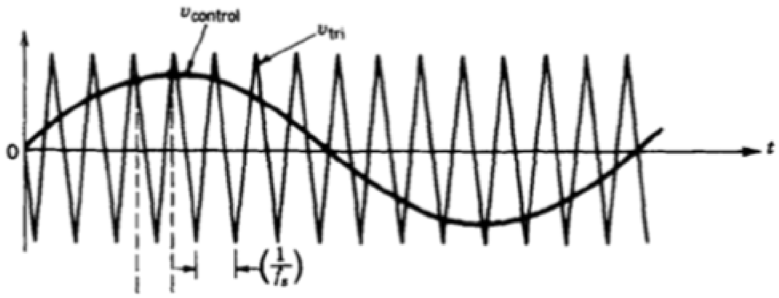

Figure 8. Duty cycle control input signal and the triangle waveform. Source: [8].

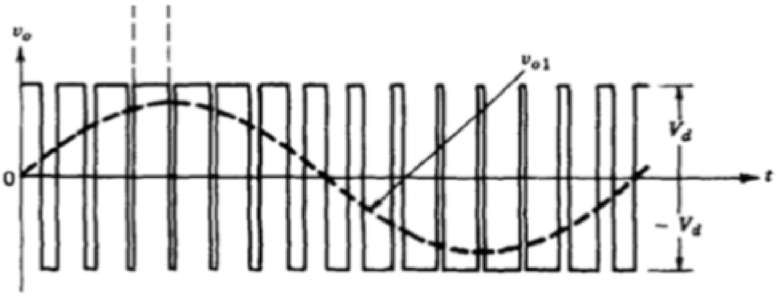

Figure 9. Duty cycle control output signal. Source: [8].

Finally, yet importantly, it should be mentioned there are two different ways to create this rectangular pulse. In other words, there are two types of PWM, depending on the way the legs operate [8]:

- Bipolar: The two one-leg inverters are switching in pairs (S_{A+} , S_{B-}) and (S_{A-} , S_{B+}). Therefore, when one pair is on, the other is off, and vice versa.

- Unipolar: Each one-leg of the inverter is switching separately of the other leg.

5. Filter

A Low Pass Filter (LPF) is shown in the output of the H-bridge inverter. The aim of this filter is to convert the PWM rectangular pulse into sinewave current i_{ems} and voltage v_{ems} and also to smooth the voltage and current waveforms [9]. As we have mentioned, the dashed sinusoidal waveform of Figure 9 is the desired waveform after filtering. The filter consists of one capacitor C_f and two inductors L_f. Two inductors are required to balance the circuit [9].

6. Critical and Noncritical Loads

All the loads of our system are separated into two main categories depending on whether their use is crucial for the functionality of our power system:

- critical loads
- noncritical loads

As can be assumed by their names, the critical loads are those loads that are definitely needed for the performance of our local power system, especially when an emergency occurs. As a result, these loads are provided with power in either islanding or grid-connected mode. On the other hand, the noncritical loads are those loads that do not affect in a significant way the operation of our system in islanding form, and this is the reason they are not supplied with energy in emergency cases.

THIS PAGE INTENTIONALLY LEFT BLANK

IV. MODELING AND CONTROL

The AC bus control system shown in Figure 10 is explained in this chapter. Each part of the controller is analyzed in detail by showing its functionality and its Simulink model. Four different methods of active and reactive power flow control are presented for a single-phase microgrid operating in grid-connected mode.

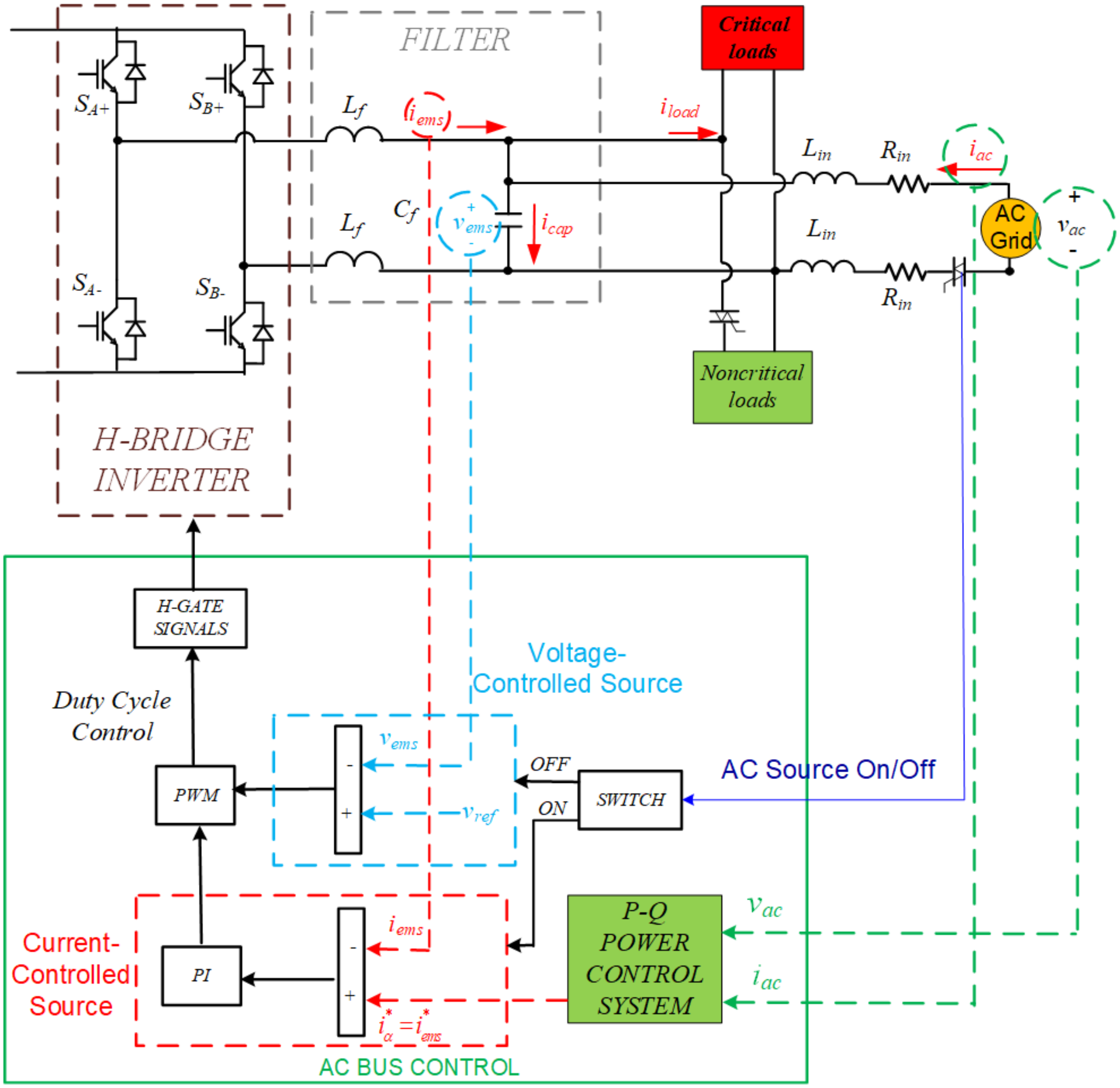

Figure 10. AC bus control system. Adapted from [7].

A. P-Q POWER CONTROL SYSTEM

The proposed P-Q controller of the AC source power flow is depicted in Figure 11. One of its novelties is that part of the control is implemented in the Direct-Quadrature (DQ) synchronous frame to ensure the steady state error is zero, while part is implemented in the αβ stationary frame. In this figure, each step of the control algorithm can be observed. A detailed description of each part follows separately.

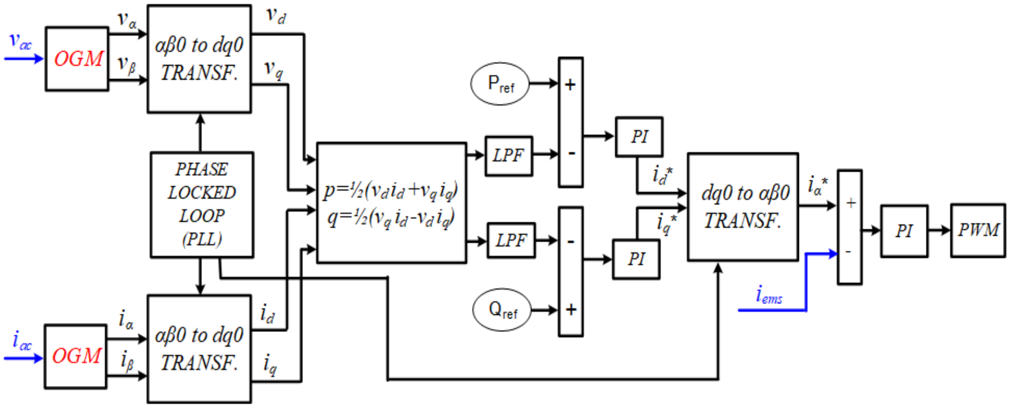

Figure 11. Block diagram of the novel P-Q source power flow controller

1. Model of the AC Grid

The AC grid was modeled in three different ways in order to create different conditions under which the various control methods could be tested. The three models are described in the following sections.

a. AC Grid as Ideal Voltage Source

An ideal voltage supply is a circuit component that retains its nominal value across its terminals, irrespective of the current flowing across those terminals [10]. Thus the AC grid voltage is given by

$$v_{ac} = V_m \sin(\omega t) \Leftrightarrow v_{ac} = V_m \sin(2\pi * f * t) \Leftrightarrow v_{ac} = 120\sqrt{2}\sin(2\pi * 60 * t). \qquad (17)$$

Laboratory measurements of the AC grid voltage have shown that it is not an ideal voltage source; therefore, other models that include harmonic components and frequency noise are also examined.

b. *AC Grid as Voltage Source with Harmonics*

In contrast with the ideal source, the AC source in reality is not a perfect sinewave, but has harmonics, which can cause disturbance in the control system. As mentioned previously, the line frequency (or in other words the fundamental frequency) for the United States is 60 Hz. The harmonics are odd multiples of the fundamental frequency and can be calculated by implementing Fourier analysis [8]. In Figure 12, we can observe an example of how a sinusoidal waveform is distorted when the third (f_3 = 3*60= 180 Hz) and fifth (f_5 = 5*60= 300 Hz) harmonics are added to the fundamental frequency component [11].

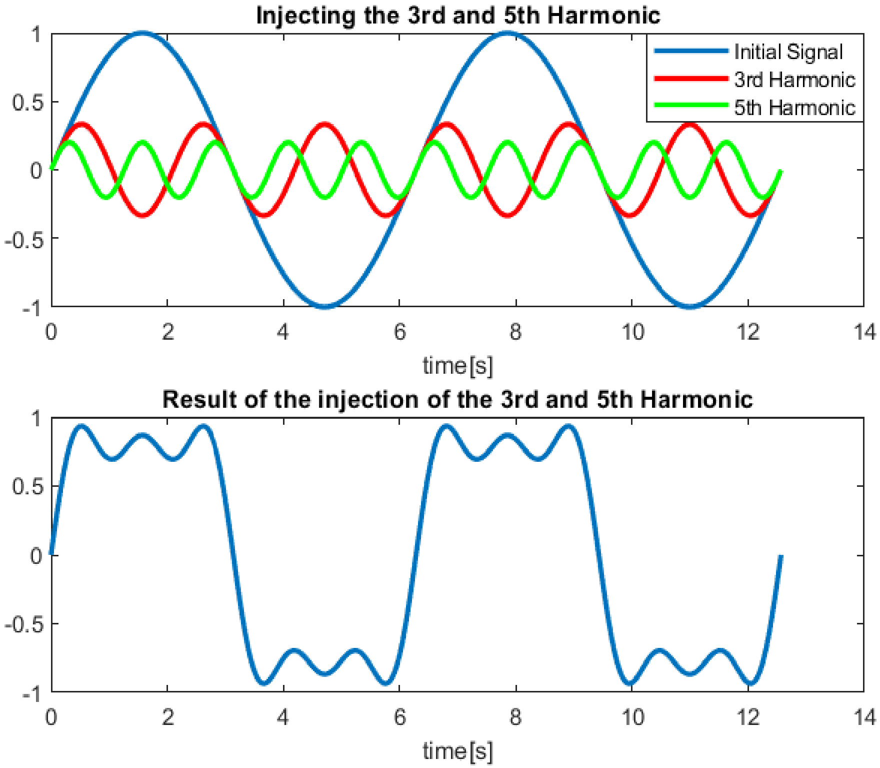

Figure 12. Distorted voltage waveform due to harmonics Source: [11].

In Chapter VI, experimental measurements of the AC grid voltage are analyzed to highlight their harmonic content. Taking those measurements into consideration, we implement the same amplitudes and frequencies in the Simulink model in order to obtain realistic simulation results. In Table 2 all the harmonics that have been added to the ideal sinusoidal voltage are listed:

Table 2. AC grid harmonic components

	Frequency	**Amplitude Voltage Harmonic in case of P=150 W and Q=0 VARS**	**Amplitude Voltage Harmonic in case of P=500 W and Q=0 VARS**
3rd Harmonic	60 x **3** = 180 Hz	V_**3** = 0.6016 Volts	V_**3** = 0.6707 Volts
5th Harmonic	60 x **5** = 300 Hz	V_**5** = 3.324 Volts	V_**5** = 3.243 Volts
7th Harmonic	60 x **7** = 420 Hz	V_**7** = 1.539 Volts	V_**7** = 1.417 Volts
9th Harmonic	60 x **9** = 540 Hz	V_**9** = 0.3774 Volts	V_**9** = 0.3367 Volts
11th Harmonic	60 x **11** = 660 Hz	V_**11** = 1.905 Volts	V_**11** = 1.851 Volts
13th Harmonic	60 x **13** = 780 Hz	V_**13** = 1.058 Volts	V_**13** = 1.182 Volts

The Simulink implementation of the AC grid model including harmonics is shown in Figure 13.

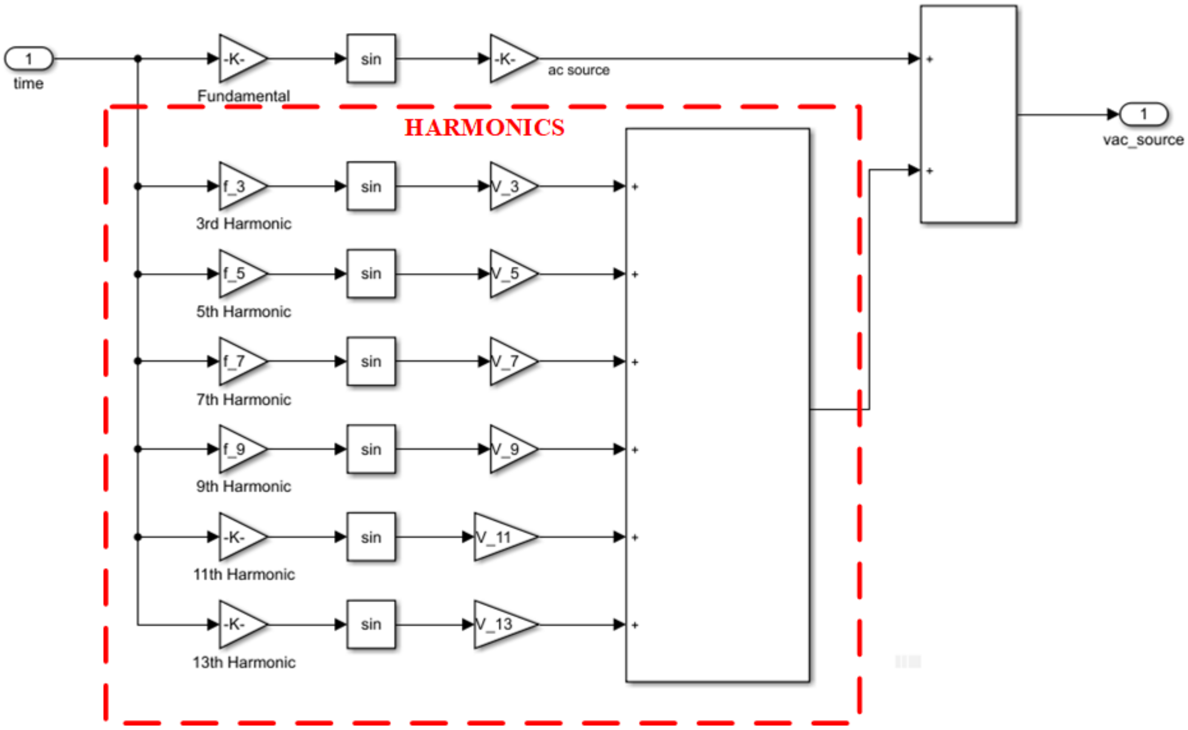

Figure 13. Block diagram of the AC grid voltage algorithm as implemented in Simulink, when harmonics are added

c. AC Grid as Voltage Source with Harmonics and Noise

The last model of the AC grid adds high-frequency noise to the harmonics described in the previous section. Many different definitions exist concerning what noise is and depend on the context in which the term is used (e.g., electronics, signal processing, communication). According to the authoritative dictionary of the Institute of Electrical and Electronics Engineers (IEEE) standard terms, the general term of noise is any “unwanted disturbances superimposed upon a useful signal, which tend to obscure its information content” [12]. In other words, noise, which is a feature of all electric circuits, is the undesirable random fluctuation in a useful signal.

In our AC grid source model, we added a high-frequency noise to further test and compare the different control methodologies. Because the H-bridge inverter’s currents and voltages contain high-frequency components due to the switching of the solid-state switches, it generates electromagnetic interference (EMI). EMI is defined as any disturbance that relates to high-frequency noise and “*may be conducted on the power line or radiated from its source*” [8].

The high-frequency sinewave of a frequency 100 times higher than the fundamental was added to the AC grid voltage ($f_{noise} = 100*f_{fund} = 100*60 = 6$ kHz). Its amplitude is ten times smaller than the amplitude of the nominal AC grid voltage ($V_{noise} = V_{source}/10$). The model of the AC grid voltage including harmonics and high-frequency noise is presented in Figure 14 with Simulink blocks.

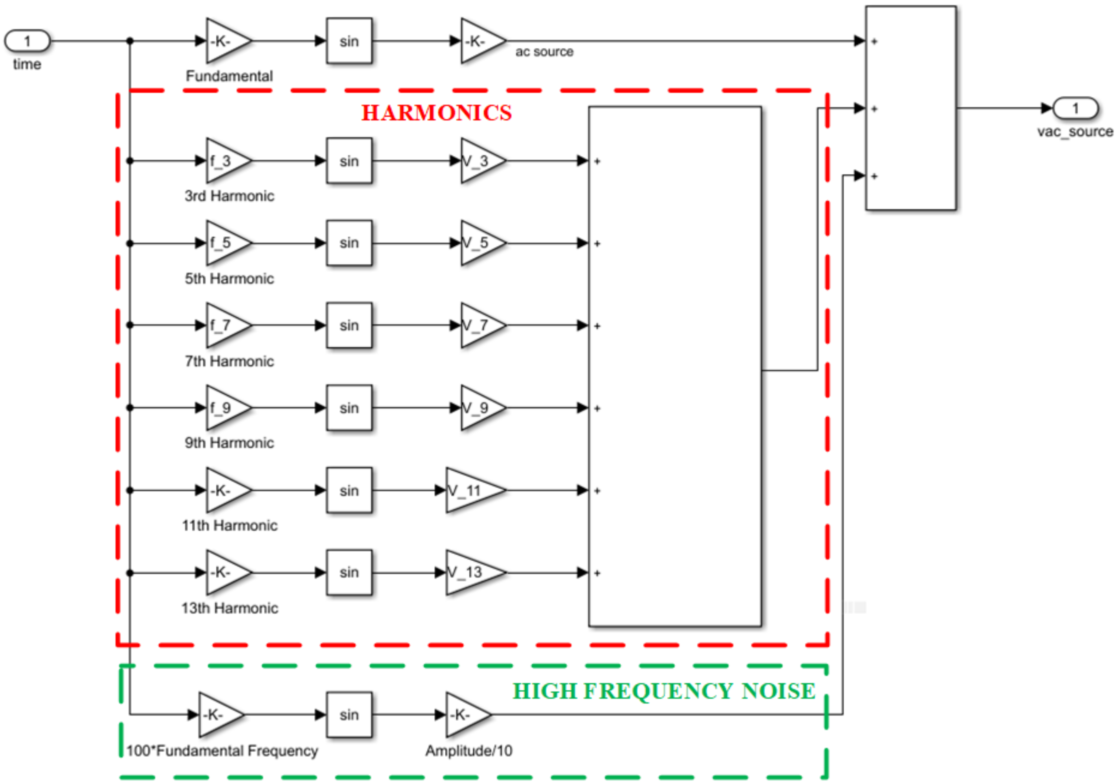

Figure 14. Block diagram of the AC grid voltage algorithm as implemented in Simulink, when harmonics and high-frequency noise are added

2. Orthogonal Generation Methods

In our single-phase microgrid model, we use a DQ synchronous reference frame controller and analyze it in detail. Controllers implemented in the DQ synchronous reference frame are typically used for three-phase inverters; however, they are also used for single-phase inverters by generating fictitious voltages and currents orthogonal to the single-phase voltages and currents. As a consequence, in a single-phase system, where only one phase exists, a second orthogonal phase has to be created. In this thesis, four different methods are used to generate the orthogonal axis components, distinctively affecting the performance of the control strategy in [13]. These methods include: a) the Quarter Cycle Delay method, b) the Differentiation method, c) the Second Order Generalized Integrator (SOGI) method, and d) the All Pass Filter (APF) method. These four Orthogonal Generation Methods (OGM) enable us to determine which method is better in controlling i_{ems} in such way that the power factor is one (unity power factor), and so that a "cleaner" sinusoidal can be implemented. Furthermore, we can determine how each method behaves if harmonics and noise are present.

In Figure 11, the “αβ0 to dq0 TRANSF.” blocks are identical for both voltage and currents; therefore, in the following sections the symbol *X* is used instead of *V* for voltage and *I* for current. For each of the four different OGMs, the analysis, the block diagram, and the proof of the orthogonality of the two axes [13] are presented.

a. Quarter Cycle Delay

In this method, the α-axis, which represents the voltage source, is delayed by one quarter cycle in order to generate the β orthogonal axis. The exact mathematical procedure, the block diagram (shown in Figure 15), and the proof of the orthogonality between the α axis and β axis are shown in equations (18) and (19).

The mathematical form and the Simulink implementation of the equations of the Quarter Cycle Delay method are

$$X_{\alpha}(t) = X_{ac\_source} \Leftrightarrow X_{\alpha}(t) = X_m \sin(\omega_o t) \tag{18}$$

$$X_{\beta}(t) = X_m \sin(\omega_o (t + \frac{3\pi}{2\omega_o})) . \tag{19}$$

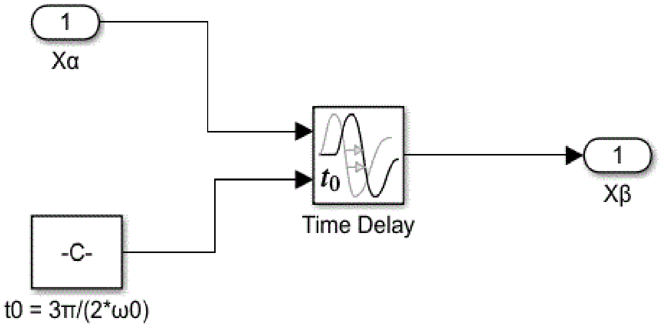

Figure 15. Simulink block diagram for the Quarter Cycle Delay method

The proof of the orthogonality of the two axes is shown in Table 3. First, the voltage and current equations are converted from the time domain to the s-domain, and then the transfer function is calculated and defined by its result if the two axes are orthogonal.

Table 3. Orthogonality of the two axes in the Quarter Cycle Delay method

Axis	Time Domain	S-domain	Transfer Function
A-axis	$X_\alpha(t) = X_m \sin(\omega_o t)$	$X_\alpha(s) = X_m \frac{\omega_o}{s^2+\omega_o^2}$	$H(s) = \frac{X_\beta(s)}{X_\alpha(s)} = e^{j\frac{3\pi}{2\omega_o}s}$ $H(j\omega_o) = -j$ ***Orthogonal***
B-axis	$X_\beta(t) = X_m \sin(\omega_o(t+\frac{3\pi}{2\omega_o}))$	$X_\beta(s) = X_m e^{j\frac{3\pi}{2\omega_o}s} \frac{\omega_o}{s^2+\omega_o^2}$	

The equations in Table 3 demonstrate that the β-axis is orthogonal to the α-axis, because the transfer function between those two axes is –j. In other words, this means that $H(j\omega_o) = -j \;\; = 1\underline{|-90^o}$; so when the α-axis component is in the positive horizontal axis (positive x axis), the β-axis is in the negative perpendicular axis (i.e., negative y axis).

b. Differentiation

In this method, the α-axis, which represents the voltage source, is differentiated to generate the β orthogonal axis. The mathematical form of the differentiation method, the block diagram (shown in Figure 16), and the proof of the orthogonality between the α and β axis are shown in equations (20) and (21).

The equations that show how the differentiation method is implemented and its Simulink block diagram are

$$X_\alpha(t) = X_{ac\_source} \Leftrightarrow X_\alpha(t) = X_m \sin(\omega_o t) \tag{20}$$

$$X_\beta(t) = -\frac{1}{\omega_o}\frac{dX_{ac\_source}}{dt} = -\frac{1}{\omega_o}\frac{d}{dt}(X_m \sin(\omega_o t)) = -X_m \cos(\omega_o t)\,. \tag{21}$$

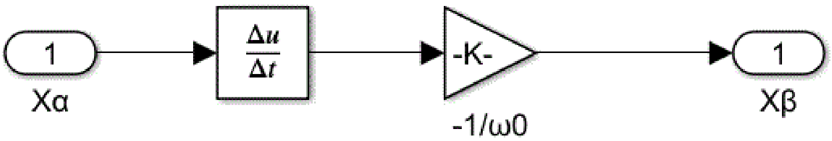

Figure 16. Simulink block diagram for the differentiation method

The equations in Table 4 demonstrate the orthogonality of the two axes. First, the voltage and current equations are converted to the s-domain and then the transfer function is calculated and defined by its result if the two axes are orthogonal.

Table 4. Orthogonality of the two axes in the differentiation method

Axis	**Time Domain**	**S-domain**	**Transfer Function**
A-axis	$X_\alpha(t) = X_m \sin(\omega_o t)$	$X_\alpha(s) = X_m \dfrac{\omega_o}{s^2 + \omega_o^2}$	$H(s) = \dfrac{X_\beta(s)}{X_\alpha(s)} = -\dfrac{s}{\omega_o}$ $H(j\omega_o) = -j$ **Orthogonal**
B-axis	$X_\beta(t) = -X_m \cos(\omega_o t)$	$X_\beta(s) = -X_m \dfrac{s}{s^2 + \omega_o^2}$	

It is clear that the equation of the transfer function in Table 4 is identical to the transfer function of the Quarter Cycle Delay method. Therefore, as already proven, when the α-axis component is in the positive horizontal axis (i.e., positive x axis), the β-axis is in the negative perpendicular axis (i.e., negative y axis), and then those two components are orthogonal.

c. Second Order Generalized Integrator

By implementing this method, the α-axis component is a filtered input signal of the voltage and current of the main grid, and the generated β-axis component is shifted by 90 degrees with respect to the original components in order to have orthogonality [14]. Let us analyze the RLC bandpass filter in Figure 17. Its transfer function is shown in Equation (22) and then it is compared to the equations of the SOGI method in order to observe their similarity:

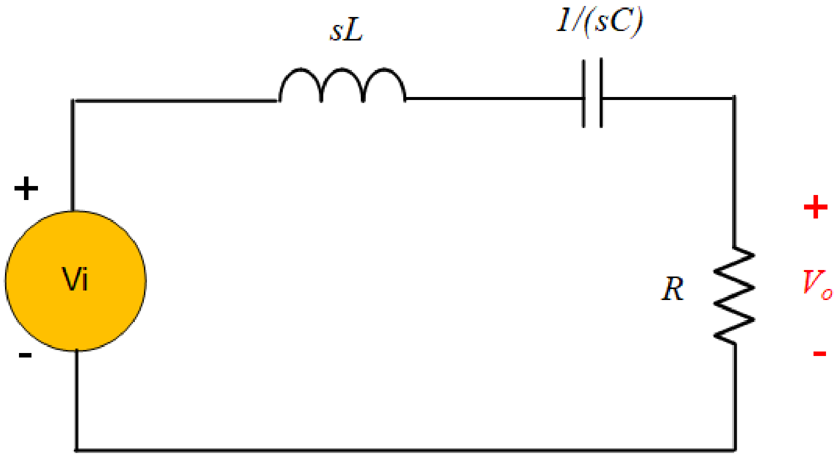

Figure 17. RLC bandpass filter. Source: [10].

$$\mathrm{H}(s)=\frac{V_o(s)}{V_i(s)}=\frac{(R/L)s}{s^2+(R/L)s+1/LC}. \tag{22}$$

Equation (22) can be written in the generalized form of a bandpass filter transfer function by setting $\beta = R/L$ and $\omega_O = \sqrt{1/(LC)}$. Therefore, the general form of any bandpass filter will be:

$$\mathrm{H}(s)=\frac{V_o(s)}{V_i(s)}=\frac{\beta s}{s^2+\beta s+\omega_o^2}, \tag{23}$$

where ω_o is the center frequency and β the bandwidth of that type of filter.

The mathematical form and the Simulink implementations (Figure 18) of the equations of the SOGI method follow.

$$\mathrm{H}_1(s)=\frac{X_a(s)}{X_{ac\_source}(s)}=\frac{k\omega_o s}{s^2+k\omega_o s+\omega_o^2} \tag{24}$$

$$\mathrm{H}_2(s)=\frac{X_\beta(s)}{X_{ac\_source}(s)}=\frac{k\omega_o^2}{s^2+k\omega_o s+\omega_o^2}. \tag{25}$$

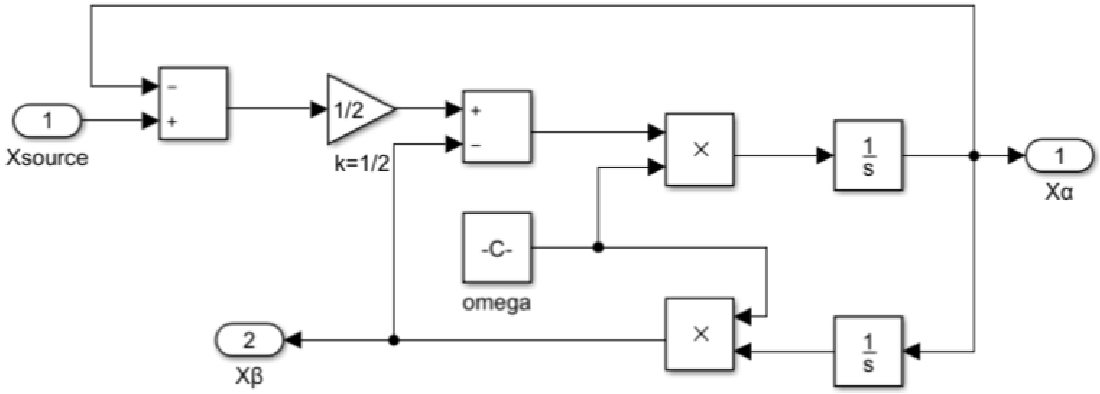

Figure 18. Block diagram for the SOGI method. Source: [14].

Comparing equations (23) and (24), it can be observed that the $H_1(s)$ transfer function behaves as a band pass filter with a center frequency of ω_o and a bandwidth of $\beta = k\omega_o$.

Finally, equations (24) and (25) are compared in Table 5. The orthogonality of the two axes components is proven, and therefore, it can be concluded that the $H_2(s)$ is a 90-degree phase shift signal with respect to $H_1(s)$.

Table 5. Orthogonality of the two axes in the SOGI method

Axis	**S-domain**	**Transfer Function**
A-axis	$\mathrm{H}_1(s) = \dfrac{X_a(s)}{X_{ac\_source}(s)} = \dfrac{k\omega_o s}{s^2 + k\omega_o s + \omega_o^2}$	$H(s) = \dfrac{\mathrm{H}_2(s)}{\mathrm{H}_1(s)} = \dfrac{V_\beta(s)}{V_\alpha(s)} = \dfrac{k\omega_o^2}{k\omega_o s} = \dfrac{\omega_o}{s}$ $H(j\omega_o) = -j$ ***Orthogonal***
B-axis	$\mathrm{H}_2(s) = \dfrac{X_\beta(s)}{X_{ac\_source}(s)} = \dfrac{k\omega_o^2}{s^2 + k\omega_o s + \omega_o^2}$	

As it can been noticed, the transfer function between the α-axis and β-axis components has the same result as compared with the transfer functions of the previous methods. Therefore, it can be concluded that the α-axis and β-axis components are orthogonal to each other.

d. All Pass Filter

The last method is an All Pass Filter (APF) method, which uses a Kalman-based filter estimator. In this procedure, a Kalman-based filter is designed [15] and, by selecting the appropriate gains (k_e and k_f), an all pass filter is created. In order to create the two orthogonal axes, the value of k_e has to be equal to $-k_f$. In our simulation, different values are evaluated and compared to each other in order to observe the performance of this method.

To better convey that the output signal is an APF, its transfer function is shown in Figure 19 and Equation (26).

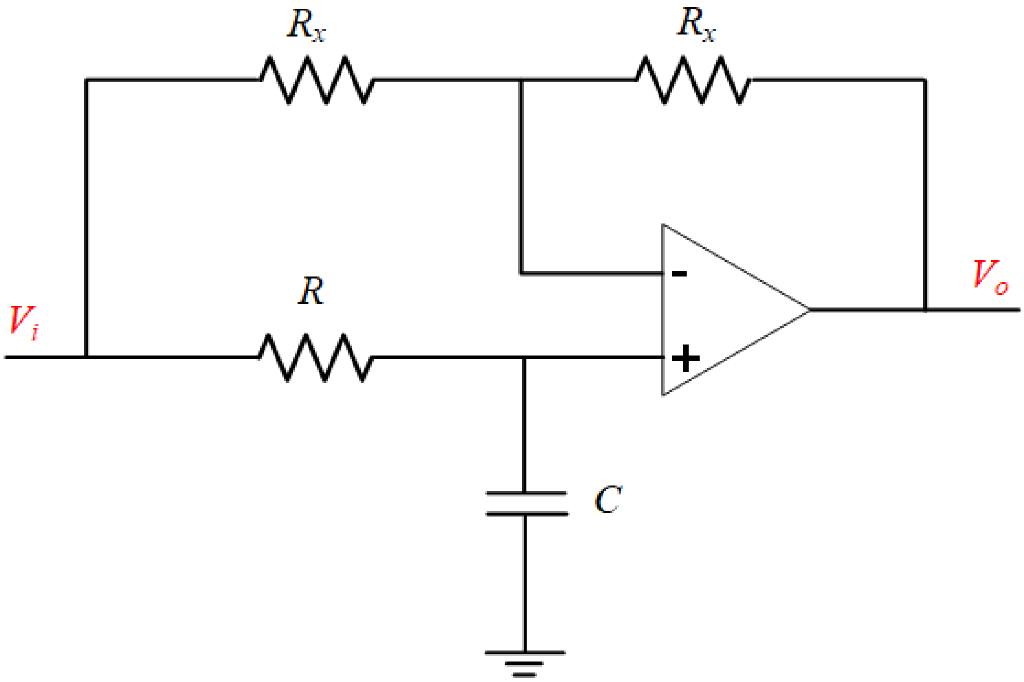

Figure 19. First order All Pass Filter. Source: [16].

In Figure 19, a first-order APF is shown with transfer function [16]:

$$H(s)=\frac{V_o(s)}{V_i(s)}=-\frac{s-\dfrac{1}{RC}}{s+\dfrac{1}{RC}}. \tag{26}$$

Equations (27) and (28) show how the APF method is implemented, and its Simulink block diagram is provided in Figure 20:

$$\mathrm{H}_1(s)=\frac{X_a(s)}{X_{ac\_source}(s)}=\frac{k_e s-\omega_o k_f}{s^2+k_e s+\omega_o^2-\omega_o k_f}\overset{k_f=-k_e}{=}\frac{k_e s+k_e\omega_o}{s^2+k_e s+\omega_o^2+\omega_o k_e}=\frac{k_e(s+\omega_o)}{s^2+k_e s+\omega_o^2+\omega_o k_e} \qquad (27)$$

$$\mathrm{H}_2(s)=\frac{X_\beta(s)}{X_{ac\_source}(s)}=\frac{k_f s+\omega_o k_e}{s^2+k_e s+\omega_o^2-\omega_o k_f}\overset{k_f=-k_e}{=}\frac{-k_e s+\omega_o k_e}{s^2+k_e s+\omega_o^2+\omega_o k_e}=\frac{k_e(-s+\omega_o)}{s^2+k_e s+\omega_o^2+\omega_o k_e}. \qquad (28)$$

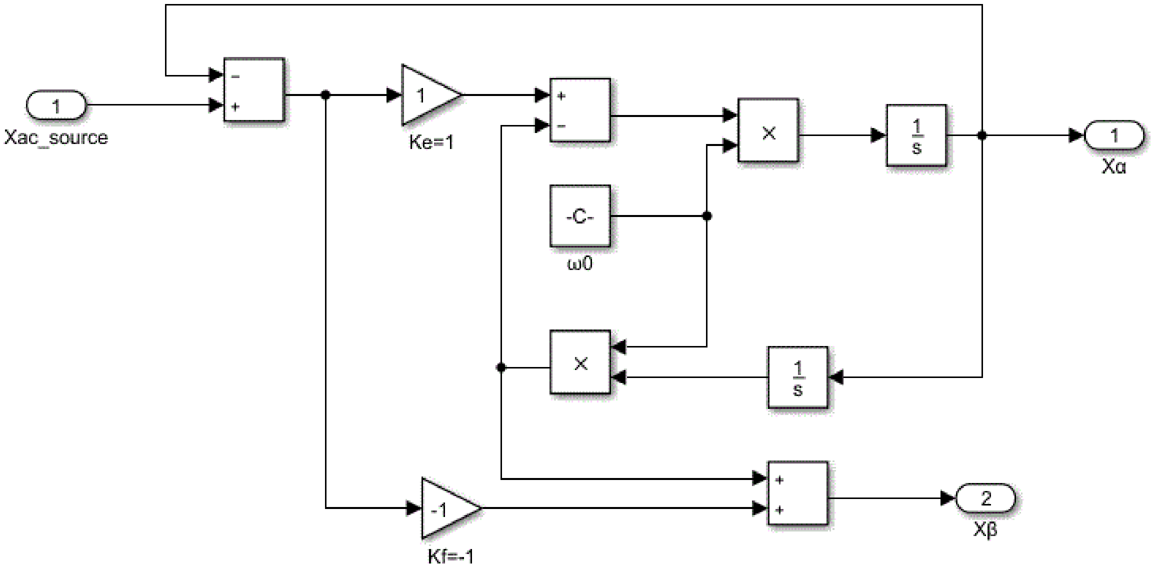

Figure 20. Block diagram for the APF method. Source: [15].

The transfer function of $\mathrm{H}_1(s)$ and $\mathrm{H}_2(s)$ will be:

$$H(s)=\frac{\mathrm{H}_2(s)}{\mathrm{H}_1(s)}=\frac{X_\beta(s)}{X_\alpha(s)}=\frac{-s+\omega_o}{s+\omega_o}=-\frac{s-\omega_o}{s+\omega_o}. \qquad (29)$$

Comparing equations (26) and (29), it can be observed that the H(s) transfer function behaves as an APF with $\omega_o = 1/(RC)$.

The equations in Table 6 show the orthogonality of the two axes. The s-domain equations of voltage and current are used, and then the transfer function is calculated and defined by its result if the two axes are orthogonal.

Table 6. Orthogonality of the two axes in the APF method

S-domain	**Transfer Function**
$H_1(s)=\frac{X_a(s)}{X_{ac\_source}(s)}=\frac{k_e s-\omega_o k_f}{s^2+k_e s+\omega_o^2-\omega_o k_f}\overset{k_f=-k_e}{=}\frac{k_e(s+\omega_o)}{s^2+k_e s+\omega_o^2+\omega_o k_e}$	$H(s)=\frac{H_2(s)}{H_1(s)}=\frac{X_\beta(s)}{X_\alpha(s)}=\frac{k_e(-s+\omega_o)}{k_e(s+\omega_o)}$ $H(j\omega_o)=\frac{-j\omega_o+\omega_o}{j\omega_o+\omega_o}=\frac{-j+1}{j+1}=-j$ ***Orthogonal***
$H_2(s)=\frac{X_\beta(s)}{X_{ac\_source}(s)}=\frac{k_f s+\omega_o k_e}{s^2+k_e s+\omega_o^2-\omega_o k_f}\overset{k_f=-k_e}{=}\frac{k_e(-s+\omega_o)}{s^2+k_e s+\omega_o^2+\omega_o k_e}$	

The transfer function between the α-axis and β-axis component is similar to the transfer functions of the previous methods, and as a consequence, the α-axis and β-axis components are orthogonal to each other.

3. DQ Synchronous Reference Frame for a Single-Phase Microgrid

In the proposed controller, first the two orthogonal components are created; then the DQ (or else Park) transformation is used to create the two DQ components for the voltage (v_d , v_q) and for the current (i_d ,i_q).

The DQ synchronous reference frame is most often used in the analysis of either a single-phase or a three-phase system, because all time-varying state variables become DC [17] in this reference frame. As a consequence, the analysis of an AC system is easier done by transforming currents and voltages to DC components. This is because “for DC converters it is quite simple to design linear current controllers with no steady state error, but if the AC controllers are designed the same way as DC controllers, a significant steady state error in both amplitude and phase may occur” [18]. Figure 21 shows a schematic view of the relationship between the α-β and d-q axes, where θ is the angle between the two axes.

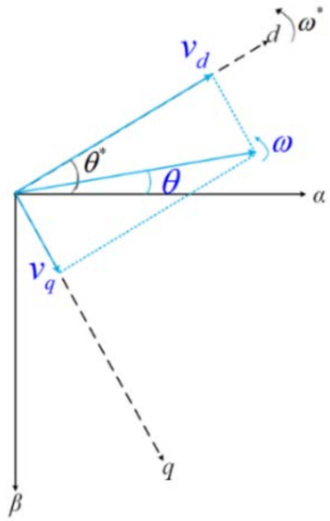

Figure 21. Axes α-β and d-q. Source: [19].

In order to convert the AC voltage of the single-phase grid to our desired DC component, the angle between the α-β and d-q axes has to lock to θ^*. In that way, the d-axis will follow the voltage of the main grid and simultaneously the voltage of q-axis will be zero. The previously mentioned lock of the angle will take place by the use of the phase-locked loop (PLL), which is as detailed in the following subsection.

The mathematical equation that transforms variables from the α-β to d-q reference frame is

$$\begin{bmatrix} d \\ q \end{bmatrix} = \begin{bmatrix} \cos(\theta^*) & \sin(\theta^*) \\ -\sin(\theta^*) & \cos(\theta^*) \end{bmatrix} \begin{bmatrix} \alpha \\ \beta \end{bmatrix}. \tag{30}$$

As a result, the values of the voltages and currents will be converted from the α-β axis to the d-q axis as follows.

- Voltage

$$v_d = v_\alpha \cos(\theta^*) + v_\beta \sin(\theta^*) \tag{31}$$

$$v_q = -v_\alpha \sin(\theta^*) + v_\beta \cos(\theta^*). \tag{32}$$

- Current

$$i_d = i_\alpha \cos(\theta^*) + i_\beta \sin(\theta^*) \tag{33}$$

$$i_q = -i_\alpha \sin(\theta^*) + i_\beta \cos(\theta^*). \tag{34}$$

4. Phase-Locked Loop

According to Goldman, a PLL "synchronizes the output phase and frequency of a controllable oscillator to match the output phase and frequency of a reference oscillator. Ideally, the steady-state condition will show a zero difference in phase and frequency between the controlled oscillator output and the reference output" [20].

Figure 22 shows the αβ0 to dq0 transformation and the block diagram of the PLL [19].

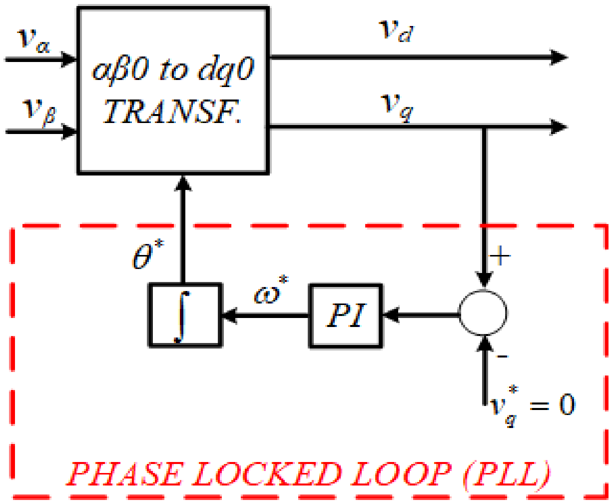

Figure 22. Synchronous reference frame PLL. Source: [19].

In our model, the PLL of Figure 22 is used to lock the angle θ^*. The reference voltage of the q axis is set to be zero ($v_q^* = 0$) for the reasons already mentioned.

5. Power Calculation for DQ Theory

After creating the DQ axis and calculating the two DC components for the voltage (v_d, v_q) and the two DC components for the current (i_d, i_q), we can calculate the values of active and reactive power as those presented in [14]:

$$P = \frac{1}{2}(v_d i_d + v_q i_q) \tag{35}$$

$$Q = \frac{1}{2}(v_q i_d - v_d i_q) . \tag{36}$$

The P and Q values computed with equations (35) and (36) are then filtered by a Low Pass Filter (LPF) and compared to the references, which are the desired values of P and Q.

6. Low Pass Filter

As mentioned previously, an LPF is used in our model. The purpose of this LPF is to remove any unwanted noise. An LPF passes signals that have a frequency lower than the filter's cutoff frequency. In our model the fundamental frequency is 60 Hz; an LPF with a 200 Hz cutoff frequency is used. As a result, any kind of undesired signal with frequency components greater than 200 Hz will be rejected.

7. Calculation of Instantaneous Active and Reactive Current

After the LPF, a Proportional-Integral (PI) controller produces the reference DQ currents i_d^* and i_q^*, which are transformed to the stationary frame into i_α^* and i_β^*. This transformation has been implemented with two different methods; the first method is shown in Figures 23:

a. First Method: DQ0 to AB0 Transformation

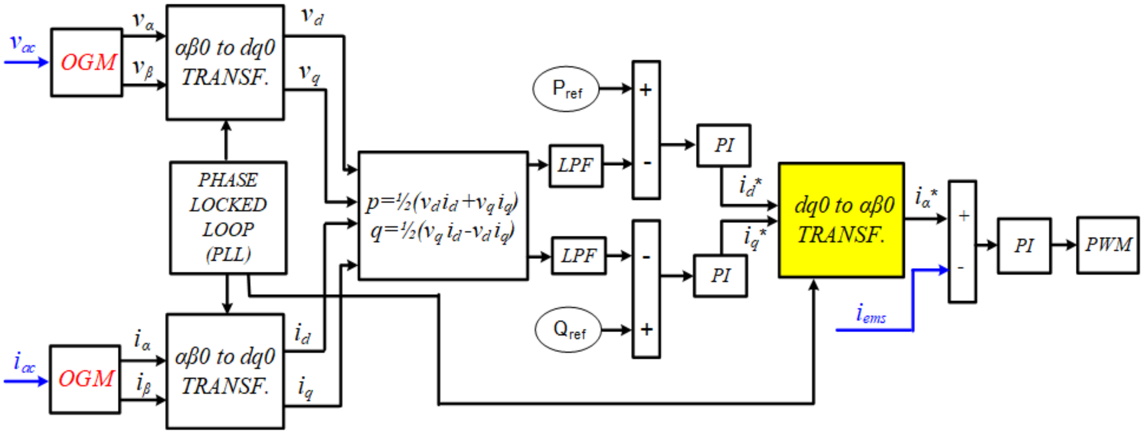

Figure 23. Block diagram of a P-Q source power flow controller using DQ0 to AB0 transformation

As it can be observed from Figure 23, a dq0 to αβ0 transformation is implemented. In this part, the same PLL is used as before because the angle θ^*, as shown in Figure 21, is the angle between the d-q and α-β axes. The mathematical equation that relates those two axes for the dq0 to αβ0 transformation is

$$\begin{bmatrix} \alpha \\ \beta \end{bmatrix} = \begin{bmatrix} \cos(\theta^*) & -\sin(\theta^*) \\ \sin(\theta^*) & \cos(\theta^*) \end{bmatrix} \begin{bmatrix} d \\ q \end{bmatrix}. \tag{37}$$

As a result, the values of the currents will be converted from the d-q axis to α-β as follows.

$$i_\alpha^* = i_d^* \cos(\theta^*) - i_q^* \sin(\theta^*) \tag{38}$$

$$i_\beta^* = i_d^* \sin(\theta^*) + i_q^* \cos(\theta^*) \tag{39}$$

b. *Second Method: Using an Equation*

A second method to compute the instantaneous active and reactive current has been implemented. Its block diagram is highlighted in Figure 24.

•

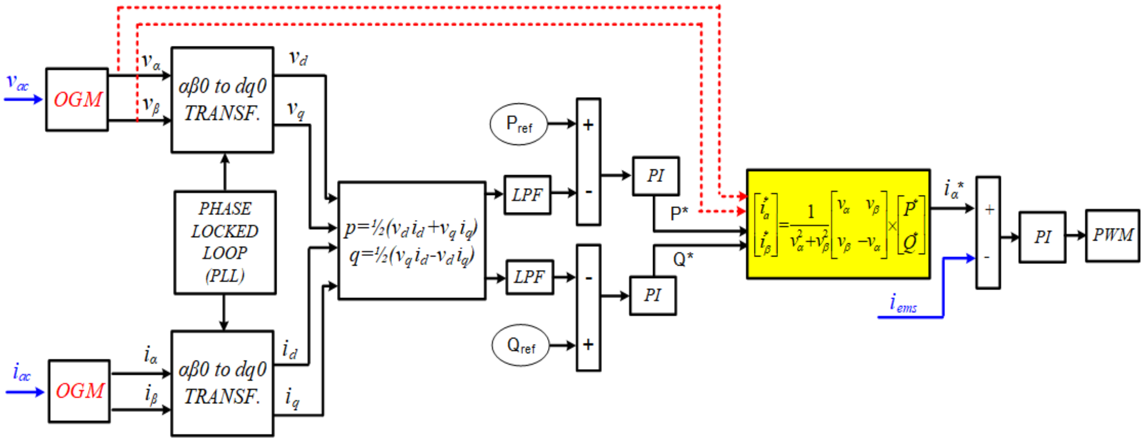

Figure 24. Block diagram of a P-Q source power flow controller using an equation

Taking into consideration [4], [14], and [21], the following matrix equation yields the α–β reference frame currents.

$$\begin{bmatrix} i_\alpha^* \\ i_\beta^* \end{bmatrix} = \frac{1}{v_\alpha^2 + v_\beta^2} \begin{bmatrix} v_\alpha & v_\beta \\ v_\beta & -v_\alpha \end{bmatrix} \times \begin{bmatrix} P^* \\ Q^* \end{bmatrix} \tag{40}$$

In both methods i_{β}^{*} is neglected since this is a single-phase microgrid, and i_{α}^{*} is the reference used to control the EMS current, i_{ems}.

8. Simulink Model

In Figure 25, the Simulink model of the P-Q power flow controller is illustrated, and the individual components are highlighted with dashed blocks.

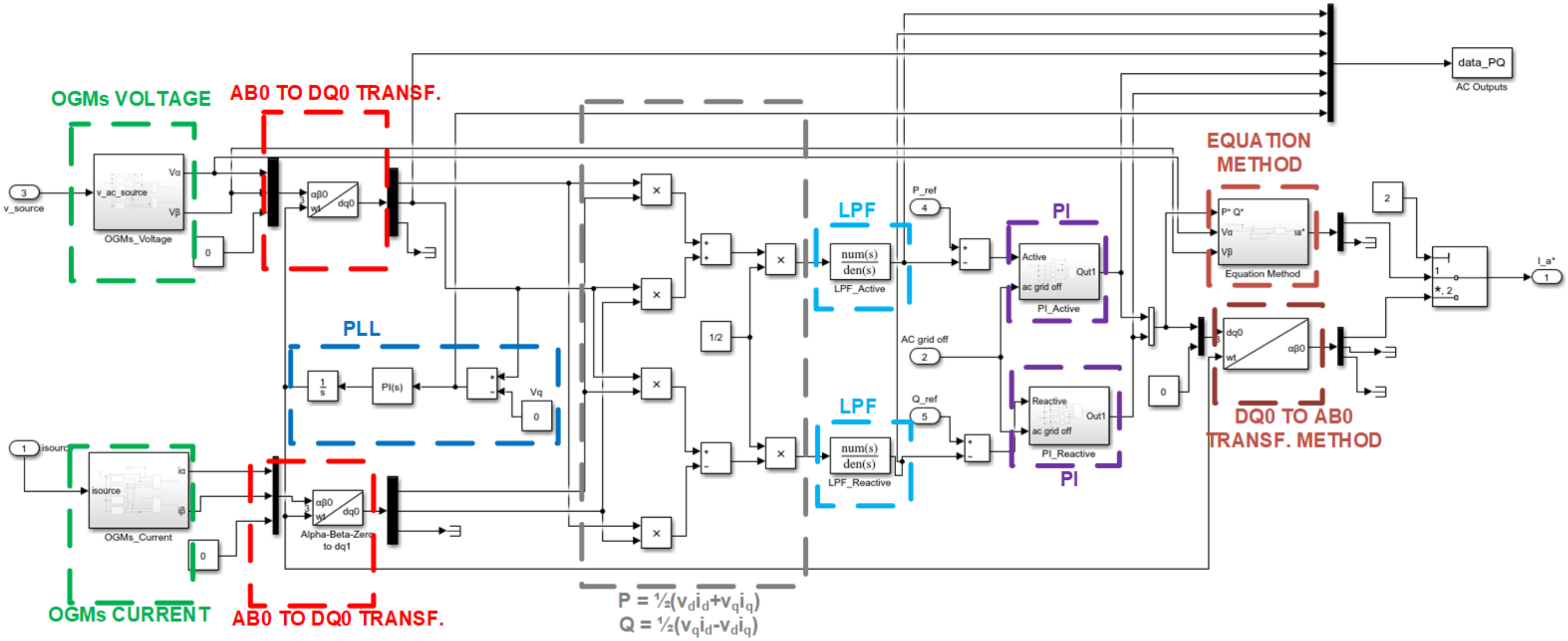

Figure 25. SIMULINK model of the P-Q power flow controller

B. PWM INVERTER

The final part of the controller, implemented with another PI, is executed in the stationary frame, producing the command voltage signal for the PWM generator. In this PI controller, the input is the error between the reference ($i_\alpha^* = i_{ems}^*$) and the measured EMS current (i_{ems}). The functionality of the PWM has already been described in Chapter III where the H-bridge inverter is presented. Figure 26 shows how the PWM algorithm is implemented in the Simulink model. The dashed lines show the Simulink implementation of the blocks previously shown in Figure 10.

Initially, in the case of a grid connected microgrid, the inputs are the reference i_{ems}^* and the measured i_{ems}. Otherwise, if the main grid cannot supply our microgrid, a switch will be activated in order to convert the functionality of the EMS from a current-controlled source to a voltage-controlled source. In both cases, after the switch, a duty cycle control input signal is created. Furthermore, as illustrated in Figure 26, the triangle waveform is generated with a fixed switching frequency and a constant peak amplitude. In our case, we set $f_s = 15$ kHz and the peak is varied from -1 to 1. Finally, the comparison of the signal-level control voltage and the triangle signal produces the desired duty cycle control signal.

The Simulink model allows simulations to be run with either unipolar or bipolar PWM. The type of PWM can be determined by assigning the value zero for unipolar or one for bipolar to the variable PWM_mode defined in the MATLAB initial condition file (included in the Appendix). In this thesis, the unipolar mode is used, because it yields better performance at the output of the inverter.

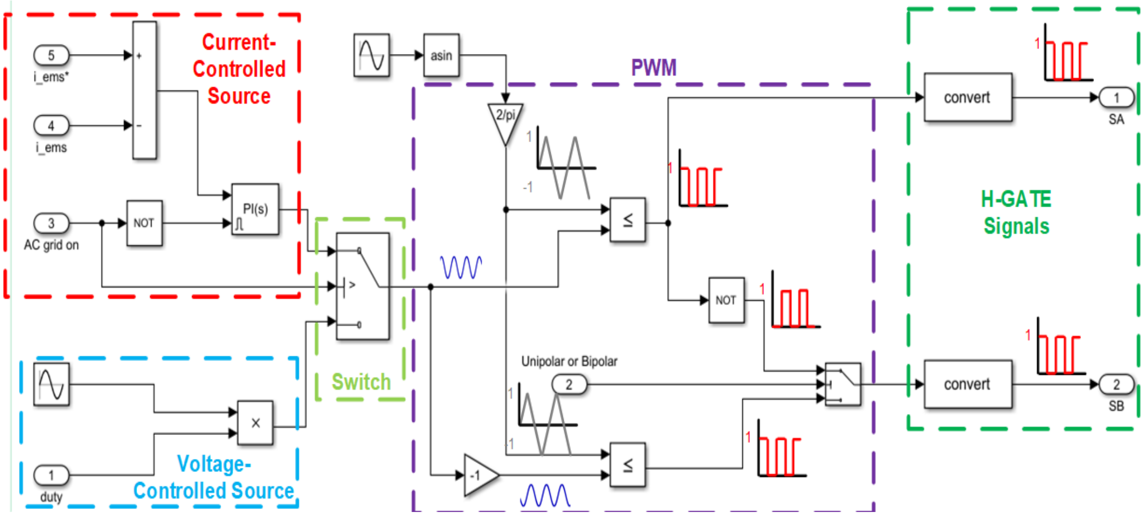

Figure 26. Simulink model of PWM

C. INVERTER OUTPUT FILTER

In Figure 27, the Simulink model of the H-bridge output filter can be observed. The filter converts the pulse signal waveform from the output of the H-bridge inverter to the desired sinusoidal signals. This can also be easily noticed from Figure 27 and how its blocks act in order to have our desired i_{ems} signal. Note that the inverter is controlled as a current source when it is grid-connected, which is the case analyzed in this thesis.

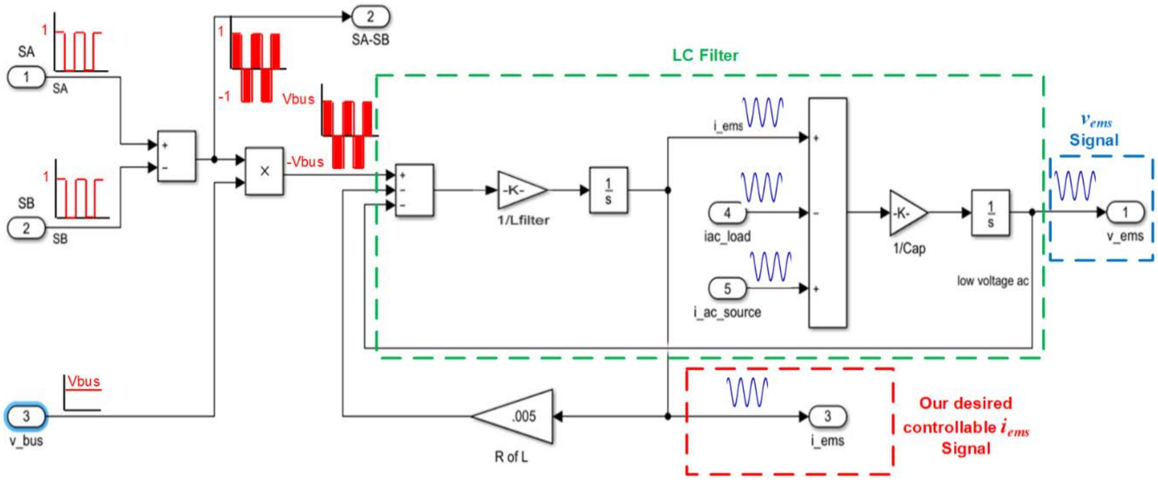

Figure 27. Simulink model of inverter output filter

The combination of H-gate signals, which produce the duty cycles for the inverter switches, and the DC bus voltage, which creates the amplitude, will lead to the inverter output voltage, which then after integration will contribute to the generation of the desired controllable i_{ems} signal.

Two differential equations model the LC filter at the output of the H-bridge inverter. Initially, by observing our circuit in Figure 10, we note that Kirchoff's current law in the Laplace domain can be applied at the node that connects the EMS, the AC source, the load current, and the current through the capacitor

$$i_{ems} - i_{load} + i_{ac} - i_{cap} = 0\,, \tag{41}$$

where

$$i_{cap} = s v_{ems} C_{cap}\,. \tag{42}$$

Therefore,

$$v_{ems} = \left(\frac{1}{C_{cap}}\right) * \left(\frac{1}{s}\right) * (i_{ems} - i_{load} + i_{ac}) \tag{43}$$

$$i_{ems} = \frac{V_{bus} - V_{ems}}{sL_{filter} + R}\,. \tag{44}$$

D. COMMENTS

Recall that the EMS provides ancillary services such as reactive power control [7]. This can be implemented in many ways, with and without the use of a DQ frame [13], [17], [21]. Although many DQ control strategies have been reported in the literature for single-phase inverters, for both grid-connected [21], [22] and islanding mode of operation [13], [17], no previous work makes a comparison of the DQ control strategies, except in a qualitative way [13]. This makes it challenging for engineers to appreciate the differences between Orthogonal Generation Methods. Chapter V includes a detailed analysis of the impact that these four previously detailed OGMs have on the control of active and reactive power (P-Q) flow in a single-phase inverter. Furthermore, a control strategy is used, spanning both stationary and synchronous reference frames, identifying an easy method to implement the entire controller into a Field Programmable Gate Array (FPGA).

V. SIMULATION RESULTS

We developed a physics-based model of the EMS with its control system and used the model to simulate different scenarios with the objective of observing how the performance of the proposed controller varies according to different OGMs. The values of the load inductors, resistors, and capacitors that have been chosen for the circuit of Figure 28 are the same as those tested in the laboratory.

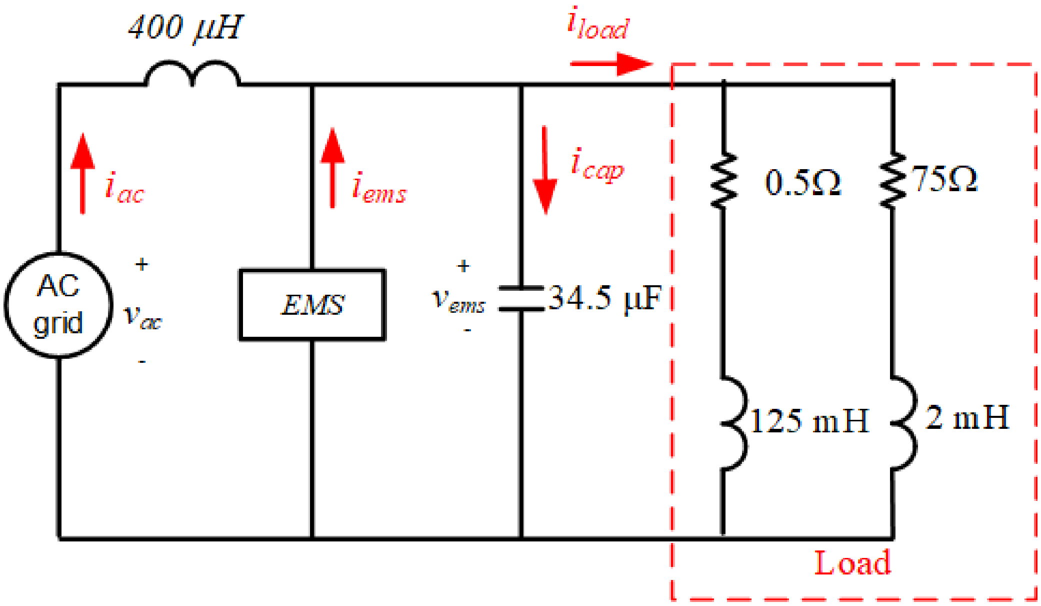

Figure 28. Simplified electric circuit for EMS testing

In this chapter, simulated plots are presented for the three different AC grid models detailed in Chapter IV: i) ideal source, ii) source with only harmonics, and iii) source with harmonics and high-frequency noise. Moreover, for each of these cases, two different methods of controls have been tested with the two derivations of the EMS reference current presented in the previous chapter: a) DQ0 to AB0 transformation and b) Use of an equation. Figure 29 depicts the model of the loads as they have been implemented in Simulink.

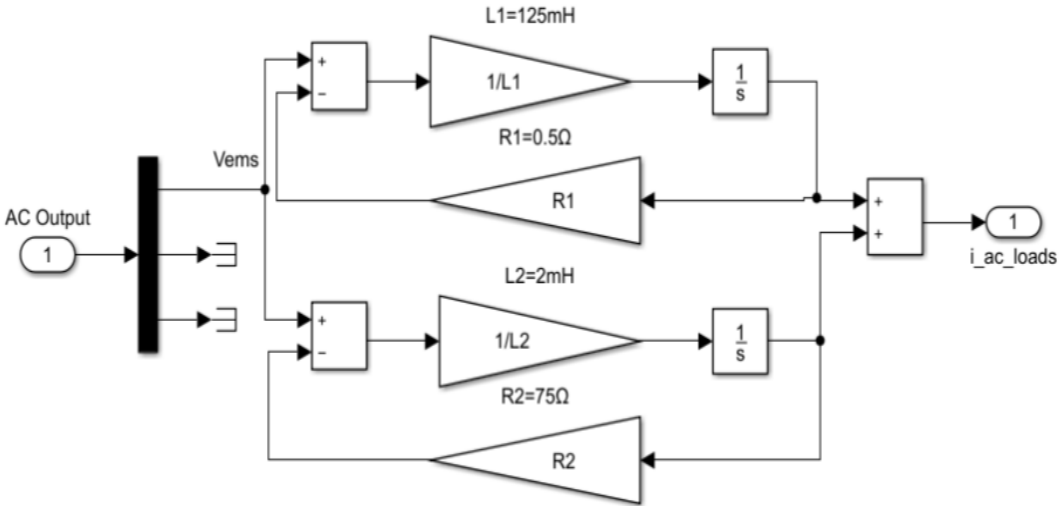

Figure 29. Simulink model of the loads

Table 7 illustrates all the possible cases tested. The figures have been divided into two categories: a) P-Q figure, where the simulated active and reactive power are shown; and b) EMS current, source current, and source voltage, where the phase error is observed. Moreover, for the SOGI method, the value of k that has been used is $k=1/2$, and for the APF method, $k_e=-\ k_f=1$. Finally, our comparison takes place only for the steady state portion.

Table 7. Simulated cases tested

	CASES	**Control Method**	**OGM**	**Figures**	
				v_{ac} ,i_{ac}, i_{ems}	**P-Q**
1	Ideal Voltage Source	DQ0 to AB0 Transf.	Quarter Cycle Delay	Figure 30	Figure 31
			Differentiation		
			SOGI		
			APF		
			All OGMs (zoom in)		
			All OGMs (except Different.Method)		
2	Ideal Voltage Source	Use of an Equation	Quarter Cycle Delay	Figure 32	Figure 33
			Differentiation		
			SOGI		
			APF		
			All OGMs (zoom in)		

	CASES	Control Method	OGM	Figures	
				v_{ac}, i_{ac}, i_{ems}	P-Q
			All OGMs (except Different.Method)		
3	Source with Harmonics only	DQ0 to AB0 Transf.	Quarter Cycle Delay	Figure 34	Figure 35
			Differentiation		
			SOGI		
			APF		
			All OGMs		
			All OGMs (except Different.Method)		
4	Source with Harmonics only	Use of an Equation	Quarter Cycle Delay	Figure 36	Figure 37
			Differentiation		
			SOGI		
			APF		
			All OGMs		
			All OGMs (except Different.Method)		
5	Voltage Source with Harmonics and Noise	DQ0 to AB0 Transf.	Quarter Cycle Delay	Figure 38	Figure 39
			Differentiation		
			SOGI		
			APF		
			All OGMs		
			All OGMs (except Different.Method)		
6	Voltage Source with Harmonics and Noise	Use of an Equation	Quarter Cycle Delay	Figure 40	Figure 41
			Differentiation		
			SOGI		
			APF		
			All OGMs		
			All OGMs (except Different.Method)		

A. SIMULATED CASES FOR THE FOUR OGMS IN STEADY STATE

1. Ideal Source—DQ0 to AB0 Transformation Control Method

From Figure 30 it can be concluded that the angle difference between the voltage and the current at the grid is zero or, in other words, that all the OGMs present unity power factor at the source. Furthermore, Figure 31 shows that in the case of an ideal source and when the DQ0 to AB0 transformation control method is used, the commanded active and reactive power are equal to the measured active and reactive power, respectively. ***Therefore, the implementation of active and reactive power control flow has been accomplished.*** Although the differentiation method presents a slight amount of noise, it does not significantly affect the system performance.

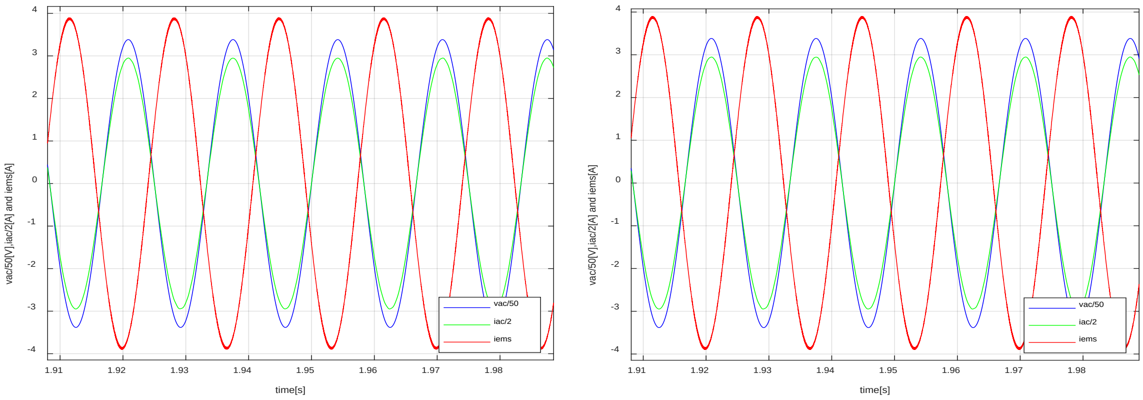

a) Quarter Cycle Delay method

b) Differentiation method

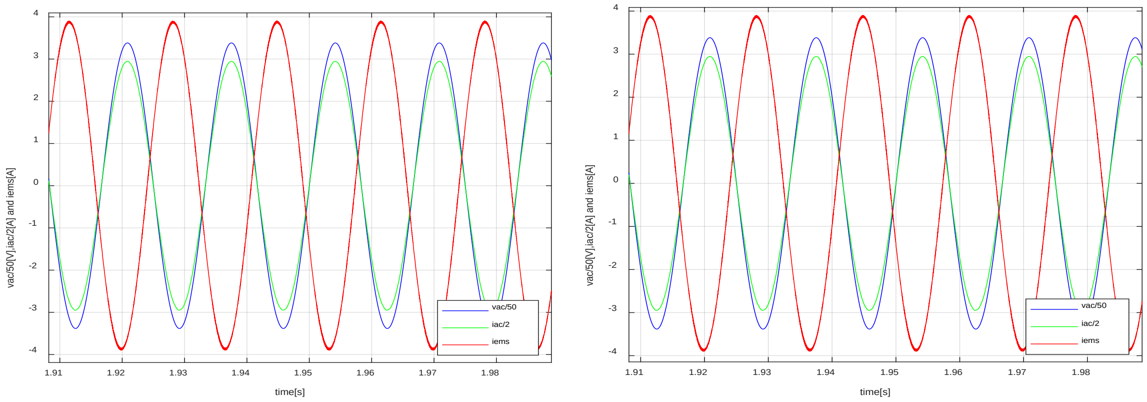

c) SOGI method

d) APF method

Figure 30. Source current, source voltage, and EMS current for an ideal source by using the DQ0 to AB0 transformation control method

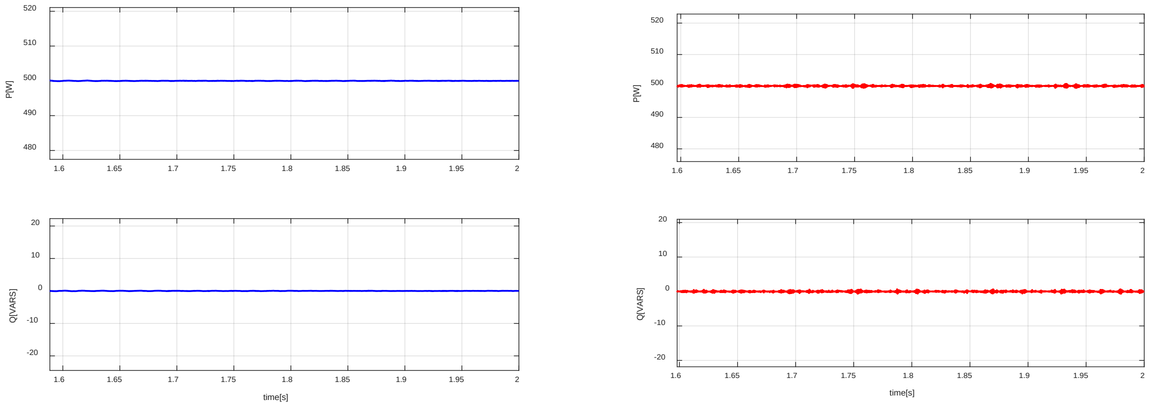

a) Quarter Cycle Delay method b) Differentiation method

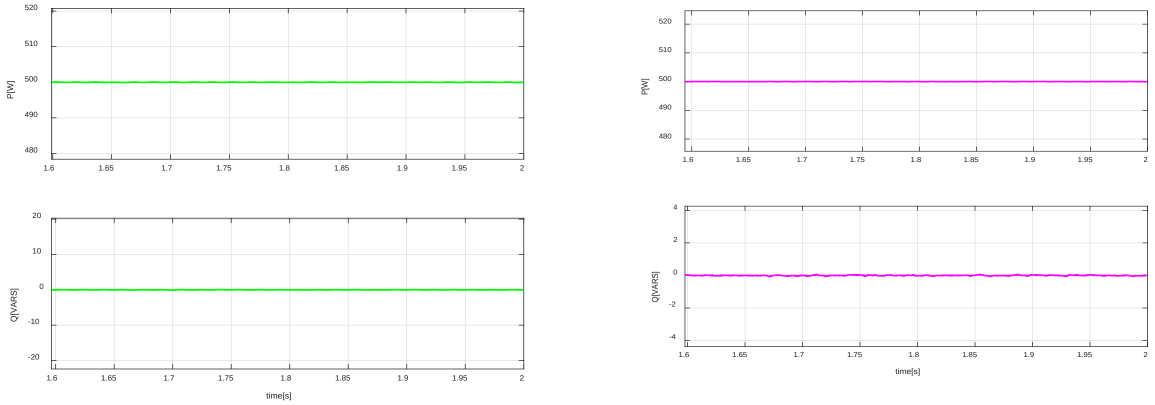

c) SOGI method d) APF method

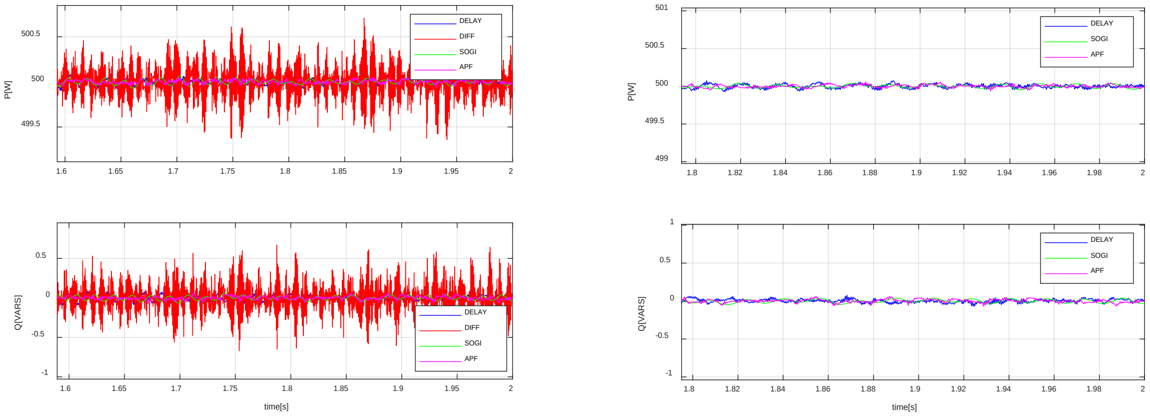

(e) All OGMs (zoom in) (f) All OGMs (except differentiation)

Figure 31. P commanded to 500 W and Q commanded to 0 VARS for an ideal source by using the DQ0 to AB0 transformation control method

2. Ideal Source—Equation Control Method

It is clear that the two different control methods for an ideal source have exactly the same results. Characteristically, from Figure 32, it can be concluded that the angle difference between the voltage and the current at the grid is zero or, in other words, that all the OGMs result in unity power factor at the source. Moreover, Figure 33 shows that in the case of an ideal source, and when the equation control method is used, the commanded active power and the reactive power are equal to the measured active and reactive powers, respectively. ***Therefore, the implementation of active and reactive power control flow has been accomplished.***

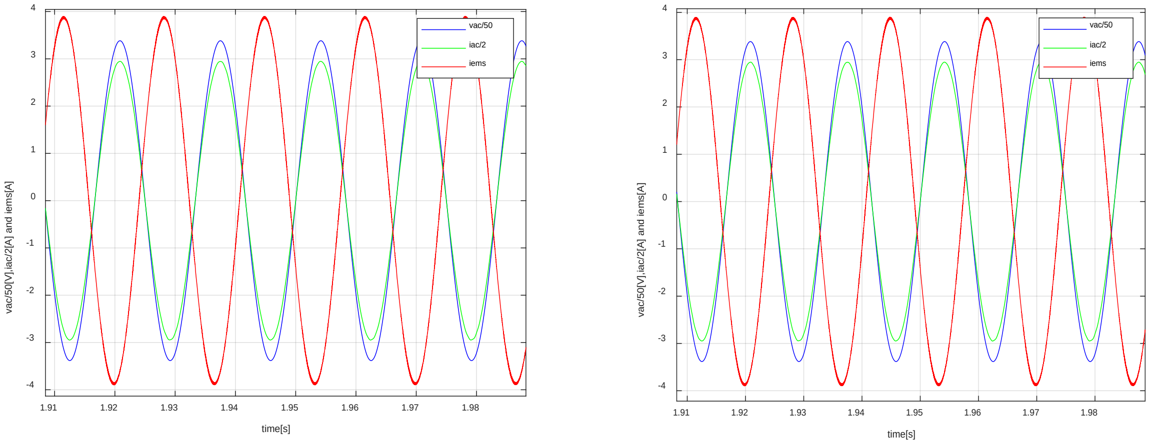

a) Quarter Cycle Delay method

b) Differentiation method

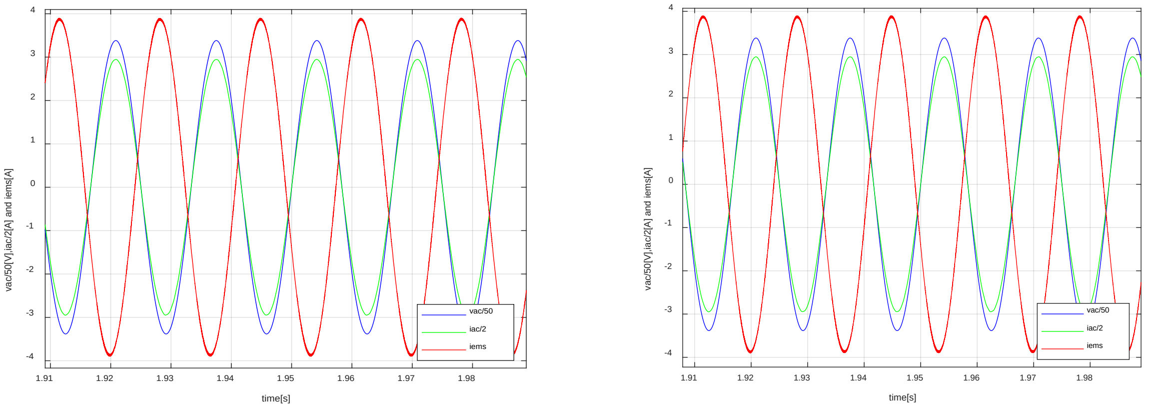

c) SOGI method

d) APF method

Figure 32. Source current, source voltage, and EMS current for an ideal source by using the equation control method

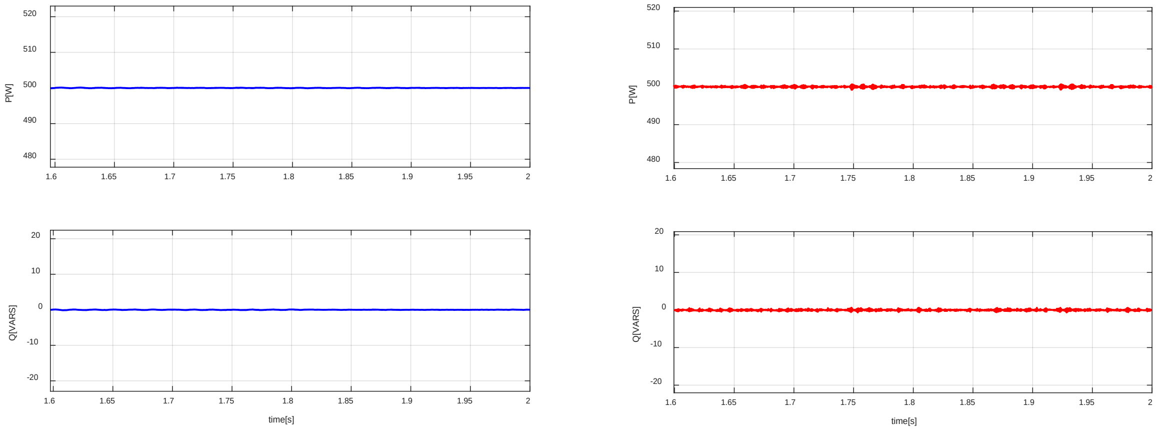

a) Quarter Cycle Delay method b) Differentiation method

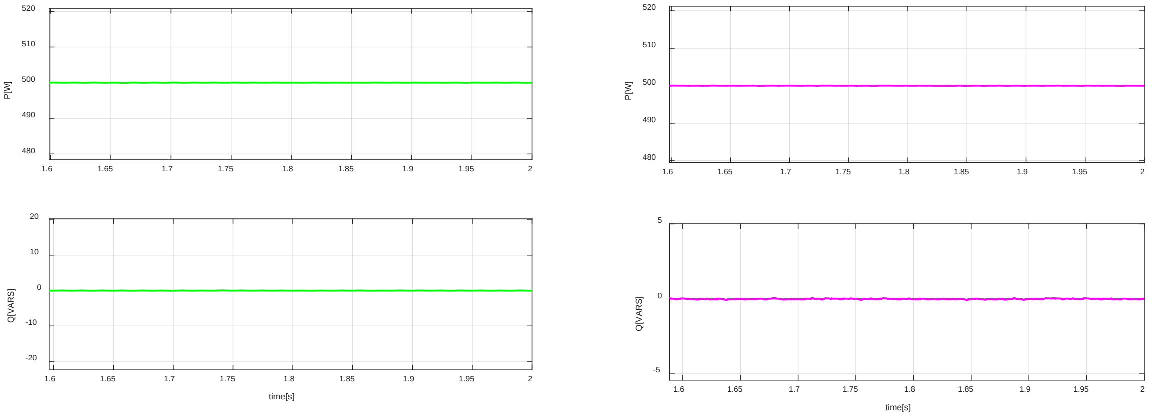

c) SOGI method d) APF method

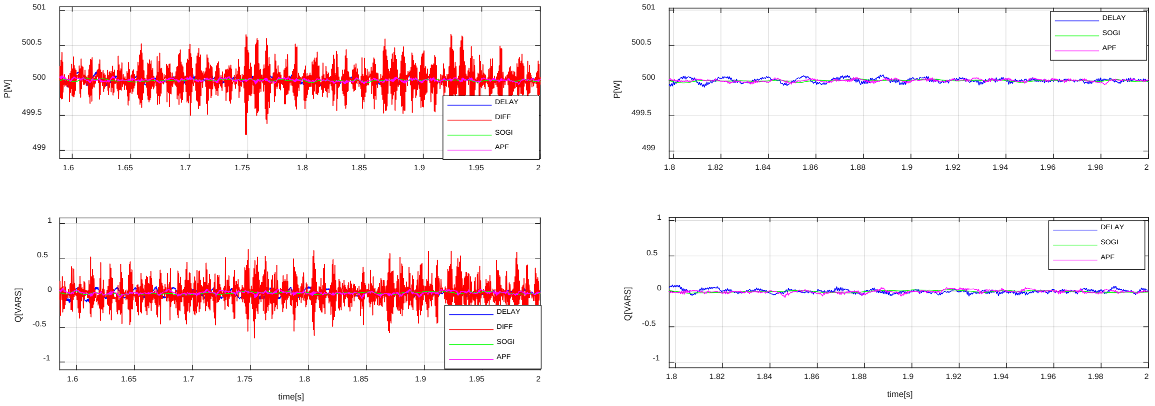

(e) All OGMs (zoom in) (f) All OGMs (except differentiation)

Figure 33. P commanded to 500 W and Q commanded to 0 VARS for an ideal source by using the equation control method

3. Source with Harmonics Only—DQ0 to AB0 Transformation Control Method

Having added harmonics to the model of the AC grid voltage, the case of the DQ0-to-AB0 transformation control method has been tested first. Figure 34 illustrates that in all OGMs, the voltage and the current at the grid are in phase. Additionally, Figure 35 shows that the performance of the SOGI method is not affected at all from the injection of the harmonics. This is not the case with the Differentiation method, where there is a noticeable, significant distortion when compared to the simulated results obtained with an ideal AC grid voltage source. The other two methods present the same slight distortion.

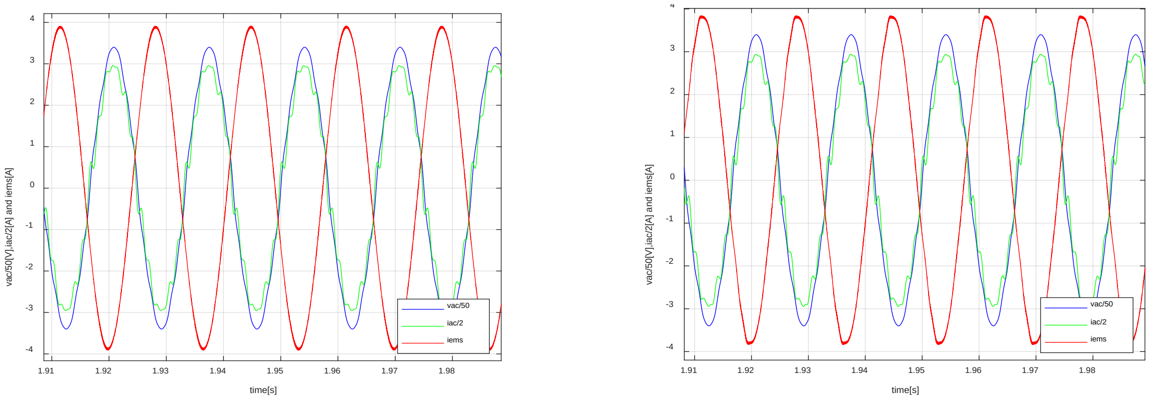

a) Quarter Cycle Delay method

b) Differentiation method

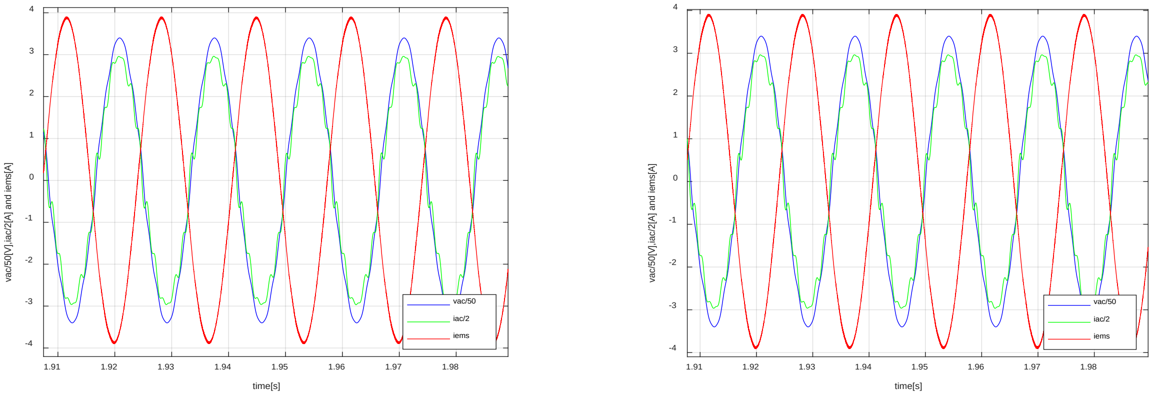

c) SOGI method

d) APF method

Figure 34. Source current, source voltage, and EMS current for a source with harmonics only, by using the DQ0 to AB0 transformation control method

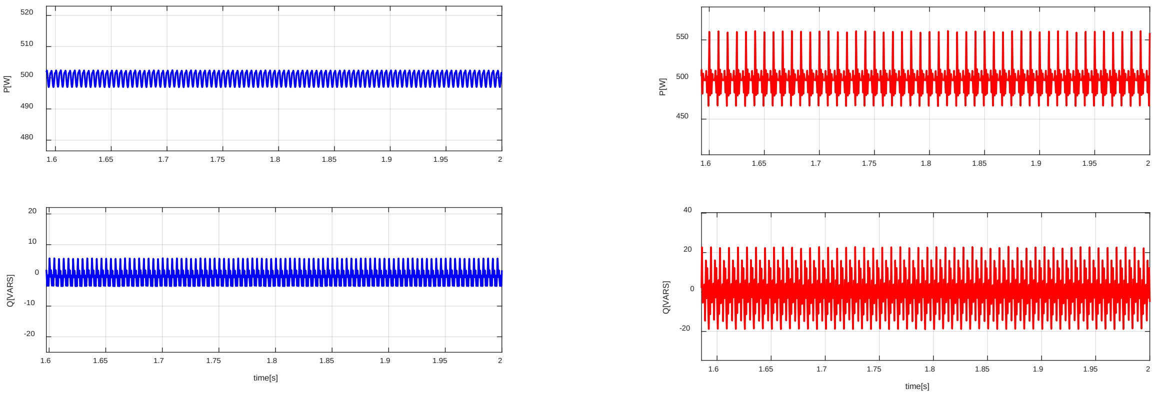

a) Quarter Cycle Delay method   b) Differentiation method

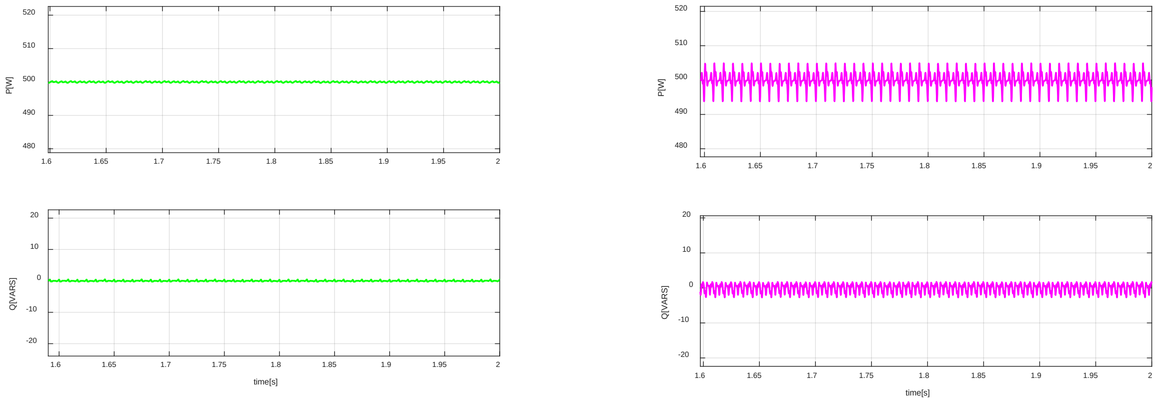

c) SOGI method   d) APF method

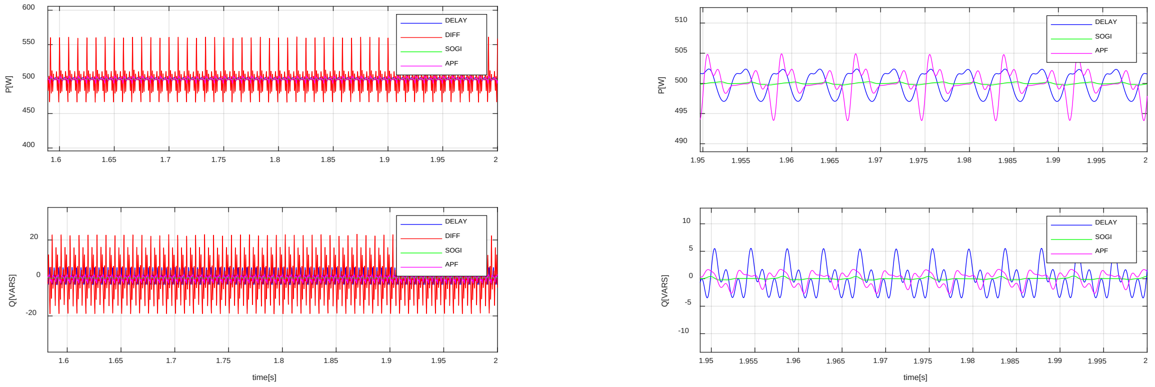

(e) All OGMs (zoom in)   (f) All OGMs (except differentiation)

Figure 35. P commanded to 500 W and Q commanded to 0 VARS for a source with harmonics only, by using the DQ0 to AB0 transformation control method

4. Source with Harmonics Only—Equation Control Method

In this case, the model has been examined to determine its performance when harmonics are added to the AC grid voltage and the equation control method is implemented. It is indisputable that the operation of all OGMs is exactly the same as that of the previous case, where the DQ0 to AB0 control method was used. As a consequence, Figure 36 shows that the difference of the angle between the voltage and current source is zero for all OGMs. It should be mentioned that there is only a minor difference with the Differentiation method (Figure 36b), which is that the current of the EMS is slightly distorted. Also, and as seen in Figure 37, the SOGI method achieves the best operation, while the Differentiation method has a significant amount of distortion. The other two OGMs demonstrate as before the same slight deformity.

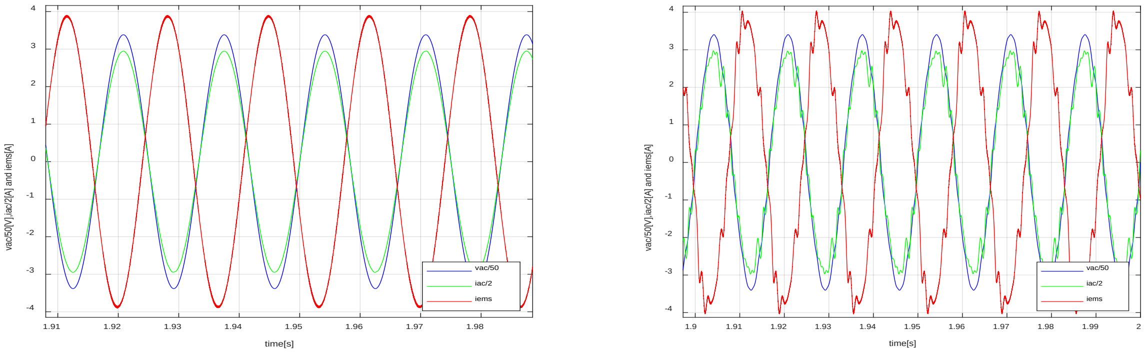

a) Quarter Cycle Delay method b) Differentiation method

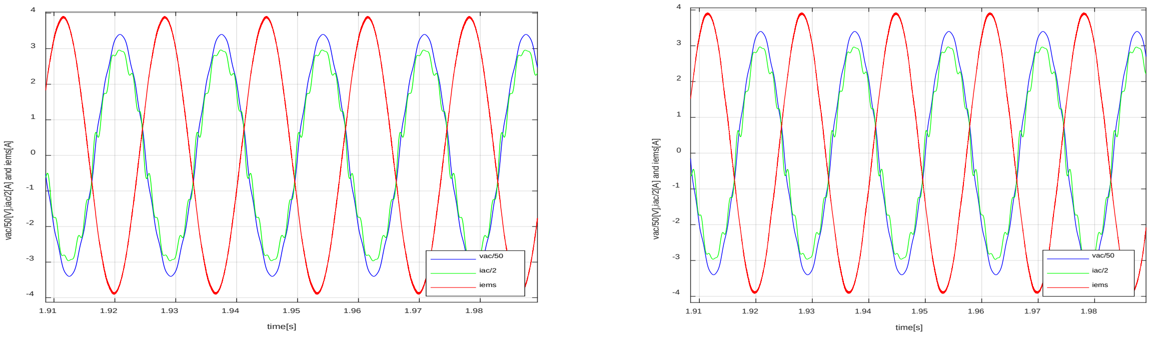

c) SOGI method d) APF method

Figure 36. Source current, source voltage, and EMS current for a source with harmonics only, by using the equation control method

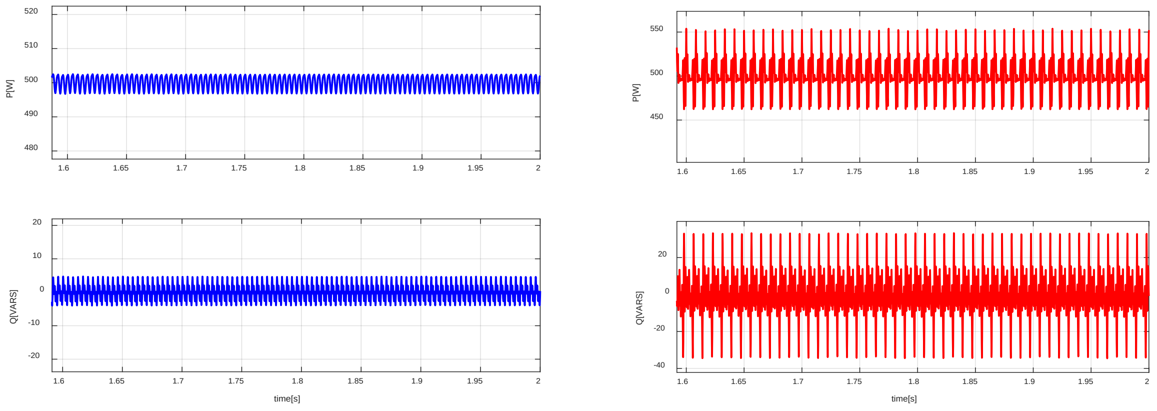

a) Quarter Cycle Delay method b) Differentiation method

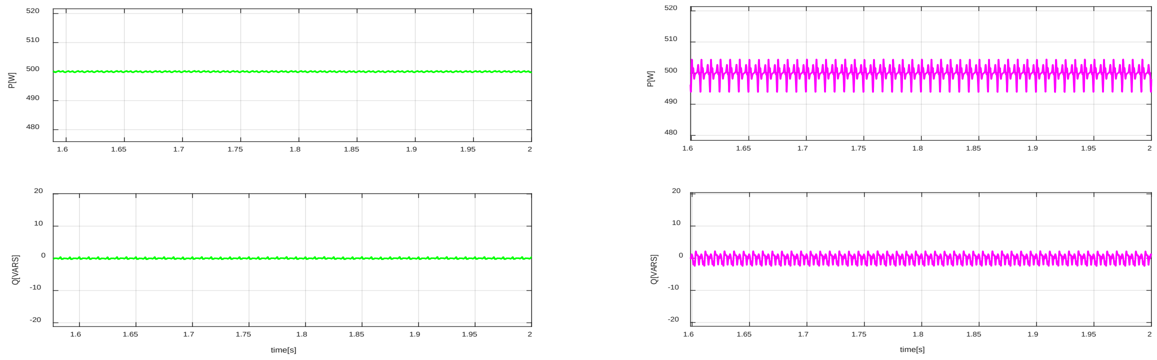

c) SOGI method d) APF method

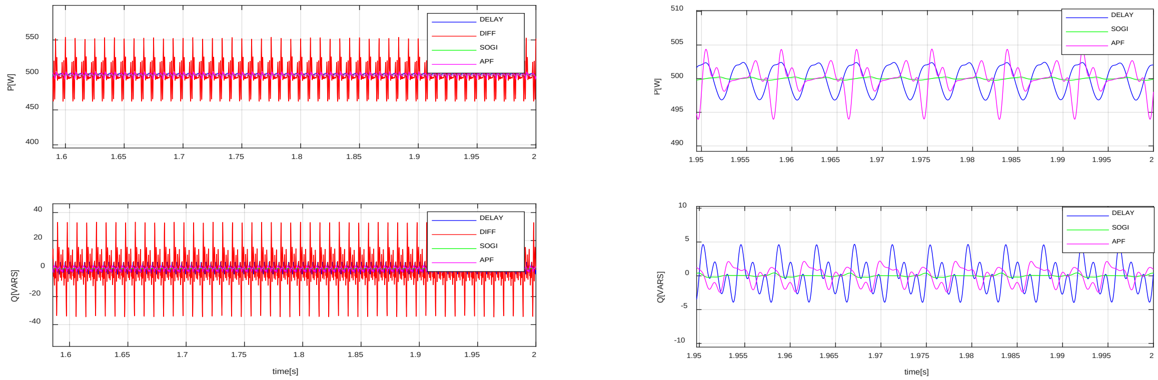

(e) All OGMs (zoom in) (f) All OGMs (except differentiation)

Figure 37. P commanded to 500 W and Q commanded to 0 VARS for a source with harmonics only, by using the equation control method

5. Source with Harmonics and Noise—DQ0 to AB0 Transformation Control Method

In this case, controller performance has been tested with the addition of both harmonics and high-frequency noise to the AC grid voltage source when the DQ0-to-AB0 transformation control method is applied. Figure 38 depicts how the current of the source is affected while the waveform of the voltage source is underneath. Therefore, the difference of the angle between the voltage and current source is zero for all OGMs. Lastly, it is perceptible in Figure 39 that the only method significantly influenced is the Differentiation method. As a result, the commanded active power and the reactive power differ from the measured active and reactive powers, respectively, and subsequently they cannot be controlled.

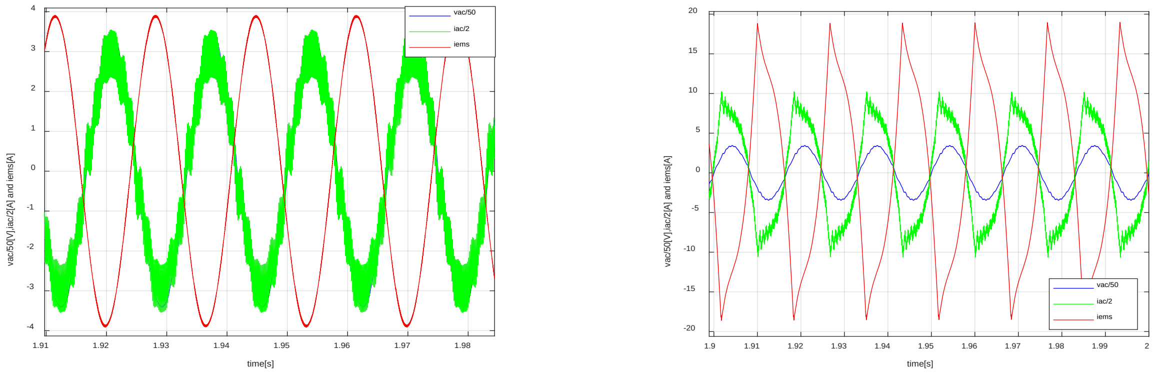

a) Quarter Cycle Delay method b) Differentiation method

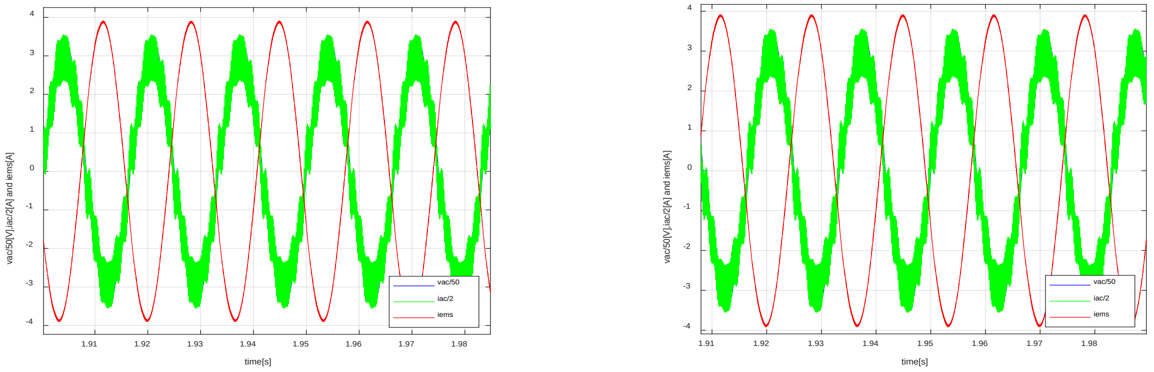

c) SOGI method d) APF method

Figure 38. Source current, source voltage, and EMS current for a source with harmonics and noise by using DQ0 to AB0 transformation control method

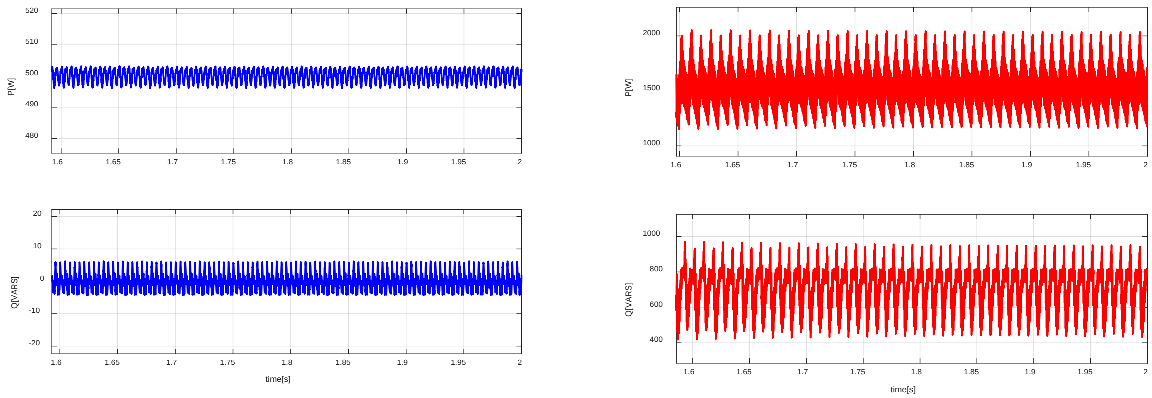

a) Quarter Cycle Delay method b) Differentiation method

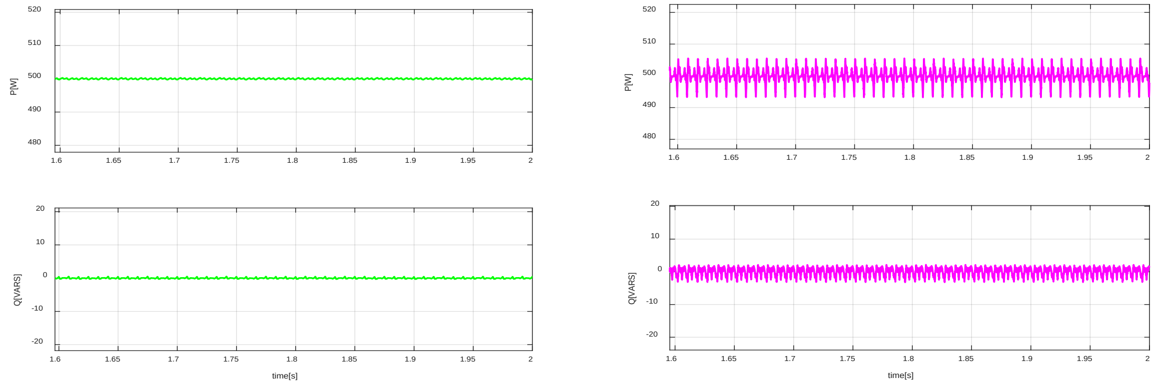

c) SOGI method d) APF method

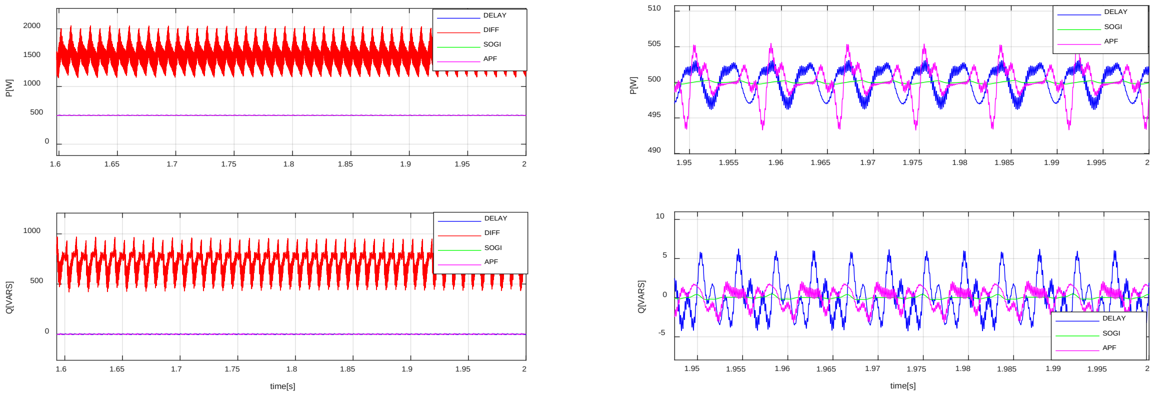

(e) All OGMs (zoom in) (f) All OGMs (except differentiation)

Figure 39. P commanded to 500 W and Q commanded to 0 VARS for a source with harmonics and noise by using DQ0 to AB0 transformation control method

6. Source with Harmonics and Noise—Equation Control Method

In this case, the same procedure as that of case (subsection) 5 has been followed, with the only difference being that the equation control method is implemented**.** ***As it occurred previously, the only method that is affected is the Differentiation method, as can be seen in Figure 41. As a result, this method should not be used for P-Q control.*** Concerning the other OGMs, it should be stated that they are equivalent if a DQ0 to AB0 transformation control method or equation control method is applied.

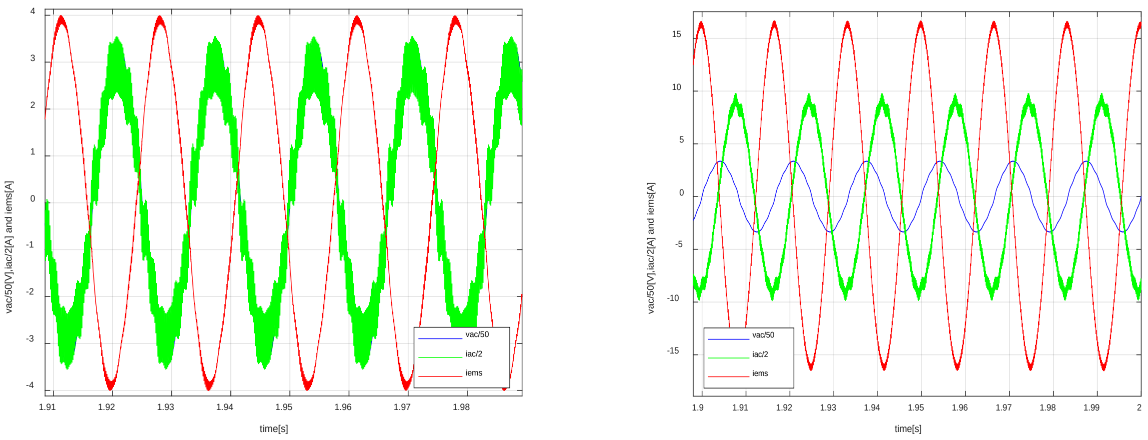

a) Quarter Cycle Delay method b) Differentiation method

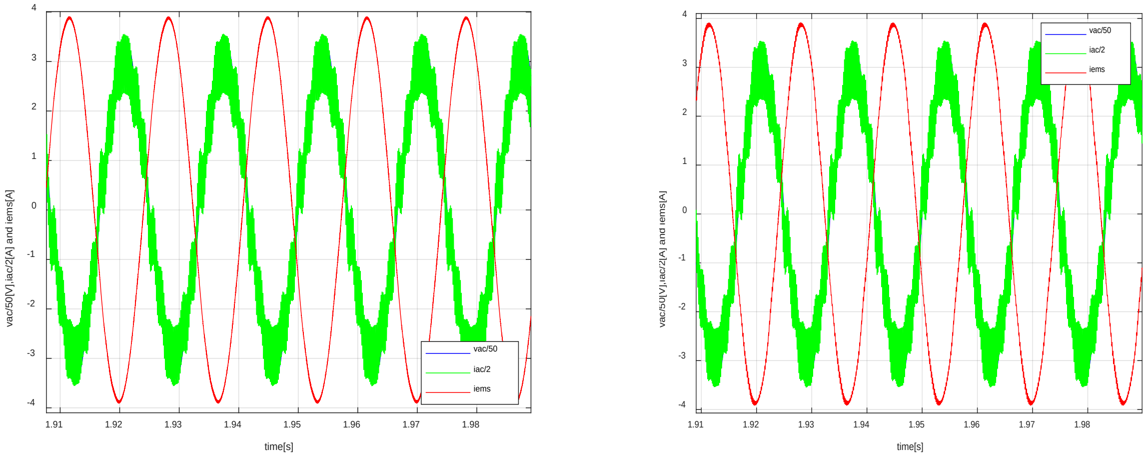

c) SOGI method d) APF method

Figure 40. Source current, source voltage, and EMS current for a source with harmonics and noise by using the equation control method

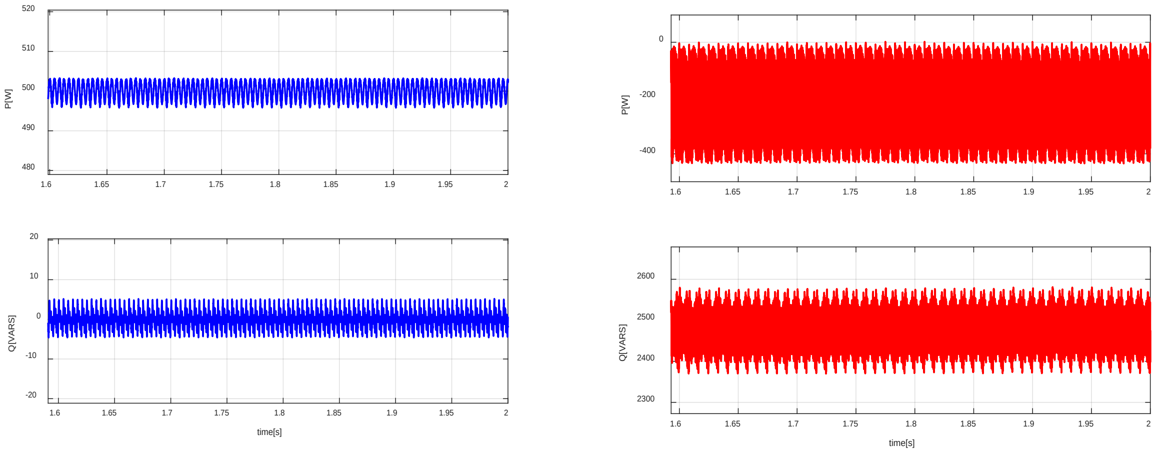

a) Quarter Cycle Delay method

b) Differentiation method

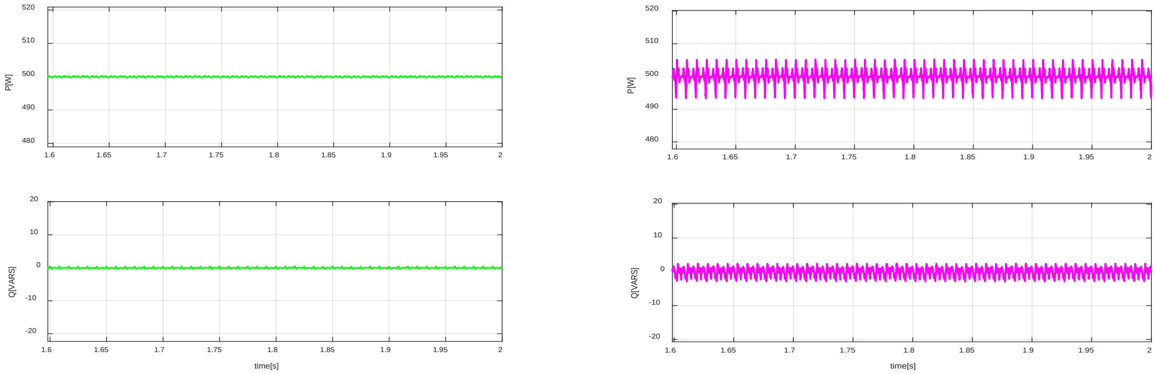

c) SOGI method

d) APF method

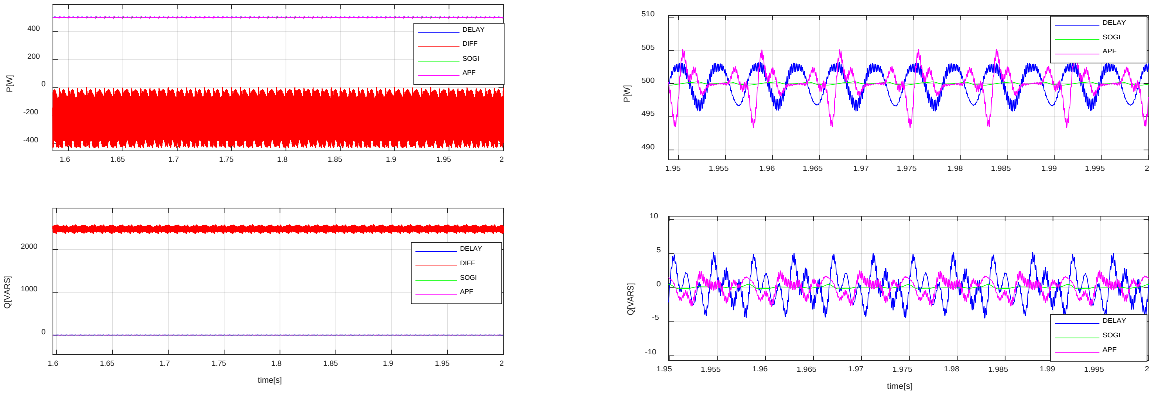

(e) All OGMs (zoom in)

(f) All OGMs (except differentiation)

Figure 41. P commanded to 500 W and Q commanded to 0 VARS for a source with harmonics and noise by using the equation control method

B. SIMULATED CASES FOR DIFFERENT VALUES OF K FOR THE SOGI METHOD

1. k=1/2

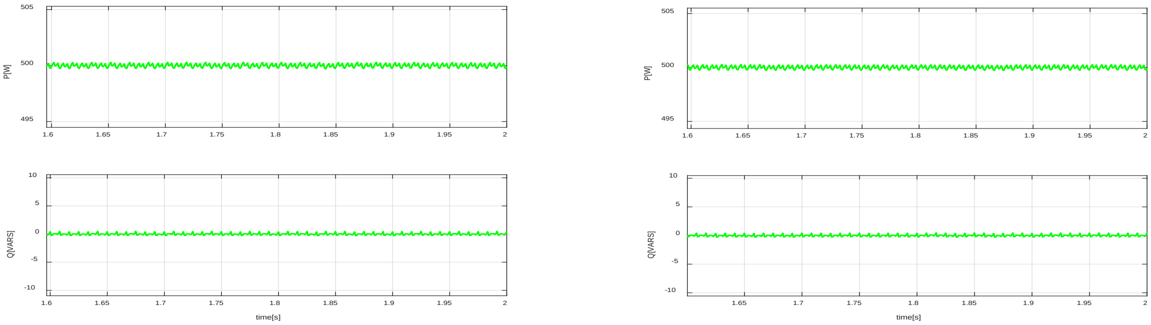

(a) DQ0 to AB0 transformation method (b) Equation method

2. k=3/2

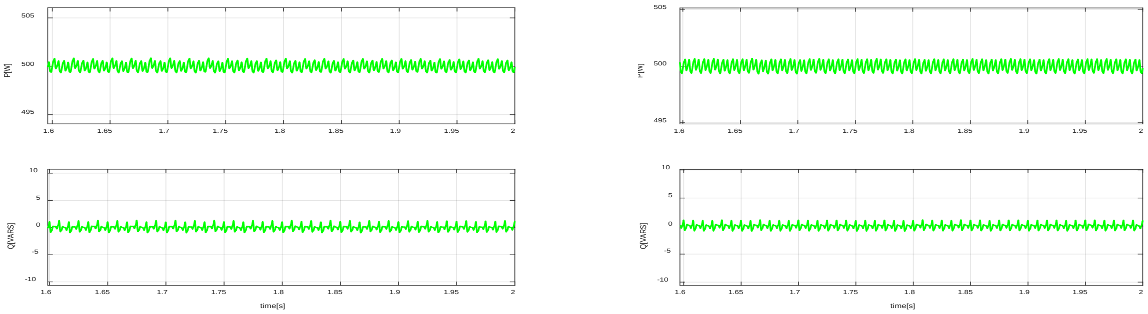

(a) DQ0 to AB0 transformation method (b) Equation method

3. k=2

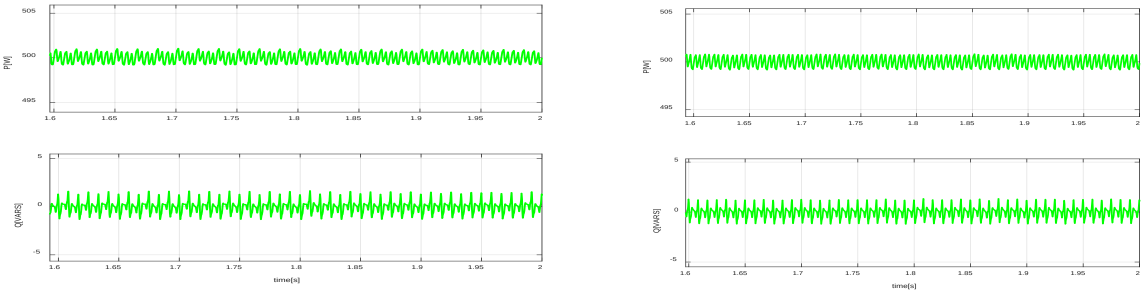

(a) DQ0 to AB0 transformation method (b) Equation method

Figure 42. Comparison of using different values of k for the SOGI for both the DQ0 to AB0 transformation and the equation control methods when a source with harmonics and noise exists

4. Comments

Figure 42 illustrates how the value of k affects the performance of the SOGI method regardless of the control method that has been used, where k=1/2 is the best choice for our control system.

C. SIMULATED CASES FOR DIFFERENT VALUES OF K_E, K_F FOR APF METHOD

1. $k_e = - k_f = 1$

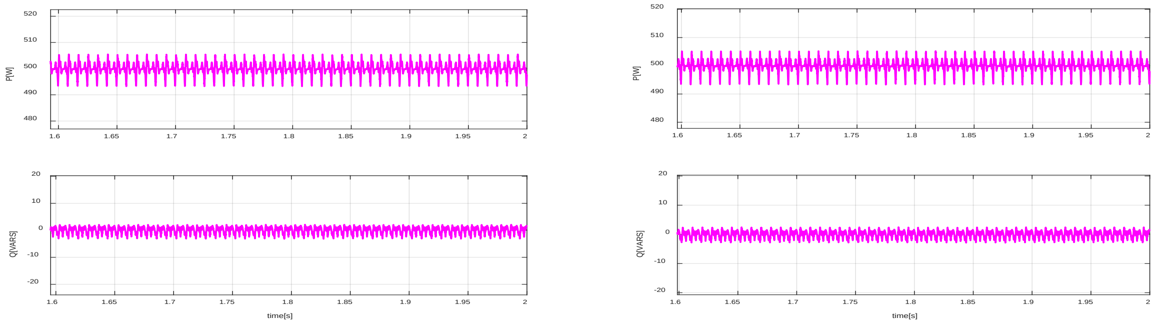

(a) DQ0 to AB0 transformation method

(b) Equation method

2. $k_e = - k_f = 1/10$

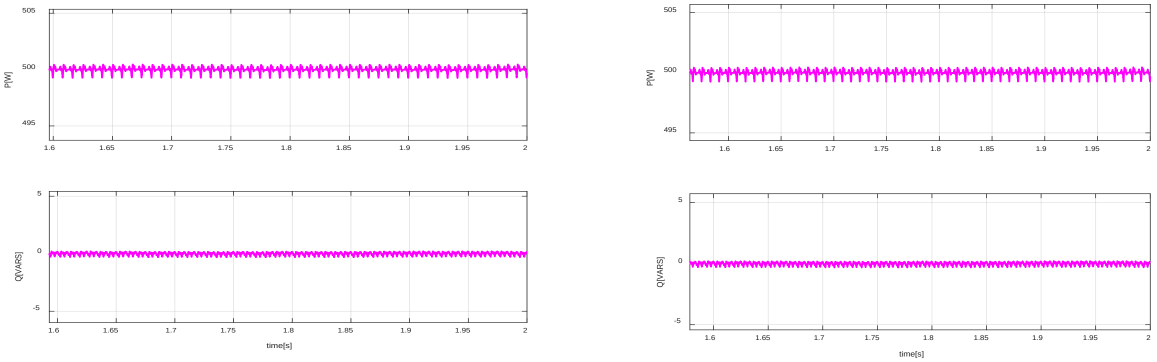

(a) DQ0 to AB0 transformation method

(b) Equation method

3. $k_e = - k_f = 1/25$

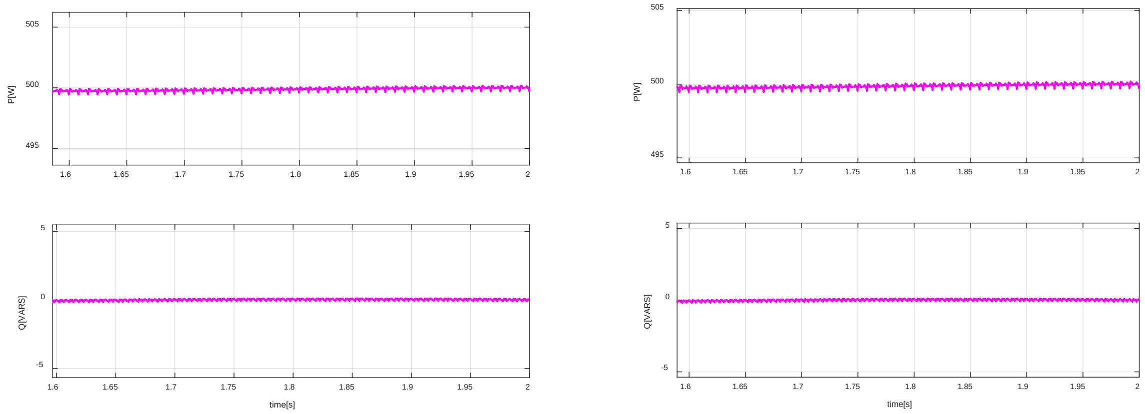

(a) DQ0 to AB0 transformation method (b) Equation method

Figure 43. Comparison of using different values of k_e,k_f for the APF for both the DQ0 to AB0 transformation and the equation control methods when a source with harmonics and noise exists

4. Comments

Figure 43 illustrates how the value of k_e, k_f affects the performance of the APF method regardless of the control method that has been used. As a consequence, it can be mentioned that the best case simulated is $k_e = -k_f = 1/25$.

In order to validate our simulated results, experimental measurements are analyzed in Chapter VI.

VI. EXPERIMENTAL VALIDATION

A. HARDWARE

A laboratory prototype of the EMS is shown in Figure 44. As shown, three Printed Circuit Boards (PCB) exist:

- The Power Electronics PCB includes a DC power supply, voltage and current sensors, cooling system, and three integrated power modules. Two of those modules are used to create the H-bridge of the EMS and the third is for the buck and boost converter [7].
- The FPGA control board is connected to a Personal Computer (PC) through a Join Test Action Group (JTAG) cable [5]. The FPGA is part of a Xilinx development board [23], and is programmed using MATLAB/Simulink and the Xilinx System Generator software [24]. The purpose of this software is to convert the Simulink model into Very High Speed Integrated Circuit Hardware Description Language (VHDL) code. The control methods we examined previously were programmed into the FPGA board to study the performance of the control system, which is shown in Figure 25.
- The Interface board consists of a number of analog-to-digital converters and many other connections in order to pass signals between the FPGA and the Power Electronics PCB.

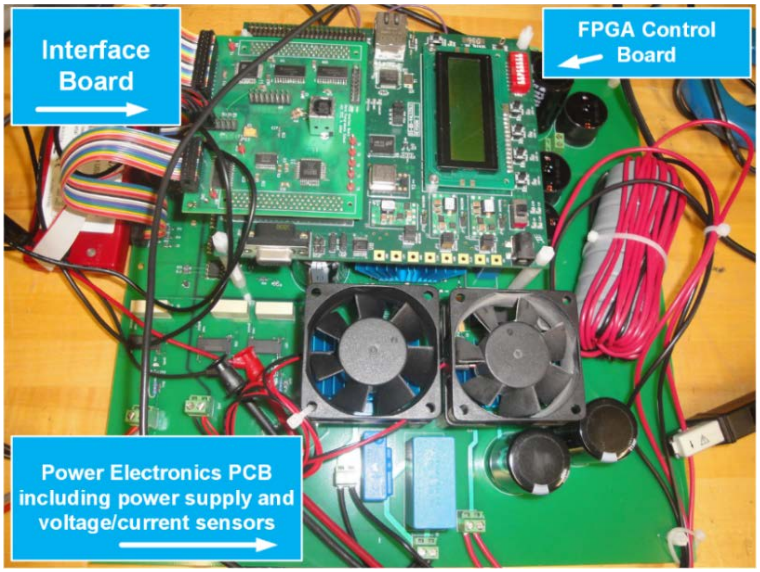

Figure 44. EMS hardware as implemented in the laboratory. Source: [7].

The block diagram of the EMS hardware can be observed in Figure 45, which shows the main elements of each PCB and their connections. The loads in the experimental set-up are the same loads that have been used in the Simulink model, as shown in Figure 29.

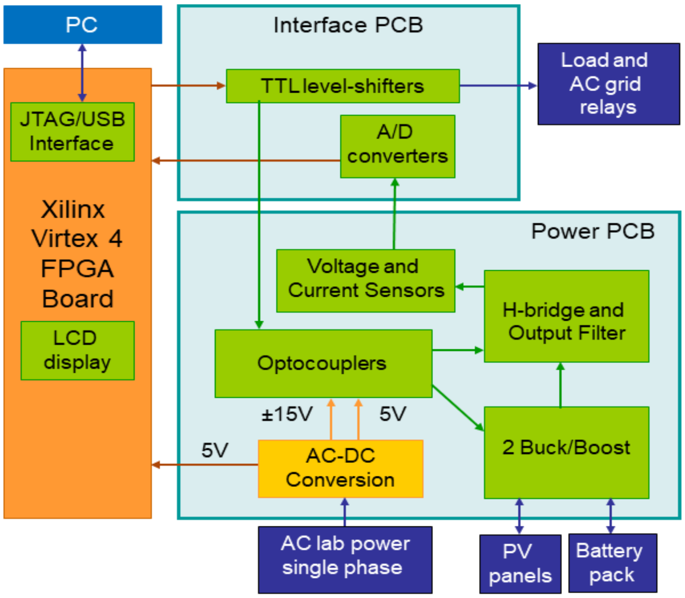

Figure 45. Block diagram of EMS hardware. Source: [7].

B. EXPERIMENTAL MEASUREMENTS

The circuit built in the laboratory is the same as the simulated circuit represented in Figure 28. In that way, it is possible to perform a validation between the simulated and experimental measurements. All the following plots were obtained using the Orthogonal Generation method SOGI with the DQ0 to AB0 transformation control method, as described in Chapter IV “Modeling Simulation,” when $k = ½$. Furthermore, all the plots were accomplished using the Xilinx integrated logic analyzer to export the data from the FPGA.

The following different cases have been tested in the laboratory for validation of our simulated results:

- Case 1: Commanded Active Power P = 150 W and Commanded Reactive Power Q = 0 VARS
- Case 2: Commanded Active Power P = 500 W and Commanded Reactive Power Q = 0 VARS
- Case 3: Step of the Power from case 1 to case 2
- Case 4: Step of the Power from case 2 to case 1

1. Case 1: Commanded Active Power P = 150 W and Commanded Reactive Power Q = 0 VARS

a. Experimental Measurements

In this case, we command the active power to be 150 W and the reactive power to be 0 VARS. Figure 46 shows the orthogonal currents i_α and i_β in the stationary reference frame. By presenting this plot, we can verify that the currents created in the laboratory from the SOGI method are orthogonal.

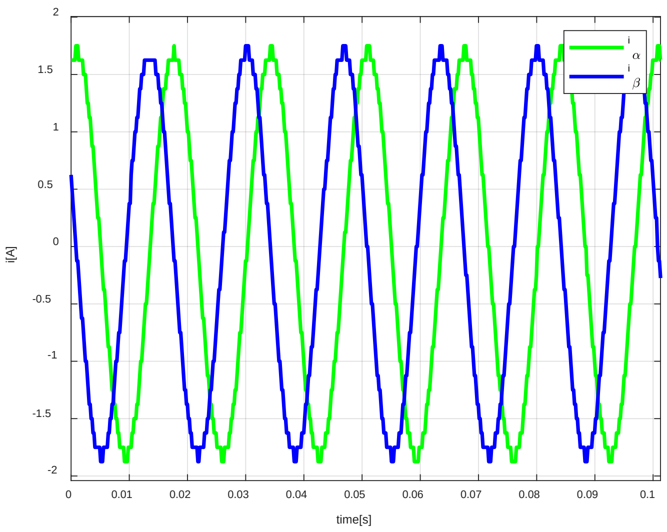

Figure 46. Orthogonal currents created by the SOGI method in the laboratory for the case of P = 150 W and Q = 0 VARS

In Figure 47, the active and reactive powers are shown when their references were set at 150 W and 0 VARs, respectively. From that plot, we can observe that ***the commanded active and reactive powers and the measured active and reactive powers are the same, respectively.***

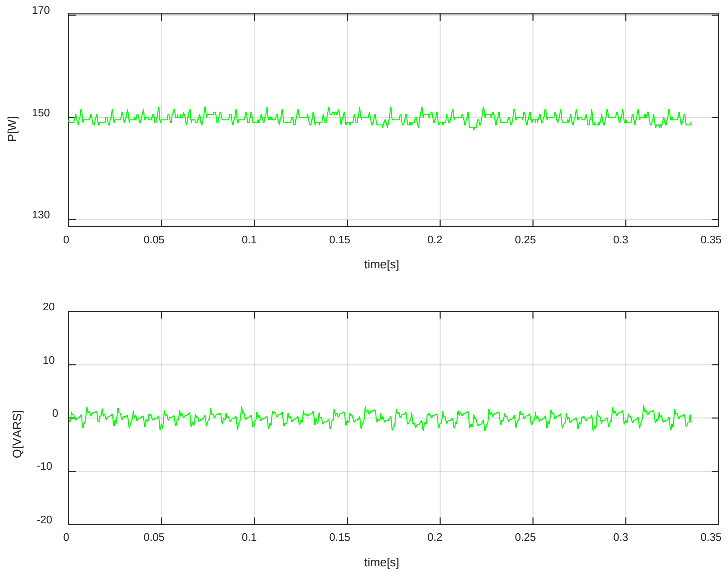

Figure 47. P commanded to 150 W and Q commanded to 0 VARS, created by the SOGI method in the laboratory

Additionally, Figure 48 shows that the source current is in phase with the source voltage and therefore confirms that ***the reactive power at the source is zero, obtaining unity power factor.*** The EMS current is also shown in Figure 48. The data obtained from Figure 48 was filtered to focus on the lower frequency behavior. Some low-frequency harmonics are visible in these experimental measurements due to distortion present in the source voltage, as well as some possible resonance in the passive load set-up in the laboratory.

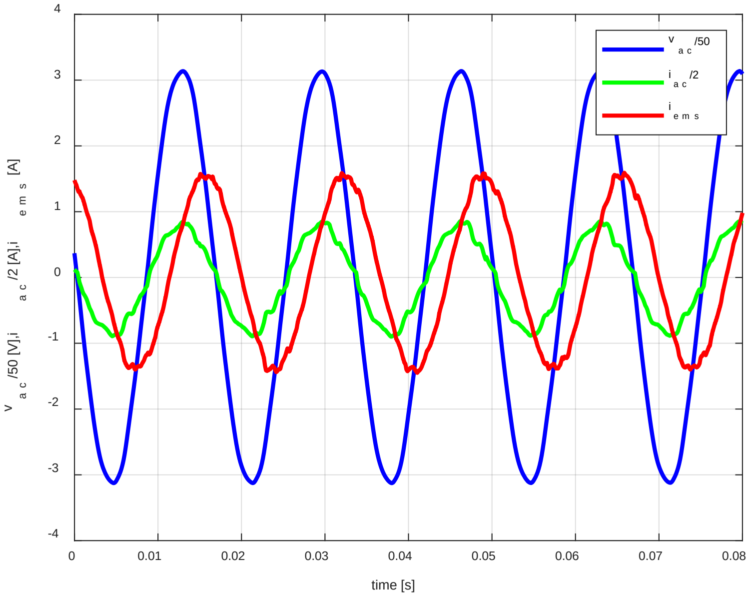

Figure 48. Source current in phase with the source voltage and EMS current for the case of P = 150 W and Q = 0 VARS, using the SOGI method in the laboratory

Furthermore, in Figure 48 it can be observed how harmonics in the voltage source distort the waveforms of our experimental results. The frequency spectrum of the voltage source and its harmonics is seen in Figure 49. It is obvious that the fifth (300 Hz), the seventh (420 Hz), the 11th (660 Hz), and the 13th (780 Hz) harmonics are those that affect the experimental results the most.

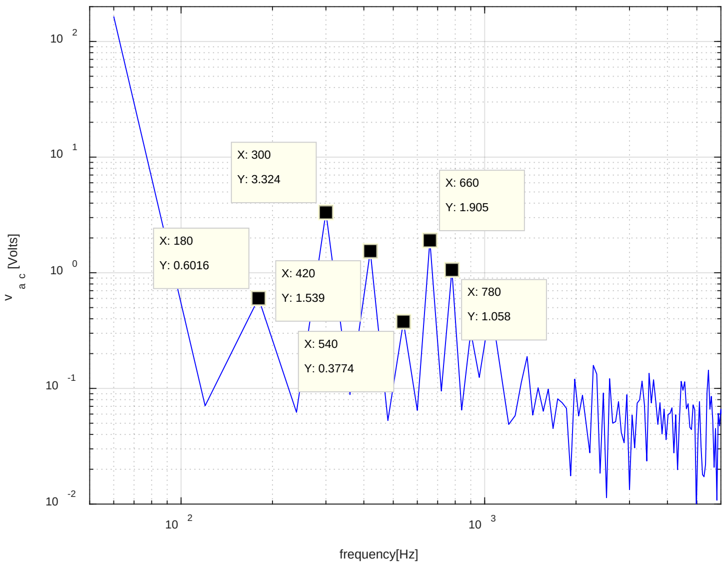

Figure 49. Voltage harmonics for the case of P = 150 W and Q = 0 VARS, using the SOGI method in the laboratory

b. Experimental Validation

In this section, the simulated and the experimental measurements are compared in order to validate the Simulink model. In Figure 50, we see that the commanded active power P=150 W and the commanded reactive power Q = 0 VARS are achieved both in the laboratory and in the Simulink model.

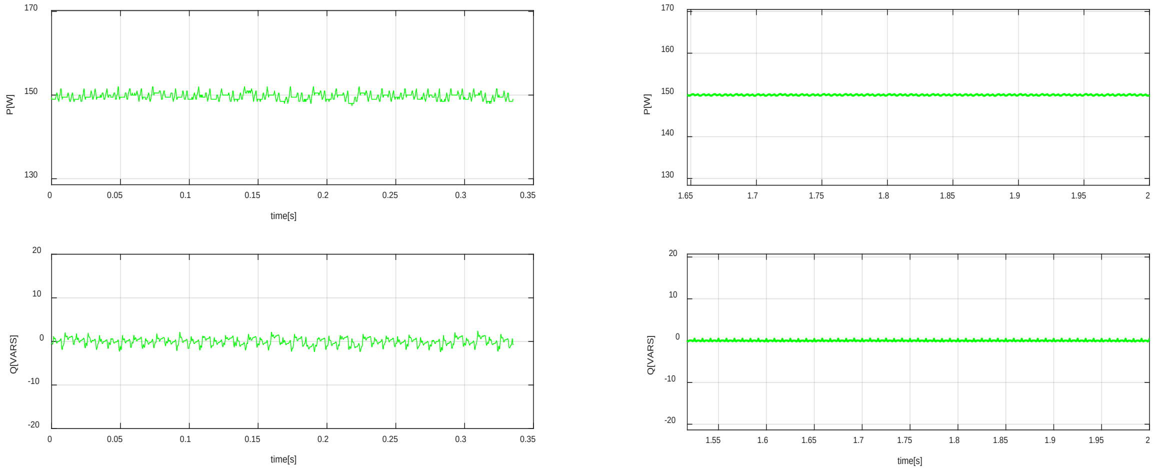

(a) Laboratory (b) Simulink

Figure 50. Experimental validation of the commanded active power P = 150 W and the commanded reactive power Q = 0 VARS

Figure 51 confirms that both in Simulink and in the lab the voltage source is in phase with the current source, thereby obtaining the desired unity power factor. It can also be observed that the values between the Simulink and the laboratory are almost the same.

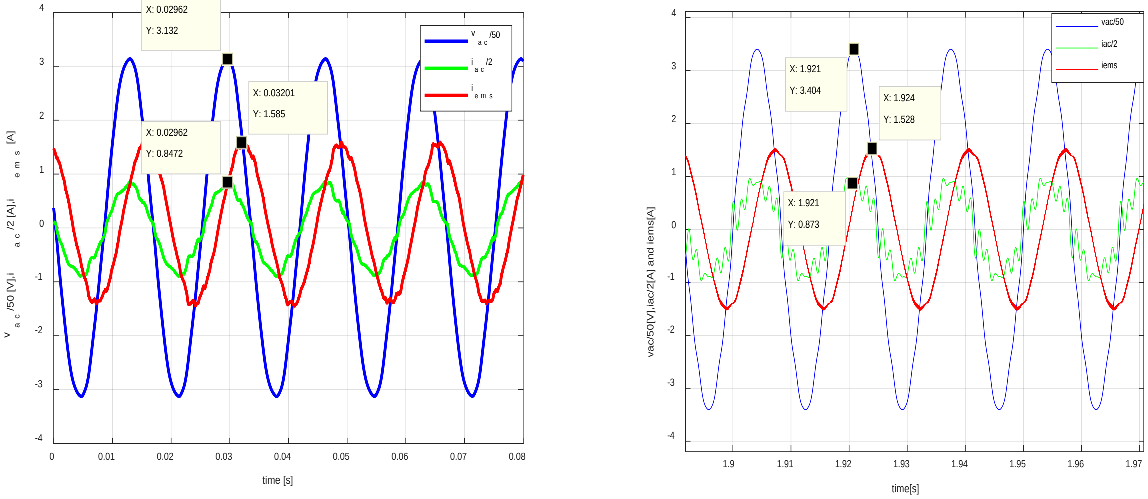

(a) Laboratory (b) Simulink

Figure 51. Experimental validation of the source current in phase with the source voltage for the case of P = 150 W and Q = 0 VARS

As a consequence, in Figure 50 and Figure 51 we see that our goal has been accomplished using the SOGI method because it was proven that ***the required active and reactive power specifications were obtained.***

2. Case 2: Commanded Active Power P = 500 W and Commanded Reactive Power Q = 0 VARS

a. Experimental Measurements

In this case, we command the active power to be 500 W and the reactive power to be 0 VARS. Figure 52 shows the orthogonal currents i_α and i_β in the stationary reference frame. By presenting this plot, we can verify that the currents created in the laboratory from the SOGI method are orthogonal.

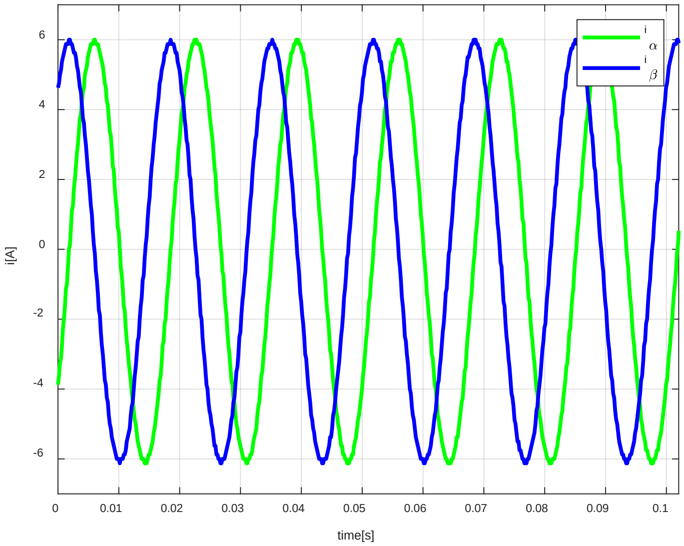

Figure 52. Orthogonal currents created by the SOGI method in the laboratory for the case of P = 500 W and Q = 0 VARS

Moreover, in Figure 53, active and reactive powers are shown when their references were set at 500 W and 0 VARs, respectively. From that plot, we can state the same conclusion as in case 1 that ***the commanded active and reactive powers and the measured active and reactive powers are the same, respectively.***

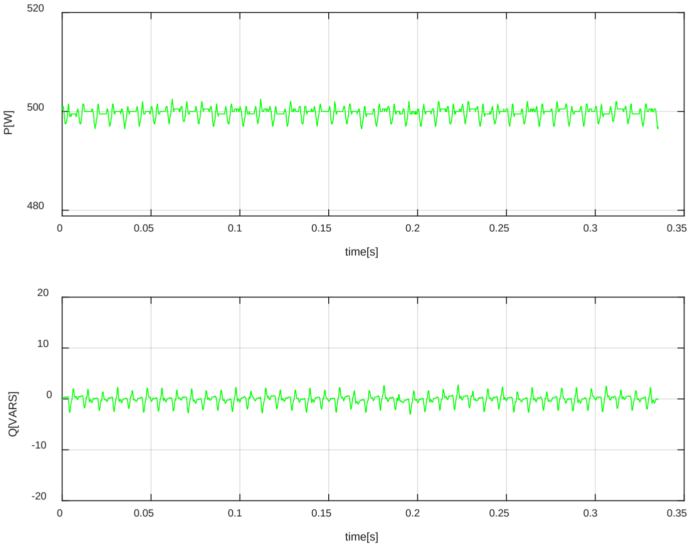

Figure 53. P commanded to 500 W and Q commanded to 0 created by the SOGI method in the laboratory

Figure 54 shows that the source current is in phase with the source voltage and therefore confirms that ***the reactive power at the source is zero, obtaining the desired unity power factor.*** The EMS current is also shown in Figure 54. As already mentioned for case 1, the data obtained for Figure 54 was filtered to focus on the lower frequency behavior.

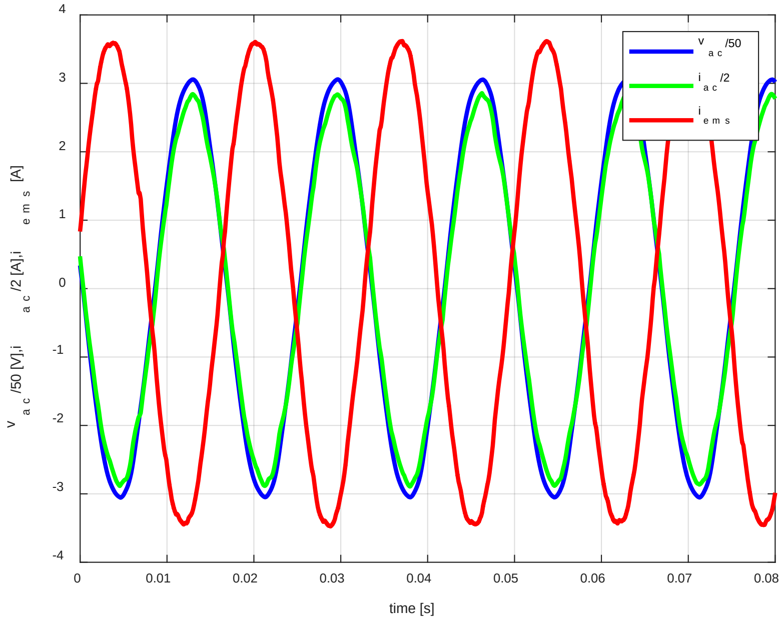

Figure 54. Source current in phase with the source voltage and EMS current for the case of P = 500 W and Q = 0 VARS, using SOGI method in the laboratory

Moreover, in Figure 54 it can be observed how harmonics in the voltage source distort the waveforms of our experimental results, while Figure 55 illustrates the frequency spectrum of the voltage source and its harmonics. It is clear that the fifth (300 Hz), the seventh (420 Hz), the 11th (660 Hz), and the 13th (780 Hz) harmonics are those that affect our experimental results the most.

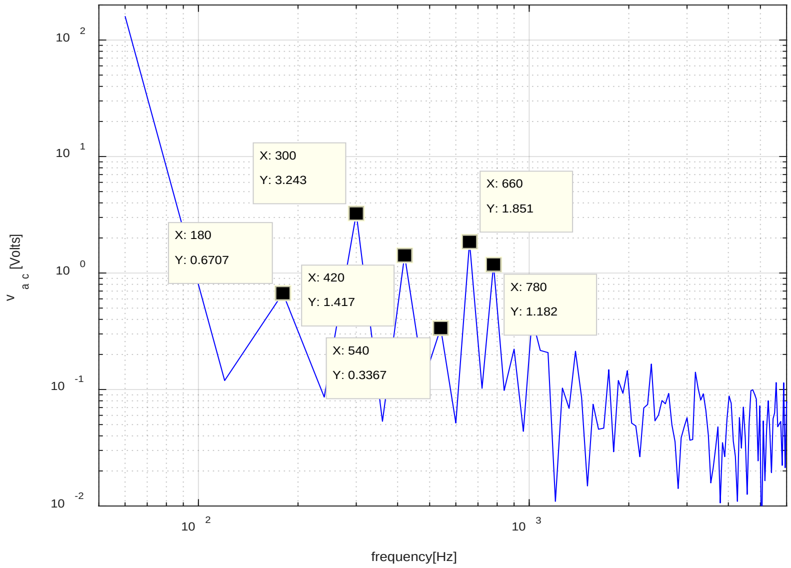

Figure 55. Voltage harmonics for the case of P = 500 W and Q = 0 VARS, using the SOGI method in the laboratory

b. *Experimental Validation*

In this section, the Simulink and the experimental measurements are compared in order to validate our results. Figure 56 confirms that the commanded active power P = 500 W and the commanded reactive power Q = 0 VARS are implemented in the lab and in Simulink.

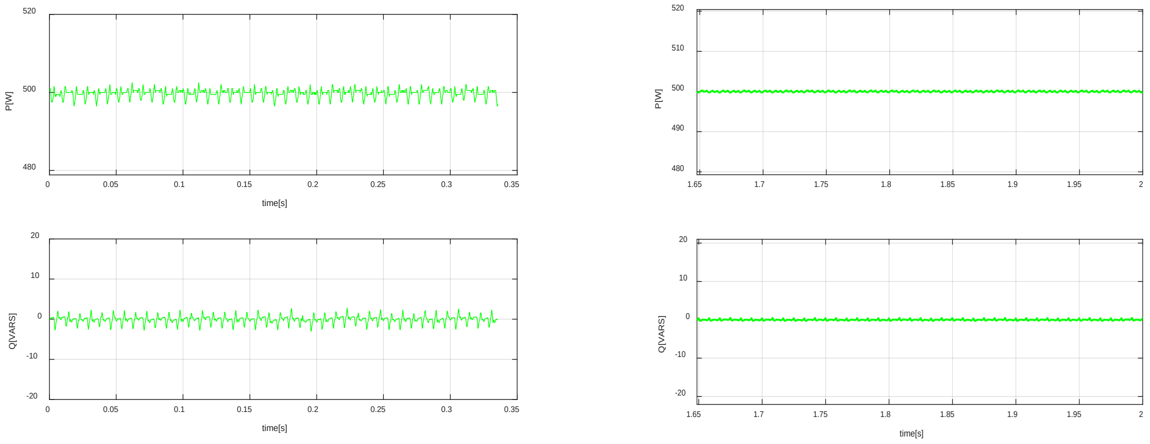

(a) Laboratory

(b) Simulink

Figure 56. Experimental validation of the commanded active power P = 500 W and the commanded reactive power Q = 0 VARS

Figure 57 confirms that both in Simulink and in the lab the reactive power at the source is zero, obtaining unity power factor. It can be observed that the values between Simulink and the laboratory are almost the same.

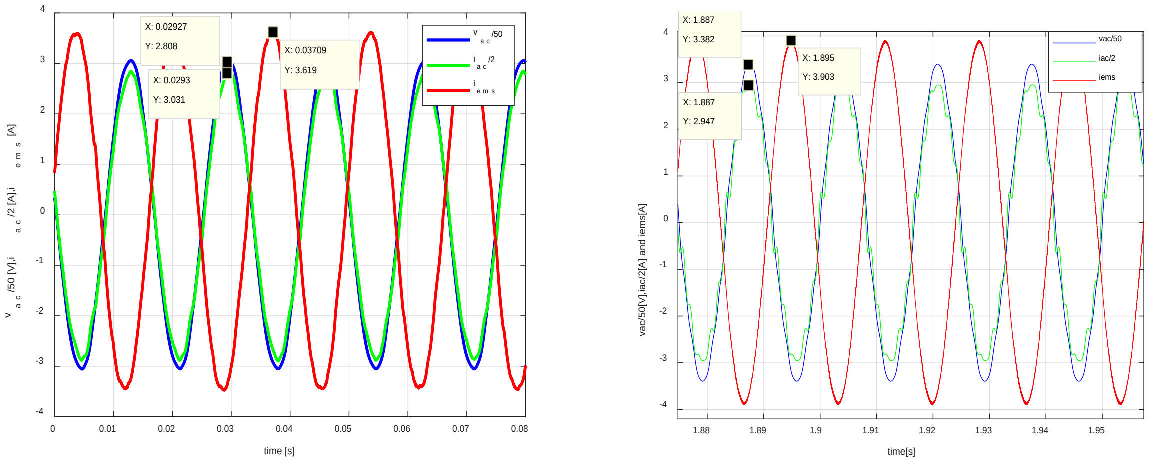

(a) Laboratory (b) Simulink

Figure 57. Experimental validation of the source current in phase with the source voltage for the case of P = 500 W and Q = 0 VARS

Therefore, Figure 56 and Figure 57 show that, our goal has been accomplished using the SOGI method, because it was proven that ***the implementation of active and reactive power control flow has been obtained, which is the goal of this thesis.***

3. Case 3: Commanded Step of Active Power from P = 150 W to P = 500 W and Commanded Reactive Power Q = 0 VARS

a. Experimental Measurements

In this case, initially we set the active power to be 150 W and then to step up to 500 W. During the whole procedure the reactive power is 0 VARS. Figure 58 shows the orthogonal currents i_α and i_β in the stationary reference frame. By presenting this plot, we can verify that the currents created from the SOGI method are orthogonal during the experimental procedure.

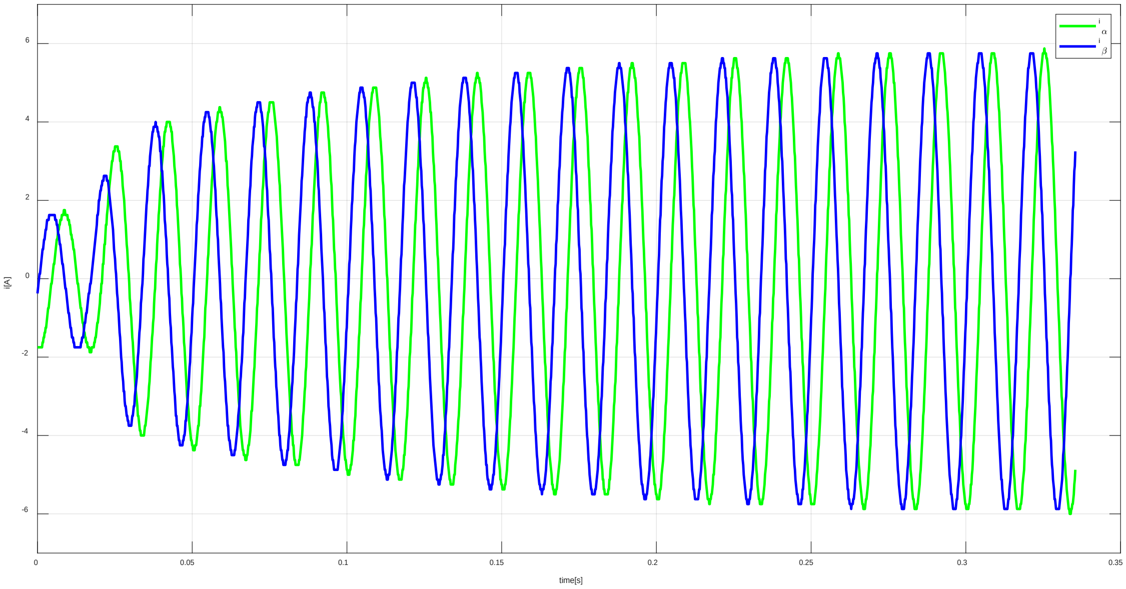

Figure 58. Orthogonal currents created by the SOGI method in the laboratory for the case of step up from P = 150 W to P = 500 W while Q = 0 VARS

Figure 59 confirms that the step from the active power P = 150 to 500 W is accomplished, and also that the commanded reactive power Q = 0 VARS is zero.

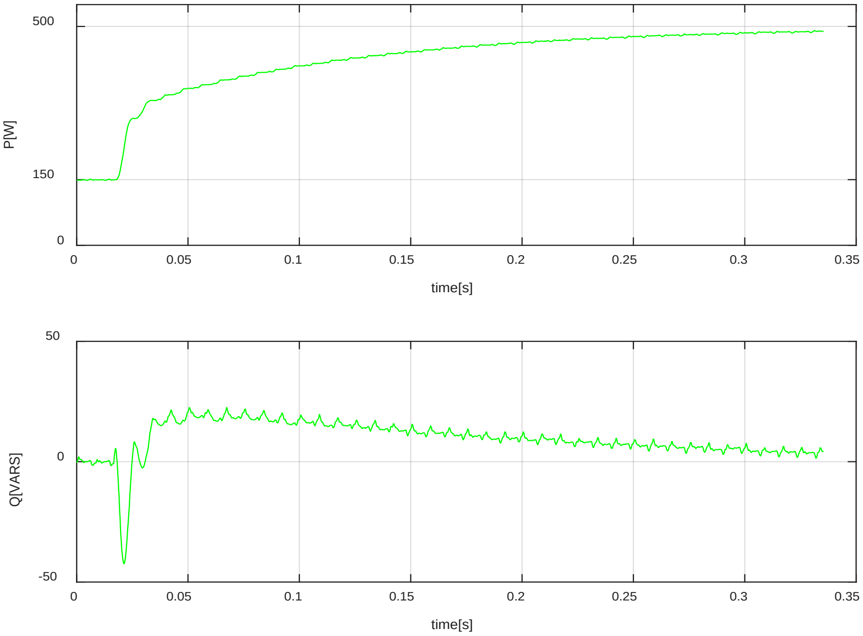

Figure 59. P commanded from 150 W to 500 W and Q commanded to 0 VARS, created by the SOGI method in the laboratory

b. *Experimental Validation*

In this section, the Simulink and the experimental measurements are compared in order to validate our results. We set in our model a step to take place at 1.5 seconds from P = 150 W to P = 500 W while Q stays constant at 0 VARS. Figure 60 confirms this procedure.

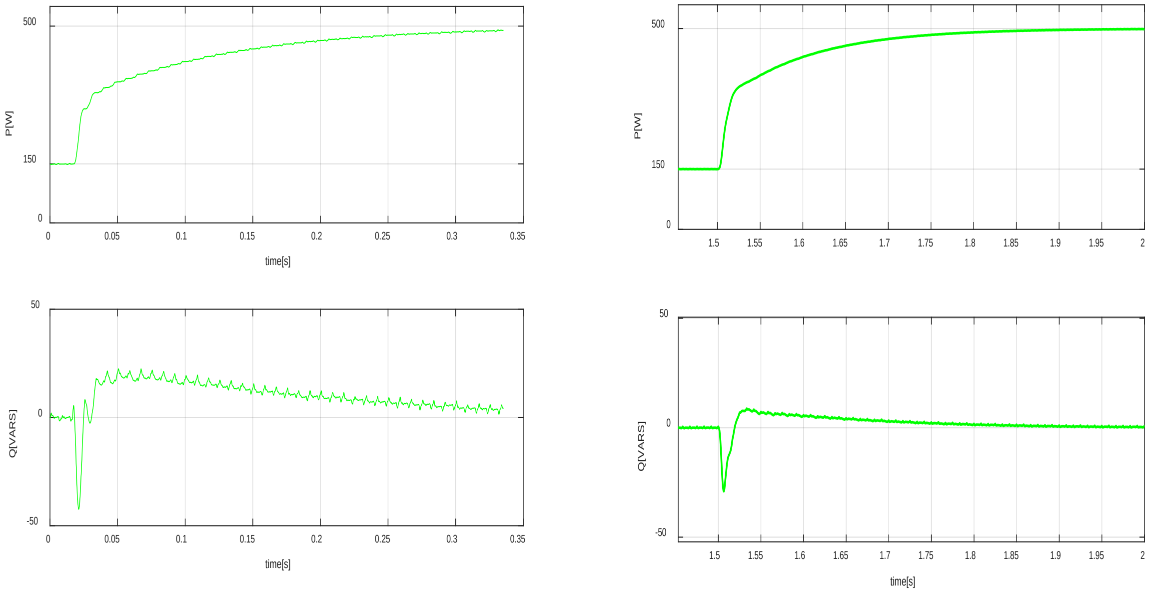

(a) Laboratory (b) Simulink

Figure 60. Experimental validation of the commanded P from 150 W to 500 W and the commanded Q to 0 VARS

Therefore, by comparing the results from our model and the experimental measurements, we can validate that, ***in both cases, the implementation of control of the active and reactive power flow is accomplished.***

4. Case 4: Commanded Step of Active Power from P = 500 W to P = 150 W and Commanded Reactive Power Q = 0 VARS

a. *Experimental Measurements*

In this case, initially we set the active power to be 500 W and then to step down to 150 W. During the whole procedure the reactive power is 0 VARS. Figure 61 shows the orthogonal currents i_α and i_β in the stationary reference frame. By presenting this plot, we can verify that the currents created from the SOGI method are orthogonal during the experimental procedure.

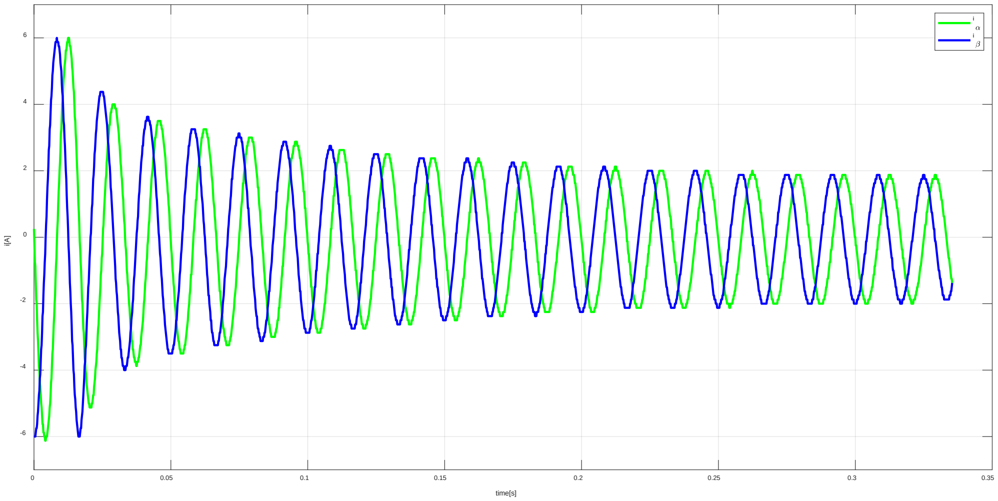

Figure 61. Orthogonal currents created by the SOGI method in the laboratory for the case of step down from P = 500 W to P = 150 W and Q = 0 VARS

Figure 62 confirms that the step from the active power P = 500 to 150 W is accomplished, and also that the commanded reactive power Q = 0 VARS is zero.

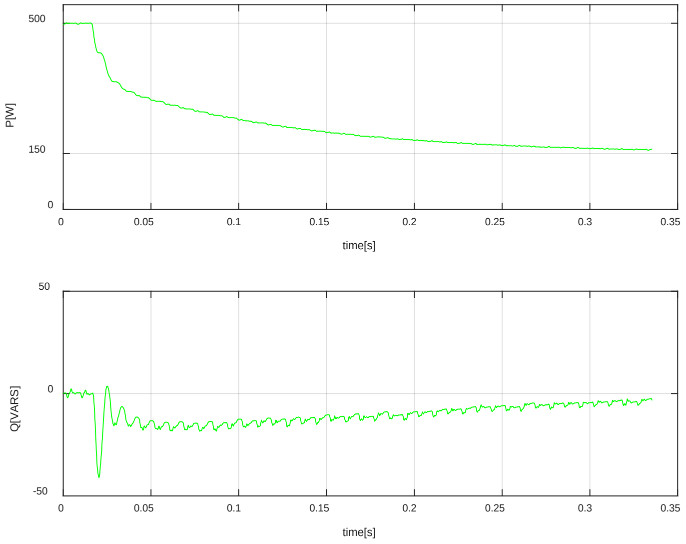

Figure 62. Experimental validation of the commanded P from 500 W to 150 W and the commanded Q to 0 VARS

b. Experimental Validation

In this section, the Simulink and the experimental measurements are compared in order to validate our results. We set in our model a step to take place at 1.5 seconds from P = 500 W to P = 150 W while Q stays constant at 0 VARS. Figure 63 confirms this procedure.

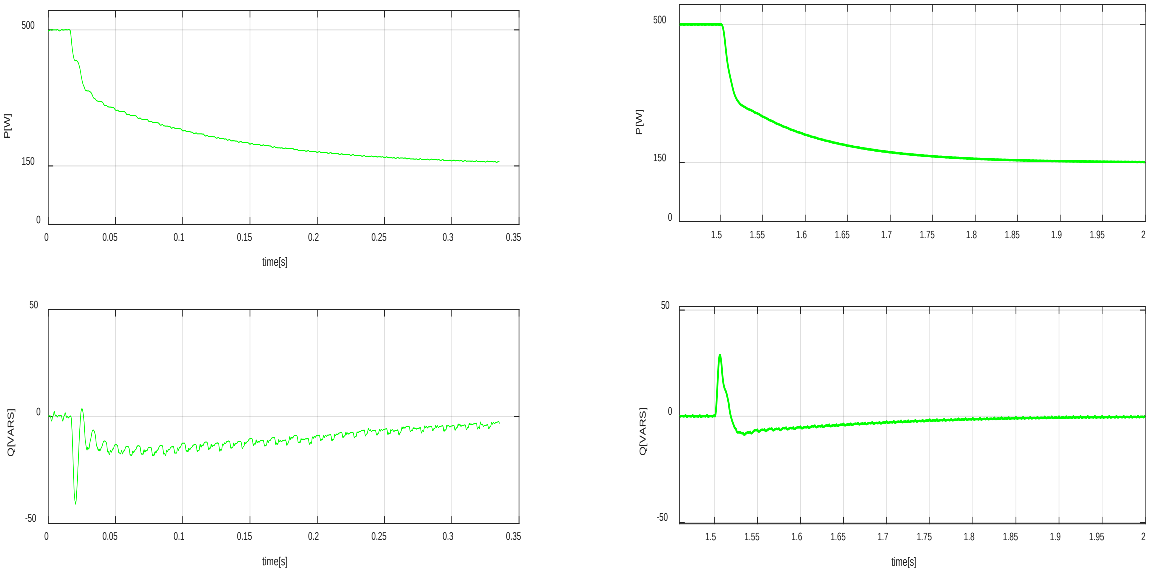

(a) Laboratory (b) Simulink

Figure 63. P commanded from 500 W to 150 W and Q commanded to 0 VARS, created by the SOGI method in Simulink

It can be concluded that in all the mentioned cases, the experimental measurements validated the simulated results for the SOGI method. Therefore, by comparing the results from our model and the experimental measurements, it can be verified that, ***in both cases, the implementation of the active and reactive power flow control is obtained.***

THIS PAGE INTENTIONALLY LEFT BLANK

VII. CONCLUSIONS AND FUTURE WORK

A. CONCLUSIONS

In this thesis we demonstrate the performance of a novel mixed-frame controller for active and reactive power flow control in a single phase grid-connected EMS. Four different methods for generating the fictitious orthogonal components have been implemented to evaluate their effect on the controller performance. Taking into consideration the simulated and experimental results, we make the following conclusions:

- In all cases, there is ***no difference*** in the performance of the OGMs ***between*** the two control methods, ***the DQ0-to-AB0 transformation control method and the equation control method***. A significant difference was observed only for the case in which the AC grid is modeled as a voltage source with harmonics and noise when the differentiation method is implemented. Nonetheless, it does not affect our conclusion, because this is the only case in which the active power and reactive power cannot be controlled.
- ***For an ideal source,*** the active and reactive power flow can be ***controlled for all OGMs***. But, in reality, no ideal source exists. Thus, we examined how this is affected in two more cases: i) a source with only harmonics, and ii) a source with harmonics and high-frequency noise.
- By implementing a ***source with harmonics only***, the SOGI method is not affected at all and behaves as in the case with the ideal source. On the other hand, the Differentiation method is influenced the most. The Quarter Cycle Delay method and the APF method, when k_e=1 and k_f=-1, present a slight difference. It should be mentioned, however, that the performance of the APF can be improved by setting other values of the gains k_f =-k_e, as previously been noted.
- In the case of a ***source with harmonics and high-frequency noise***, only the Differentiation method is affected and characteristically is the only case in which the active power and reactive power cannot be controlled. The

performance of the control system with all the other OGMs stays unchanged. Therefore, the SOGI method illustrates the best performance with no distortion and a unity power factor in the grid. The Quarter Cycle Delay method and the APF method present a slight distortion, which does not affect the control of active and reactive power control flow.

- When using either the SOGI or the APF method, it is crucial to determine the value of k and k_e, respectively. Therefore, those gains should be tuned to achieve the best performance with those methods.

In summary, the goal of this thesis has been obtained by testing a significant number of different cases. Taking into account that the experimental measurements validate the simulated results, it can be concluded that the Quarter Delay, the SOGI, and the APF methods, which can be implemented either by the DQ0-to-ABO transformation or the equation control methods, have accomplished the desired P and Q power flow control. This means that the microgrid can compensate for the reactive power drawn by the loads, and simultaneously manage the active power. This contributes to the reduction of the cost of the electricity and to the delivery of the maximum available power to the consumer.

B. FUTURE WORK

Today’s demand for reliable electric power, not only for the DoD, but for communities and industries all over the world, supports the relevance of this thesis.

One future study could be the application of multiple EMS operating in parallel. In such a system, the performance of the P-Q power flow controller can be evaluated in a more complex environment.

Another worthwhile study could consider the implementation of peak power shaving when loads with large transients (such as motors) are present in the microgrid.

APPENDIX. MATLAB FILES

A. SIMULATION—FILES OF PARAMETERS

```
% LT KANAVAROS DIMITRIOS
% FILE OF PARAMETERS

%% TIME – FREQUENCIES
  tstep = 7e-7;
  tstop = 2;
  f_corner = 100*2;

%% EMS
  Kp_v=.0005;
  Ki_v=.05;
  sw_freq=15000;
  vo_ref=120*sqrt(2)*2/pi;
  turns= 1;
   PWM_mode=0;   %set to one for bipolar PWM or   zero for        unipolar PWM

 %% CIRCUIT
   Lin=400e-6;
   Cap=12e-6;

%% FILTER
  Cfilter = 22.5e-6;
  Lfilter = 1/(((2*pi*200)^2)*Cfilter);

%% HARMONICS
 % FREQUENCIES
  fund= 2*pi*60;      % Fundamental Frequency
  f_3 = fund*3;       % 3rd Harmonic
  f_5 = fund*5;       % 5th Harmonic
  f_7 = fund*7;       % 7th Harmonic
  f_9 = fund*9;       % 9th Harmonic
  f_11 = fund*11;     % 11th Harmonic
  f_13 = fund*13;     % 13th Harmonic

 % AMPLITUDES FOR P=150W (SAME WITH THOSE OF THE LAB)
  V_3 = 0.6016;
  V_5 = 3.324;
  V_7 = 1.539;
  V_9 = 0.3774;
  V_11 = 1.905;
```

```
  V_13 = 1.058;

 % AMPLITUDES FOR P=500W (SAME WITH THOSE OF THE LAB)
  V_3 = 0.6707;
  V_5 = 3.243;
  V_7 = 1.417;
  V_9 = 0.3367;
  V_11 = 1.851;
  V_13 = 1.182;

%% HIGH FREQUENCY NOISE
  f_noise = 100*fund;
  Ampl_noise = 120*sqrt(2)/10;

%% AC LOAD
  L1 = 1/(((3/3.2)+(3/1.6)+(2/.8))*1.5);
  R1 = 0.5;
  L2 = .002;
  R2=1/((6/1200)+(3/600)+(1/300));
  jw=j*2*pi*60;
  Z_total=1/(1/(jw*L1)+1/(jw*L2+R2));

%% BOOST
  Vbus_ref = 215;

%% GAIN OF OGM METHODS
  % QUARTER CYCLE DELAY METHOD
    Kp_delay=.01;
    Ki_delay=.1*2;

  % DIFFERENTIATION METHOD
    Kp_diff=.01;
    Ki_diff=.1*2;

  % SOGI METHOD
    Kp_sogi=.01;
    Ki_sogi=.1*2;

  % APF METHOD
    Kp_apf=.01;
    Ki_apf=.1*2;
```

B. SIMULATION—FILES OF PLOTS

```
% LT KANAVAROS DIMITRIOS
```

```
% FILE OF PLOTS

%% --------------- QUARTER CYCLE DELAY METHOD-------------
load PQ1.mat;
figure(1)
subplot(2,1,1), plot(time,PQ_AB1(:,1),'b','LineWidth',1.25);
ylabel("P[W]");
grid;
subplot(2,1,2), plot(time,PQ_AB1(:,2),'b','LineWidth',1.25);
ylabel("Q[VARS]");
xlabel('time[s]');
grid;
print(gcf,'-djpeg','-r350','figure1');

vac=data_out(:,1);
iac=data_out(:,4);    % source current
i_ems=data_out(:,3);  % ems current

figure (2)
plot(time,vac/50,'b')
hold on;
plot(time,iac/2,'g')
plot(time,i_ems,'r')
legend('vac/50','iac/2','iems','location','best');
hold off;
xlabel('time[s]')
ylabel('vac/50[V],iac/2[A] and iems[A]')
grid


%% ----------------- DIFFERENTIATION METHOD-------------
load PQ2.mat;
figure(1)
subplot(2,1,1), plot(time,PQ_AB2(:,1),'r','LineWidth',1.25);
ylabel("P[W]");
grid;
subplot(2,1,2), plot(time,PQ_AB2(:,2),'r','LineWidth',1.25);
ylabel("Q[VARS]");
xlabel('time[s]');
grid;
print(gcf,'-djpeg','-r350','figure1');

vac=data_out(:,1);
iac=data_out(:,4);    % source current
i_ems=data_out(:,3);  % ems current
```

```
figure (2)
plot(time,vac/50,'b')
hold on;
plot(time,iac/2,'g')
plot(time,i_ems,'r')
legend('vac/50','iac/2','iems','location','best');
hold off;
xlabel('time[s]')
ylabel('vac/50[V],iac/2[A] and iems[A]')
grid


%% ----------------- SOGI METHOD-------------
load PQ3.mat;
figure(1)
subplot(2,1,1), plot(time,PQ_AB3(:,1),'g','LineWidth',1.25);
ylabel("P[W]");
grid;
subplot(2,1,2), plot(time,PQ_AB3(:,2),'g','LineWidth',1.25);
ylabel("Q[VARS]");
xlabel('time[s]');
ylim([-400 100])
grid;
print(gcf,'-djpeg','-r350','figure1');

vac=data_out(:,1);
iac=data_out(:,4);    % source current
i_ems=data_out(:,3);  % ems current

figure (2)
plot(time,vac/50,'b')
hold on;
plot(time,iac/2,'g')
plot(time,i_ems,'r')
legend('vac/50','iac/2','iems','location','best');
hold off;
xlabel('time[s]')
ylabel('vac/50[V],iac/2[A] and iems[A]')
grid


%% ----------------- APF METHOD-------------
load PQ4.mat;
figure(1)
```

```
subplot(2,1,1), plot(time,PQ_AB4(:,1),'m','LineWidth',1.25);
ylabel("P[W]");
grid;
subplot(2,1,2), plot(time,PQ_AB4(:,2),'m','LineWidth',1.25);
ylabel("Q[VARS]");
ylim([-100 200])
xlabel('time[s]');
grid;
print(gcf,'-djpeg','-r350','figure1');

vac=data_out(:,1);
iac=data_out(:,4);    % source current
i_ems=data_out(:,3);  % ems current

figure (2)
plot(time,vac/50,'b')
hold on;
plot(time,iac/2,'g')
plot(time,i_ems,'r')
legend('vac/50','iac/2','iems','location','best');
hold off;
xlabel('time[s]')
ylabel('vac/50[V],iac/2[A] and iems[A]')
grid

%%------------ ALL THE METHODS TOGETHER-------------

%%
load PQ1.mat;
load PQ2.mat;
load PQ3.mat;
load PQ4.mat;
figure(1)
subplot(2,1,1), plot(time,PQ_AB1(:,1),'b');
hold on;
subplot(2,1,1), plot(time,PQ_AB2(:,1),'r');
subplot(2,1,1), plot(time,PQ_AB3(:,1),'g');
subplot(2,1,1), plot(time,PQ_AB4(:,1),'m');
hold off;
legend('DELAY','DIFF','SOGI','APF');
ylabel("P[W]");
grid;
subplot(2,1,2), plot(time,PQ_AB1(:,2),'b');
hold on;
subplot(2,1,2), plot(time,PQ_AB2(:,2),'r');
```

```
subplot(2,1,2), plot(time,PQ_AB3(:,2),'g');
subplot(2,1,2), plot(time,PQ_AB4(:,2),'m');
hold off
legend('DELAY','DIFF','SOGI','APF');
ylabel("Q[VARS]");
xlabel('time[s]');
grid;
print(gcf,'-djpeg','-r350','figure1');

vac=data_out(:,1);
iac=data_out(:,4);    % source current
i_ems=data_out(:,3);  % ems current

figure (2)
plot(time,vac/50,'b')
hold on;
plot(time,iac/2,'g')
plot(time,i_ems,'r')
legend('vac/50','iac/2','iems','location','best');
hold off;
xlabel('time[s]')
ylabel('vac/50[V],iac/2[A] and iems[A]')
grid


% --- ALL THE METHODS(EXCEPT DIFFERENTIATION METHOD)-

%%
load PQ1.mat;
load PQ3.mat;
load PQ4.mat;
figure(1)
subplot(2,1,1), plot(time,PQ_AB1(:,1),'b');
hold on;
subplot(2,1,1), plot(time,PQ_AB3(:,1),'g');
subplot(2,1,1), plot(time,PQ_AB4(:,1),'m');
hold off;
legend('DELAY','SOGI','APF');
ylabel("P[W]");
grid;
subplot(2,1,2), plot(time,PQ_AB1(:,2),'b');
hold on;
subplot(2,1,2), plot(time,PQ_AB3(:,2),'g');
subplot(2,1,2), plot(time,PQ_AB4(:,2),'m');
hold off
```

```
legend('DELAY','SOGI','APF');
ylabel("Q[VARS]");
xlabel('time[s]');
grid;
print(gcf,'-djpeg','-r350','figure1');

vac=data_out(:,1);
iac=data_out(:,4);    % source current
i_ems=data_out(:,3);  % ems current

figure (2)
plot(time,vac/50,'b')
hold on;
plot(time,iac/2,'g')
plot(time,i_ems,'r')
legend('vac/50','iac/2','iems','location','best');
hold off;
xlabel('time[s]')
ylabel('vac/50[V],iac/2[A] and iems[A]')
grid
```

C. SIMULATION—FILES OF PLOTS

```
% LT KANAVAROS DIMITRIOS
% FILE OF PLOTS

%%%%%%%%%%%%%%%%%%%----------OGMs-------
%%%%%%%%%%%%%%%%%%
%% ----------------- QUARTER CYCLE DELAY METHOD------------
clear all;
close all;
mode=0;  % 1 for rms and 0 for AB
OGM = 1;
sim test_10_Apr
PQ_AB1 = data_PQ;
save('PQ1.mat','PQ_AB1');

% ----------------- DIFFERENTIATION METHOD-------------
clear all;
close all;
mode=0;  % 1 for rms and 0 for AB
OGM = 2;
sim test_10_Apr
```

```
PQ_AB2 = data_PQ;
save('PQ2.mat','PQ_AB2');

% ----------------- SOGI METHOD-------------
clear all;
close all;
mode=0;  % 1 for rms and 0 for AB
OGM = 3;
sim test_10_Apr
PQ_AB3 = data_PQ;
save('PQ3.mat','PQ_AB3');

% ----------------- APF METHOD---------------------
clear all;
close all;
mode=0;  % 1 for rms and 0 for AB
OGM = 4;
sim test_10_Apr
PQ_AB4 = data_PQ;
save('PQ4.mat','PQ_AB4');

ec4150_microgrid_plot_Q_control
```

LIST OF REFERENCES

[1] Office of the Assistant Secretary of Defense for Energy, Installations and Environment, “Department of Defense Annual Energy Management and Resilience (AEMR) report, fiscal year 2016,” Jul. 2017. [Online]. Available: https://www.acq.osd.mil/eie/Downloads/IE/FY%202016%20AEMR.pdf

[2] Enviromental and Energy Study Institute (EESI), *DoD’s energy efficiency and renewable energy initiatives*, Jul. 27, 2011. [Online]. Available: https://www.eesi.org/files/dod_eere_factsheet_072711.pdf]

[3] S. Barker, S. Kalra, D. Irwin, and P. Shenoy, “Empirical characterization and modeling of electrical loads in smart homes,” *Intl. Green Comput. Conf. Proceedings. IEEE*, pp. 1–10, Jun. 2013.

[4] H. Akagi, E. H. Watanabe, and M. Aredes, *Instantaneous Power Theory and Applications to Power Conditioning*. Hoboken, NJ, USA: John Wiley and Sons, 2007.

[5] G. Oriti, A. L. Julian, and N. J. Peck, “Power-electronics-based energy management system with storage,” *IEEE Trans. Power Electron.*, vol. 31, no. 1, pp. 452–460, Jan. 2016.

[6] N. Anglani, G. Oriti, and M. Colombini, “Optimized energy management system to reduce fuel consumption in remote military microgrids,” *IEEE Trans. Industry Appl.*, vol. 53, no. 6, pp. 5777–5785, Nov.–Dec. 2017.

[7] G. Oriti and A. L. Julian, “Reactive power control with an energy management system in single phase AC microgrids,” in *IEEE Energy Convers. Congr. Expo (ECCE)*, 2015, pp.753–759.

[8] N. Mohan, T. M. Undeland, and W. P. Robbins, *Power Electronics*. Hoboken, NJ, USA: John Wiley and Sons, 2003.

[9] Festo Didactic, Ltd., “Home energy production,” in *Electricity and New Energy*, course sample 86361-F0, Lab-Volt, Quebec, Canada, 2012, pp. 1–4. [Online]. Available: http://www1.labvolt.com/publications/courseware_samples/86361_f0.pdf

[10] J. W. Nilsson and S. A. Riedel, *Electric Circuits*, 10th ed. Boston, MA, USA: Prentice Hall, 2015.

[11] “Injection of Harmonics,” class notes for Power Electronics, Dept. of Elect. Comput. Eng., Naval Postgraduate School, Monterey, CA, USA, autumn 2018.

[12] Institute of Electrical and Electronics Engineers Content Provider, *IEEE 100 : The Authoritative Dictionary of IEEE Standards Terms*, 7th ed. Piscataway, NJ, USA: Standards Information Network IEEE Press, 2000.

[13] D. Dong, T. Thacker, R Burgos, F. Wang, and D. Boroyevich, "On zero steady-state error voltage control of single-phase PWM inverters with different load types," *IEEE Trans. on Power Electron*. vol. 26, no. 11, pp. 3285–3297, Nov. 2011.

[14] T. Orlowska-Kowalska, F. Blaabjerg, and J. Rodriguez, *Advanced and Intelligent Control in Power Electronics and Drives.* Switzerland: Springer International Publishing, 2014.

[15] K. De Brabandere, T. Loix, K. Engelen, B. Bolsens, J. Van den Keybus, J. Driesen and R. Belmans, "Design and operation of a phase-locked loop with Kalman estimator-based filter for single-phase applications," *32nd Annu. Conf. IEEE Indust. Electr.*, 2006, pp. 525–530.

[16] RF Wireless World, "What is All Pass Filter (APF)." Accessed February 28, 2019. [Online] Available: http://www.rfwireless-world.com/Terminology/All-Pass-Filter-basics-and-types.html

[17] A. Roshan, R. Burgos, A. C. Baisden, F. Wang, and D. Boroyevich, "A D-Q frame controller for a full-bridge single phase inverter used in small distributed power generation systems," in *IEEE Appl. Power Electron. Conf.*, 2007, pp. 641–647.

[18] U. A. Miranda, M. Aredes, and L. G. B. Rolim, "A DQ synchronous reference frame current control for single-phase converters," *36th Power Electr. Specialists Conf.*, 2005, pp. 1377–1381.

[19] M. Bobrowska-Rafal, K. Rafal, M. Jasinski, and M. Kazmierkowski, "Grid synchronization and symmetrical components extraction with PLL algorithm for grid connected power electronic converters—A review," *Bull. Polish Acad. Sci.: Tech. Sci.*, 2011, pp. 485–497.

[20] S. Goldman, *Phase-Locked Loop Engineering Handbook for Integrated Circuits*. Boston, MA, USA: Artech House, 2007.

[21] R. I. Bojoi, L. R. Limongi, D. Roiu, and A. Tenconi, "Enhanced power quality control strategy for single-phase inverters in distributed generation systems," *IEEE Trans. Power Electron.*, vol. 26, no. 3, pp. 798–806, Mar. 2011.

[22] J. Rocabert, A. Luna, F. Blaabjerg, and P. Rodrıguez, "Control of power converters in AC microgrids," *IEEE Trans. Power Electron.*, vol. 27, no. 11, pp. 4734–4749, Nov. 2012.

[23] Xilinx, “Virtex-4 Family Overview,” Aug. 30, 2010. [Online]. Available: https://www.xilinx.com/support/documentation/data_sheets/ds112.pdf

[24] Xilinx, “System Generator for DSP—Getting Started Guide,” Dec. 02, 2009. [Online]. Available: https://www.xilinx.com/support/documentation/sw_manuals/xilinx11/sysgen_gs.pdf

THIS PAGE INTENTIONALLY LEFT BLANK

INITIAL DISTRIBUTION LIST

1. Defense Technical Information Center
   Ft. Belvoir, Virginia

2. Dudley Knox Library
   Naval Postgraduate School
   Monterey, California